Fall 11-12-2020

Numerical Simulations of Nonlinear Waves and Their Stability: Stokes Waves and Nonlinear Schroedinger Equation

Anastassiya Semenova
Doctoral Student, Applied Mathematics

Anastassiya Semenova

Candidate

Mathematics and Statistics

Department

This dissertation is approved, and it is acceptable in quality and form for publication:

Approved by the Dissertation Committee:

Alexander O Korotkevich , Chairperson

Pavel M Lushnikov

Deborah Sulsky

Peter Vorobieff

Evangelos Coutsias

Numerical Simulations of Nonlinear Waves and Their Stability: Stokes Waves and Nonlinear Schrödinger Equation

by

Anastassiya Semenova

B.S., Mathematics, University of New Mexico, 2013
M.S., Mathematics, University of New Mexico, 2016

DISSERTATION

Submitted in Partial Fulfillment of the
Requirements for the Degree of

Doctor of Philosophy
Mathematics

The University of New Mexico

Albuquerque, New Mexico

December, 2020

Dedication

To my family, my mom and husband. Thank you for all of your support.

Acknowledgments

I would like to thank my scientific advisor Professor Alexander O Korotkevich and co-advisor Pavel M Lushnikov for their guidance and patience through my studies, and knowledge that they shared with me.

In addition, I would like to express my gratitude to the faculty of the Department of Mathematics and Statistics at the University of New Mexico. I am deeply thankful to Professors Deborah Sulsky, Steven Lau, Jens Lorenz, and Daniel Appelö for their instructions and helpful discussions.

I would like acknowledge and show gratitude to members of our scientific group Sergey Dyachenko, Denis Sylantiev and Natalia Vladimirova for their helpful conversations.

Numerical Simulations of Nonlinear Waves and Their Stability: Stokes Waves and Nonlinear Schrödinger Equation

by

Anastassiya Semenova

B.S., Mathematics, University of New Mexico, 2013
M.S., Mathematics, University of New Mexico, 2016

PhD, Mathematics, University of New Mexico, 2020

Abstract

The present work offers an investigation of dynamics and stability of nonlinear waves in Hamiltonian systems. The first part of the manuscript discusses the classical problem of water waves on the surface of an ideal fluid in 2D. We demonstrate how to construct the Stokes waves, and how to apply a continuation method to find waves in close vicinity to the limiting Stokes wave. We provide new insight into the stability of the Stokes waves by identifying previously inaccessible branches of instability in the equations of motion for the fluid. We provide numerical evidence that pairs of unstable eigenvalues of linearized dynamical equations appear as a result of collision of pairs of neutrally stable eigenvalues at extrema of the Hamiltonian. Moreover, we find that eigenvalues of the linearized problem that become unstable follow a self–

similar law as they approach the instability threshold, and a power law is suggested for unstable eigenvalues in the immediate vicinity of the limiting wave.

A related problem of formation of Stokes waves from a generic plane wave is considered. It is determined that over long time a plane wave tends to a solution that is effectively described by a Stokes wave with a perturbation moving in the opposite direction to the Stokes wave. This perturbation to the Stokes wave may be described by an effective Hamiltonian, that has quadratic and cubic terms with respect to the perturbations.

A train of Stokes waves can be studied assuming a slowly–varying envelope, with dynamics of the envelope subject to the nonlinear Schrödinger equation (NLSE). In the second part of the present work we provide comparison of two numerical methods to solve NLSE. The first one is the standard second order split-step method based on an operator splitting approach. The second method is the Hamiltonian–conserving method referred to as the Hamiltonian integration method (HIM). HIM allows exact conservation of the Hamiltonian and wave action but requires implicit time stepping. We find that the NLSE can benefit from the Hamiltonian–conserving method compared to the split step method in particular for such solutions as the Akmediev and the Kuznetsov–Ma solitons as well as multisoliton solutions. We find that numerical error for HIM is systematically smaller than for the split-step scheme for the same timestep. At the same time, one can take orders of magnitude larger timesteps in HIM, compared to split step, while still ensuring numerical stability. We propose the Hamiltonian–conserving method for the Majda–Maclaughlin–Tabak (MMT) model, which is a generalization of NLSE.

Contents

List of Figures

List of Tables

Chapter 1

Introduction

1.1 Free Surface Water Waves in Ideal Fluid

The motion and nature of water waves is a subject that is both interesting and puzzling. This topic is considered a classical problem and has been investigated and developed for at least a century and a half. For example, as Sir George G. Stokes described in the introduction to the 1847 paper [2], a ship's trajectory is directly affected by the velocity of water waves. If ocean waves can be treated as oscillatory waves and their velocity measured, then the trajectory of the ship can be approximated. Sir George G. Stokes in the work [2] (also published in [3]) studied waves that propagate with constant velocity without change of form in an ideal (incompressible and inviscid) 2-dimensional fluid with potential flow. These waves are often referred to as Stokes waves or progressive waves. The height H of the Stokes wave is defined to be the distance between the trough and the crest of the wave, and the ratio between the height and wave length L is called steepness $s = H/L$. In the original work [2], Stokes developed a method that expands free-surface water waves in power series of the amplitude of the progressive wave referred to as Stokes'

expansion. It was shown by Nekrasov [4] that expansion in small amplitudes is indeed convergent. This approach works well in the case of waves with small amplitudes, and it was shown that Stokes waves are periodic surface waves. In 1925, Levi-Cevita proved existence of such waves in the paper [5]. However as amplitudes of Stokes waves increase, the series might not converge or converges slowly. It was proposed by Stokes in [2], [6] that progressive waves have a maximum or limiting height, and he argued that the angle at the summit of the limiting wave should be $\frac{2\pi}{3}$. This result has been rigorously proved in the works of Plotnikov [7] and Amick *et al* [8] independently of each other. The Stokes expansion does not work for the limiting wave due to there being a stagnation point at the crest of the wave. So, it was suggested by Stokes in [6] to switch to conformal variables instead to study progressive waves with large heights. In 1968 Zakharov in the work [9], found that surface elevation and velocity potential at the surface are canonical Hamiltonian variables. Series expansion of Hamiltonian in canonical variables has been used later to construct reduced models for free surface waves.

In 1893 Mitchel in [10] numerically computed waves with large height and got that the limiting steepness should be 0.142. Stokes waves have been computed by many authors: Grant [11], Schwartz [12], Williams [13], [14], Maklakov [15], Gandzha and Lukomsky [16], Dyachenko *et al* [17], [18], Lushnikov *et al* [19], and many more.

Equations in physical variables require the normal derivative of the velocity potential at the free surface to be known. The normal derivative can be computed by applying the Dirichlet to Neumann operator to surface potential. However, the Dirichlet to Neumann operator is represented by an infinite series in powers of steepness, and may converge slowly or does not converge for waves with large steepness. New implicit equations of motion in conformal variables were constructed separately by Ovsyannikov [20] and Dyachenko *et al* [21]. These equations are computed in the lower complex half plane, and the Dirichlet to Neumann operator is transformed

into the Hilbert operator. In these equations, a time-dependent conformal transformation maps the half-strip in w plane ($(u, v) \in [-\pi, \pi] \times (-\infty, 0]$) into the area $(x, y) \in [-\pi, \pi] \times (-\infty, \eta]$ in the physical plane occupied by the fluid, as can be seen in the figure 1.2 where x is the horizontal component, y is the vertical component, and t is time. The function $y = \eta(x, t)$ represents the free surface of the fluid, and the line $v = 0$ is mapped into the fluid surface. These equations in conformal variables are further simplified in the work of Dyachenko [22]. We use these equations to study evolution of periodic progressive waves and their stability.

The stability of periodic gravity progressive waves in deep water with small amplitudes were studied in the works of Benjamin [23], Benjamin and Feir [24], Lighthill [25] and Whitham [26]. Benjamin and Feir found that waves with weak nonlinearity (small amplitude waves) are unstable to long-wave perturbations. This modulational instability is often referred to as Benjamin-Feir or subharmonic instability. In the work [27], Longuet-Higgins looked at superharmonic instability of the Stokes wave. Here we refer to superharmonic perturbation as a perturbation having a smaller wave length than the original Stokes wave. The stability of progressive waves was considered as a function of wave steepness. Longuet-Higgins was able to compute waves only up to the steepness $H/L = 0.13$. He showed that the waves remain stable with respect to superharmonic perturbations, but he proposed that the instability occurs at the steepness $H/L \approx 0.1387$. Tanaka in the work [28], computed that instability develops at the steepness $H/L = 0.1366$, and one unstable mode appears. He stated that the first maximum of the total energy is attained at the steepness at which the first superharmonic instability occurs. The kinetic, potential and total energy of Stokes waves were studied in the works of Longuet-Higgins [29], Longuet-Higgins and Fox [30] and Longuet-Higgins and Dommermuth [31]. In the work [1], Tanaka and Longuet-Higgins found that as steepness of the Stokes wave increases past $H/L = 0.1366$ a second unstable mode appears. It is natural to assume that as we approach the limiting Stokes waves, more unstable modes would appear. The

stability of Stokes waves were further studied in the works of Longuet-Higgins and Cokelet [32], Bridges [33], and many others.

1.2 Hamiltonian Integration Method

If we consider the envelope approximation description for a moving train of Stokes waves in the ocean, we will get the nonlinear Schrödinger equation often referred to as NLSE (Zakharov *et al* [34]).

It is one of the most common nonlinear partial differential equations in mathematical and theoretical physics (Sulem and Sulem [35]). Although, it can be considered as a natural generalization of a classical Schrödinger equation in quantum mechanics (Landau [36]), NLSE has a more general range of applications. NLSE naturally appears if one considers envelope dynamics of a quasi–monochromatic nonlinear wave that was studied by Zakharov *et al* in [37]. In quantum mechanics a version of NLSE is called a Gross–Pitaevskii equation [38] which describes a Bose-Einstein condensate for short-range interactions of particles.

A classical example of NLSE application is the dynamics of optical pulses in an optical fiber. The time evolution of the envelope of an optical pulse in a fiber is well approximated by NLSE, including the description of very long, transoceanic optical communication lines, see e.g. Agrawal [39], Lushnikov [40]. Langmuir waves in plasmas are described by NLSE as well, for example in the works of Zakharov [41], and Silantiev *et al* [42]. In the paper [43] Dysthe, uses NLSE and its modifications to describe dynamics of quasi-monochromatic ocean waves. The analysis of NLSE offers a possible explanation to the mystery of the appearance of rogue waves [44]. These and many other applications require numerical simulation of NLSE or its modifications, and the natural question that arises is what is an efficient method to do that.

There are many techniques that can be applied in the simulation of NLSE: the Crank-Nicholson scheme (Crank-Nicholson [45], Taha and Ablowitz [46]), the hop-scotch method (Greig and Morris [47]), the Ablowitz–Ladik scheme (Ablowitz and Ladik [48], [49]), the pseudo–spectral split-step method (Tappert [50], Taha and Ablowitz [46]), the Hamiltonian preserving method (Dyachenko *et al* [51]), and many others. The de facto standard method of integration of NLSE was proposed by Tappert [50]. Taha and Ablowitz studied its performance in the article [46]. The split-step method is based on the Strang's operator splitting approach [52] combined with a pseudo-spectral method. The stability of the split-step method has been recently studied in the work of Lakoba [53] and references therein. The split-step method can be constructed to any order of accuracy, in this work we consider the second order symmetrized split-step (SS2) method.

In 1992, Dyachenko *et al* in the article [51] proposed a new method for simulation of NLSE. It was used to study wave or optical turbulence in two–dimensional NLSE, however it passed largely unnoticed by a wide audience. Recent papers such as Chen *et al* [54] and Gong *et al* [55] describe somewhat similar numerical methods. We refer to the numerical method from [51] as the Hamiltonian integration method (HIM) and study it in our paper Semenova *et al* [56]. It is based on discrete Hamilton's equations, and this method conserves the numerical Hamiltonian and the optical power (also called the number of particles or wave action) exactly (up to any desired accuracy in exact arithmetic). In finite precision arithmetic, the error in conservation of Hamiltonian is due to round-off errors inherent to specific finite precision floating point representation.

The Hamiltonian–preserving numerical schemes can be derived for other systems by using the discrete Hamilton's equations. As an example, in the recent work of Korotkevich *et al* [57] on numerical simulations of nonlinear water waves, a Hamiltonian–preserving scheme was described. There are similarities between HIM

and the symplectic methods like those presented in Yoshida [58]. HIM is a completely self–contained method which can be derived for other Hamiltonian systems having canonical symplectic structure. For example, we have done it for the Majda, McLaughlin, and Tabak (MMT) model [59] which is a widely used generalization of NLSE.

We compare the HIM and SS2 numerical methods by performing a set of simulations with various initial conditions. In these experiments we observe that in some scenarios the HIM method outperforms SS2 when very high accuracy is not essential. The SS2 method requires a stringent condition on the time step for stability, whereas HIM is an implicit method and as such allows the time step to be a hundred times larger. Our observations illustrate that the HIM method might be the method of choice for efficient simulations of interaction of solitons, where a tight balance between nonlinearity and dispersion occurs.

Part I

Free Surface Hydrodynamics, Stokes Waves

Chapter 1

Equations of Motion

1.1 Problem Formulation

We consider an ideal 2-dimensional fluid located under a free-surface represented by a 1-dimensional curve $y = \eta(x,t)$. The fluid is acted upon by the force of gravity and the effects of surface tension and atmospheric pressure are neglected. The velocity field of the fluid in Eulerian coordinates is denoted by $\mathbf{v}(x,y,t)$ that varies in space and time, where (x,y) and t are the spatial and temporal variables respectively. The fluid is inviscid and incompressible, and its flow is potential with the velocity potential $\Phi(x,y,t)$ and $\mathbf{v} = \nabla\Phi$. Incompressibility implies that Φ satisfies the Laplace equation:

$$\nabla \cdot \mathbf{v} = \nabla \cdot \nabla\Phi = \Delta\Phi = 0. \tag{1.1}$$

The kinematic and dynamic boundary conditions at the free surface are:

$$\frac{\partial \eta}{\partial t} = -\frac{\partial \Phi}{\partial x}\frac{\partial \eta}{\partial x} + \left.\frac{\partial \Phi}{\partial y}\right|_{y=\eta(x,t)} \tag{1.2}$$

$$\left(\frac{\partial \Phi}{\partial t} + \frac{1}{2}\left(\nabla\Phi\right)^2\right)\Bigg|_{y=\eta(x,t)} + g\eta = 0, \tag{1.3}$$

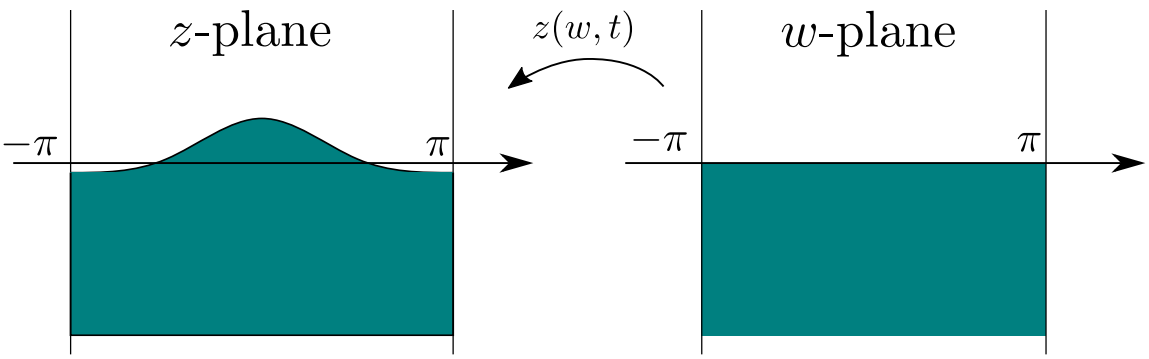

Figure 1.1: Half-strip in w plane ($(u, v) \in [-\pi, \pi] \times (-\infty, 0]$) into the area in (x, y) plane under the free-surface $\eta(x, t)$. The line $v = 0$ is mapped into the fluid surface.

where g is the acceleration of gravity. The fluid depth can be chosen arbitrarily, and we consider infinite fluid depth. At the bottom, the fluid is motionless, and $\Phi(x, y, t)|_{y=-h} = 0$ as $h \to \infty$. We consider a free surface $y = \eta(x, t)$ that is periodic in the x variable, and the same for the velocity potential Φ.

The equations (1.2)–(1.3) are the boundary conditions for Laplace equation (1.1) that must be solved in order to determine the normal component of velocity at the surface. Because the fluid domain is varying in time, the Laplace equation must be solved in a spatial domain that varies in time. Fortunately we can map this domain into one that is fixed in time by employing a time–varying conformal map.

1.2 Conformal Map

We consider a time-dependent conformal map $z(w, t) = x(w, t) + iy(w, t)$ with $w = u + iv$. It maps the half-strip $[-\pi, \pi] \times (-\infty, 0]$ of the complex plane w into the area in the (x, y) plane occupied by a single period of the fluid domain. The line $v = 0$ is mapped into the fluid surface and its shape has a parametric representation given

by:

$$x(u,t) = u + \tilde{x}(u,t),\ y = y(u,t), \tag{1.4}$$

where $\tilde{x}$ is a deviation from the identity transformation and $\tilde{x}(u,t)$ and $y(u,t)$ are 2π–periodic functions of u. All variables are transformed to be dimensionless.

1.3 Equations of Motion in Conformal Domain

The implicit equations of motion in conformal variables on the real line $w = u, v = 0$ were derived from the equations (1.2)–(1.3) by Ovsyanikov [20] and later independently by Dyachenko *et al* [21]. It is convenient to introduce the potential on the free surface $\psi(x,t) = \Phi|_{y=\eta(x,t)}$ and the implicit equations have the form:

$$y_t x_u - x_t y_u = -\hat{H}\psi_u \tag{1.5}$$

$$y_u \psi_t - y_t \psi_u + g y y_u = -\hat{H}(x_u \psi_t - x_t \psi_u + g y x_u) \tag{1.6}$$

where $\hat{H}$ denotes a circular Hilbert transform given by the formula:

$$\hat{H}f(u) = \frac{1}{2\pi}\text{p.v.}\int_{-\pi}^{\pi} f(u')\cot\left(\frac{u'-u}{2}\right)du', \tag{1.7}$$

where $p.v.$ denotes the Cauchy principal value integral. We assume that $f(u)$ is a 2π periodic function (like $y(u)$ and $\tilde{x}(u)$), and it has Fourier series representation $f(u) = \sum f_k e^{iku}$. In Fourier space, the operator (1.7) corresponds to multiplication of Fourier coefficients of the function $f(u)$ by $i\,\text{sign}\,k$, and has the following form,

$$(\hat{H}f)_k = i\,\text{sign}(k) f_k. \tag{1.8}$$

Equations (1.5)–(1.6) can be rewritten in explicit form as was done in Dyachenko

et al [21], [60] (also published in Zakharov *et al* [61]):

$$y_t = (y_u \hat{H} - x_u)\frac{\hat{H}\psi_u}{|z_u|^2}, \tag{1.9}$$

$$\psi_t + gy = \frac{\hat{H}\left(\psi_u \hat{H}\psi_u\right)}{|z_u|^2} + \psi_u \hat{H}\left(\frac{\hat{H}\psi_u}{|z_u|^2}\right). \tag{1.10}$$

Since $z(u,t)$ is analytic in $\mathbb{C}^-$, its real and imaginary parts are related by the Hilbert transform:

$$y = \hat{H}\tilde{x}, \qquad \tilde{x} = -\hat{H}y, \tag{1.11}$$

where $\tilde{x}(u,t) = x(u,t) - u$ and $\tilde{z}(u,t) = z(u,t) - u$.

In the paper [22], Dyachenko introduced new variables:

$$R = \frac{1}{z_u} \quad \text{and} \quad V = \frac{i\Pi_u}{z_u} \tag{1.12}$$

with V being the complex velocity and $\Pi = \psi + i\hat{H}\psi$ being the complex potential. The equations (1.9)–(1.10) can be reformulated into:

$$R_t = i\left(UR_u - U_u R\right), \tag{1.13}$$

$$V_t = i\left(UV_u - RB_u\right) + g(R-1), \tag{1.14}$$

Here U and B are the expressions:

$$U = \hat{P}(V\bar{Q}^2 + \bar{V}Q^2), \quad B = \hat{P}\frac{\partial}{\partial u}(V\bar{V}) \tag{1.15}$$

where bar means complex conjugation and $\hat{P} = \frac{1+i\hat{H}}{2}$ is a projector generating a function analytic in the lower complex half-plane. In Fourier space, the operator $\hat{P}$ is a Fourier multiplier given by the formula:

$$\hat{P}_k = \frac{1 - \operatorname{sign} k}{2} = \begin{cases} 1, k < 0 \\ \frac{1}{2}, k = 0 \\ 0, k > 0 \end{cases} \tag{1.16}$$

which amounts to zeroing out the positive Fourier coefficients and multiplication of the zero Fourier coefficient by half. These equations can be extended to include surface tension by introducing $Q = \sqrt{R}$:

$$Q_t = i\left(UQ_u - \frac{1}{2}QU_u\right), \tag{1.17}$$

$$V_t = i\left(UV_u - BQ^2\right) + g(Q^2 - 1) - 2\sigma R\hat{P}\frac{\partial}{\partial u}\left(Q_u\bar{Q} - \bar{Q}_u Q\right), \tag{1.18}$$

where σ is the surface tension coefficient. In our simulations we assume that $\sigma = 0$ (surface tension is negligible).

1.4 Numerical Method

An explicit 6th order Runge-Kutta method is used to evolve the equations (1.17)–(1.18) in time. The projection operator $\hat{P}$ and spatial derivatives are computed in Fourier space, and it is convenient to use a uniform grid in u to have access to the fast Fourier transform. We use a plane wave as an initial condition for equations (1.17)–(1.18) and evolve it for long time (10 or more periods). Results of these computations are described in the chapter "Spontaneous Formation of Stokes Waves from Plane Waves".

1.5 Conserved Quantities

Free–surface hydrodynamics is a Hamiltonian system, with the Hamiltonian in physical variables given by,

$$\mathcal{H} = \frac{1}{2}\int_{-\pi}^{\pi}\int_{-h}^{\eta(x,t)} (\nabla\Phi)^2\, dydx + \frac{g}{2}\int_{-\pi}^{\pi}\eta^2 dx \tag{1.19}$$

We use eqations (1.9) – (1.10) in free-surface variables, and we need to transform the Hamiltonian to be defined on the surface. Note that variable x depends on u and

$dx = x_u du$, so the potential energy has the form:

$$U = \frac{g}{2}\int \eta^2 dx = \frac{g}{2}\int y^2 x_u du \tag{1.20}$$

To modify the kinetic energy over the domain $D = (x, y) \in [-\pi, \pi] \times (-h, \eta(x)]$, we use Green's identity:

$$\begin{aligned}
K &= \frac{1}{2}\int\int_D (\nabla\Phi)^2 \, dydx \\
&= \frac{1}{2}\int_{\partial D} \Phi\left(\nabla\Phi \cdot d\Gamma\right) - \frac{1}{2}\int\int_D \Phi\nabla^2\Phi dxdy \\
&= \frac{1}{2}\int_{-\pi}^{\pi} \left(\Phi\Phi_y\right)|_{y=-h} dx + \frac{1}{2}\int_{-h}^{\eta(\pi)} \left(\Phi\Phi_x\right)|_{x=\pi} dy \\
&+ \frac{1}{2}\int \psi\left(\nabla\Phi \cdot \mathbf{n}\right)|_{y=\eta(x)} dl - \frac{1}{2}\int_{-h}^{\eta(-\pi)} \left(\Phi\Phi_x\right)|_{x=-\pi} dy \\
&= \frac{1}{2}\int_{-\pi}^{\pi} \psi\left(\Phi_x y_u - \Phi_y x_u\right)|_{v=0} du.
\end{aligned}$$

We write Φ_x and Φ_y in terms of Φ_u and Φ_v to get the kinetic energy in terms of surface variables (as derived by Dyachenko *et al* in [60] and later described in details by Dyachenko *et al* in [18]),

$$K = -\frac{1}{2}\int_{-\pi}^{\pi} \psi\hat{H}\psi_u du. \tag{1.21}$$

The Hamiltonian in free-surface variables is given by,

$$\mathcal{H} = K + U = -\frac{1}{2}\int \psi\hat{H}_u\psi \, du + \frac{g}{2}\int y^2 x_u \, du, \tag{1.22}$$

where $\psi = \Phi|_{y=\eta(x,t)}$, $z = x + iy$.

The momentum of the solution is a conserved quantity and is given by the following expression:

$$\mathcal{P} = \int_{-\pi}^{\pi}\int_{-\infty}^{\eta(x,t)} \Phi_x dx = -\int_{-\pi}^{\pi} \psi y_u \, du. \tag{1.23}$$

The Hamiltonian $\mathcal{H}$ and the momentum $\mathcal{P}$ are important parts of discussion in chapters "Spontaneous Formation of Stokes Waves from Plane Waves" and "Stability of Stokes Waves".

Chapter 2

Stokes Waves

Stokes waves are nonlinear periodic traveling progressive waves on the surface of an ideal fluid. The height of a Stokes wave H is the distance between crest and trough, and the steepness is the ratio of height H over a wavelength L. Stokes waves can be parametrized by their steepness H/L.

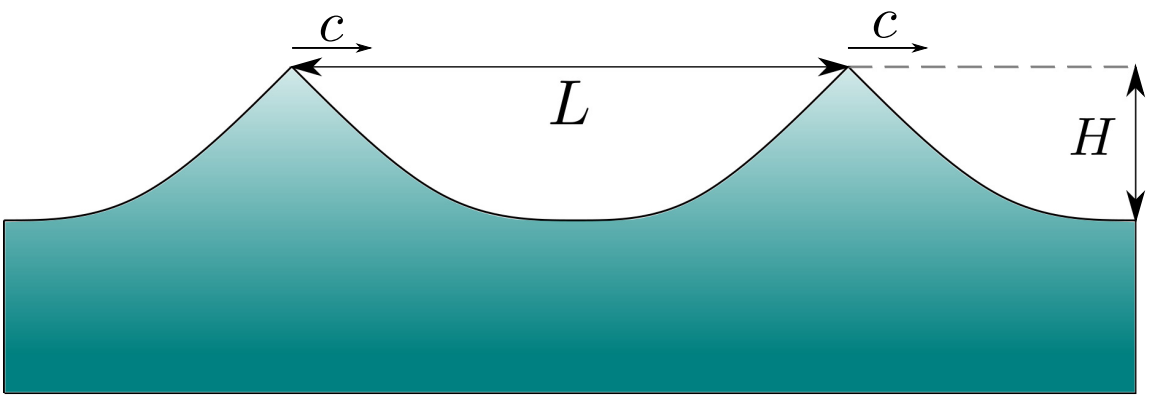

Figure 2.1: A Stokes wave is a nonlinear periodic traveling wave on the surface of an ideal fluid. The height H is the distance between crest and trough, and L is the wavelength.

To find a Stokes wave, we need to assume that the solution of (1.5) – (1.6)

propagates with constant speed c. We consider ψ and z as functions of one variable $u - ct$,

$$z(u,t) = u + \tilde{z}(u - ct), \tag{2.1}$$

$$\psi(u,t) = \psi(u - ct) \tag{2.2}$$

with ψ and $\tilde{z}$ being periodic functions. We note that $c = \tilde{c}/c_0$ where $\tilde{c}$ is in physical units and $c_0 = \sqrt{g/k}$ with $k = 2\pi/L$ to make speed dimensionless.

This change of variables corresponds to transformation to the moving frame of reference $u - ct \to u$. Functions $\psi(u)$ and $\tilde{z}(u)$ are periodic with period 2π. In this fame of reference, we place the crest of a Stokes wave at $u = 0$, so the wave is symmetric in u relative to the origin. This implies that $y(u)$ is an even function, and due to (1.11) $\tilde{x}(u)$ should be an odd function. We also need $\tilde{x}(u)$ to be a periodic function, and thus $\tilde{x}(\pm\pi) = 0$. So we get that $\eta(x(\pm\pi), t) = \eta(\pm\pi, t)$, and Stokes waves have the same spatial period in conformal (u as in (2.1)) and physical (x as in $\eta(x - ct)$) variables.

From equation (1.5), we obtain expressions $cy = \hat{H}\psi$ and $\psi = -c\hat{H}y$. We eliminate ψ from equation (1.6) and derive an integro–differential equation for Stokes waves,

$$-c^2 y_u + g y y_u + g\hat{H}[y(1 + \tilde{x}_u)] = 0. \tag{2.3}$$

We define the operator $\hat{k} = -\frac{\partial}{\partial u}\hat{H}$ and apply $\hat{H}$ to the equation (2.3) to get the equation (obtained by Babenko [62] and later independently rederived in Dyachenko *et al* [17]) for $y(u)$,

$$\left(c^2\hat{k} - 1\right) y - \left(\frac{\hat{k}y^2}{2} + y\hat{k}y\right) = 0. \tag{2.4}$$

We note that the total mass of fluid should be conserved. This means that mean elevation of the free surface should be zero, and the expression $\int_{-\pi}^{\pi} y(x)dx = \int_{-\pi}^{\pi} y(u)x_u du = 0$ needs to be satisfied.

2.1 Computing Stokes Waves via Newton Conjugate Gradient Method

We use the Newton conjugate gradient (Newton-CG) method (Yang [63], [64]) to solve the equation (2.4). This method was implemented by Dyachenko *et al* in [17] to compute Stokes waves, and consists of two stages: linearization of (2.4) and solution of the resulting linear system via the conjugate gradient (CG) method.

We define the operator $\hat{L}$ of the equation (2.4) to be,

$$\hat{L}y \equiv \left(c^2\hat{k} - 1\right) y - \left(\frac{\hat{k}y^2}{2} + y\hat{k}y\right) = 0. \tag{2.5}$$

We linearize it around the nth approximation y^n,

$$\hat{L}y^n + \hat{L}_1\delta y = 0 \tag{2.6}$$

with $\hat{L}_1 = -\hat{M}\delta y - \left(\hat{k}\left[y^n\delta y\right] + y^n\hat{k}\delta y + \delta y\hat{k}y^n\right)$ and $\hat{M} = 1 - \frac{c^2}{g}\hat{k}$.

We solve the linear system (2.6) for δy via the CG method (e.g. Schewchuk *et al* [65]) and then get the $n+1$st approximation,

$$y^{n+1} = y^n + \delta y. \tag{2.7}$$

Note that the monotonic convergence is guaranteed only for positive definite matrices in the CG method. Even though the operator $\hat{L}_1$ is indefinite, the Newton-CG method converges from our experience at least for some range of initial conditions.

Chapter 3

Spontaneous Formation of Stokes Waves from Plane Waves

In this chapter, we find how trains of Stokes waves may form in deep water. In order to do that we consider evolution of a plane wave for long time (10 or more periods) to get numerical solutions resembling a Stokes wave. These solutions travel at almost constant speed and their shape resembles Stokes waves superposed with a perturbation moving in the opposite direction to the Stokes wave.

3.1 Initial Condition

We would like to understand how a generic plane wave will converge to a nearly coherent train of periodic traveling Stokes waves. For that, we use the conformal variables approach (1.17)–(1.18), and consider an initial condition in the form of a

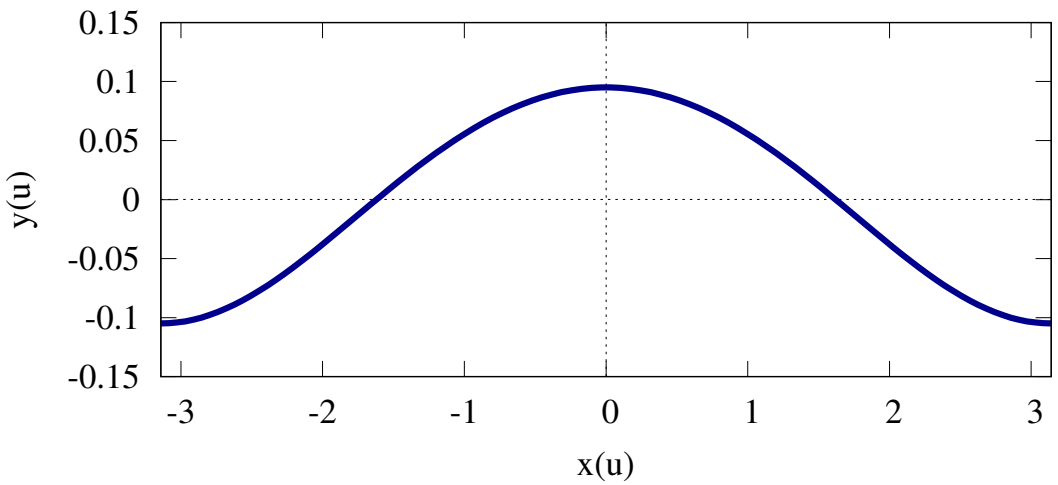

Figure 3.1: Initial condition (3.1)–(3.2) with $A = 0.1$ and $c_{init} = 1$. On the vertical axis we plot $y(u)$, and on the horizontal axis we plot $x(u)$.

plane wave,

$$z(u) = u + iAe^{-iu} + iy_0 \quad \text{and} \quad z_u = 1 + Ae^{-iu} \tag{3.1}$$

$$\Pi_u = c_{init}(z_u - 1) \tag{3.2}$$

where A is the amplitude, c_{init} is the initial speed and $y_0 = -i\frac{A^2}{2}$ is chosen so that $\int_{-\pi}^{\pi} y dx = 0$ or the free surface's mean elevation is zero. The velocity c_{init} is a parameter chosen between 1 and 2. The speed of a Stokes wave is larger than 1, and we want initial conditions to have velocities similar to those of Stokes waves. An example of such an initial condition is presented in the Figure 3.1 with $A = 0.1$ and $c_{init} = 1$.

We evolve plane waves (3.1)–(3.2) and produce solutions that have shapes similar to Stokes waves as can be seen in the Figure 3.2. It appears that there is some perturbation on the top of the numerical solution that moves in the opposite direction to the wave. So, we seek a Stokes wave that best matches the numerical solution.

We define the speed of the numerical solution and look for the Stokes wave with

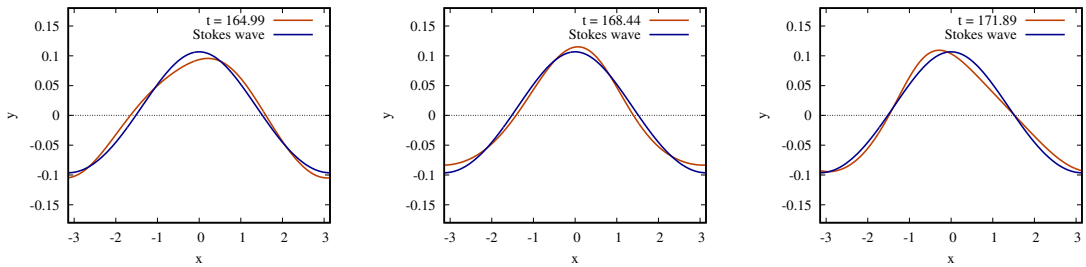

Figure 3.2: We show the free surface of the numerical solution (yellow line) and Stokes wave (blue line). Three panels correspond to different time slots: (left panel) $t = 164.99$, (center) $t = 168.44$, and (right) $t = 171.89$.

the same speed. To define the speed, we track the location of the maximum elevation, x_{max}, of the numerical solution as a function of time. We do a least squares fit of $x_{max}(t)$ to a linear function whose slope gives the speed of the numerical solution. We choose a window in time so that the least–square relative error is of the order 10^{-7} or better. For initial speeds $1 \leq c_{init} \leq 2$, we are getting the speeds of numerical solutions that are between 1.00516 and 1.0092, consistent with the range of velocities typically found in Stokes waves.

We study if the numerical solution indeed approaches a Stokes wave with some noise and decompose the numerical solution in a sum of a Stokes wave z^S, Π^S, and the remainder which we denote by δz and $\delta\Pi$:

$$z(u,t) = z^S + \delta z, \tag{3.3}$$

$$\Pi(u,t) = \Pi^S + \delta\Pi. \tag{3.4}$$

3.2 Stokes Wave and Perturbation

It is a nontrivial question how to split the solution into a Stokes wave, and into the remainder. Our initial attempt is to track the maximum peak of the free–surface in

time. Given the time series for the position of the crest of the numerical solution:

$$u_{max}(t) = \arg\max_{u} y(u,t), \tag{3.5}$$

$$x_{max}(t) = x(u_{max}(t),t), \tag{3.6}$$

we find the average speed c_s by the formula:

$$c_s = \frac{1}{T}\int_0^T x_{max}(t)\,dt. \tag{3.7}$$

where T is the averaging time which is typically of the order of 600 ($\sim$ 100 periods of Stokes wave). Given the value c_s, we find an associated Stokes wave with the same speed of propagation, and mark this wave as the "background" solution, z^S and Π^S. We would like to note that the choice of the background may not necessarily be optimal, and we also try to determine the propagation speed from minimizing the time–average of the mixed term (described in the next section "Energy Balance") of the Hamiltonian.

3.3 Energy Balance

We split Hamiltonian and momentum into a pure Stokes part, a mixed term and the remainder. The main idea of this splitting is to see if the remainder is almost decoupled from the background Stokes wave.

3.3.1 The Hamiltonian

The Hamiltonian (1.22) is split into the sum of three terms:

$$H = H^S + H_{mt} + H_{rm}. \tag{3.8}$$

Here,

$$\mathcal{H}^S = K^S + U^S = -\frac{1}{2}\int \psi^S \hat{H}_u \psi^S \, du \tag{3.9}$$

$$+ \frac{g}{2}\int \left(y^S\right)^2 \left(1 - \hat{H}_u y^S\right) \, du, \tag{3.10}$$

gives the energy of just the Stokes part of the solution. The $\mathcal{H}_{mt}$ is the mixed energy that measures the cross interaction of the Stokes wave with the solution remainder:

$$\mathcal{H}_{mt} = -2\int \left(\hat{H}_u \psi^S\right) \delta\psi \, du \tag{3.11}$$

$$+ g\int \left(y^S - y^S \hat{H}_u y^S - \hat{H}_u \left(y^S\right)^2\right) \delta y - 2y^S \delta y H_u \delta y \, du. \tag{3.12}$$

The $\mathcal{H}_{rm}$ is the remainder term that governs the motion of the remainder in the potential of the Stokes wave and is split into quadratic and cubic parts:

$$\mathcal{H}_{rm} = \mathcal{H}_{rm2} + \mathcal{H}_{rm3}. \tag{3.13}$$

The quadratic term gives the dispersion relation of the linear waves on the background of the Stokes solution, and the cubic term captures the nonlinearity in the remainder:

$$\mathcal{H}_{rm2} = -\frac{1}{2}\int \delta\psi \hat{H}_u \delta\psi + \frac{g}{2}\int (\delta y)^2 \left(1 - \hat{H}_u y^S\right) du \tag{3.14}$$

$$\mathcal{H}_{rm3} = -\frac{g}{2}\int \hat{H}_u (\delta y)^2 \, \delta y \, du. \tag{3.15}$$

3.3.2 The Momentum

Similarly to the Hamiltonian, we can split the momentum (1.23) as follows:

$$P = P^S + P_{mt} + P_{rm}, \tag{3.16}$$

where:

$$P^S = \int \psi^S y_u^S \, du = \frac{1}{c} K^S \tag{3.17}$$

$$P_{mt} = \int \left(\delta\psi y_u^S + \psi^S \delta y_u \right) \, du = \frac{1}{c} \int \left(\left(\hat{H}_u \psi^S \right) \delta\psi + c^2 \left(\hat{H}_u y^S \right) \delta y \right) \, du \tag{3.18}$$

$$P_{rm} = \int \delta\psi \delta y_u \, du \tag{3.19}$$

We now return to the question of splitting the solution into the Stokes wave and the remainder. The idea is to choose the Stokes wave in such a way that the time–averages of the mixed terms $\mathcal{H}_{mt}$ and $\mathcal{P}_{mt}$ are the smallest.

3.3.3 Simulations

In this section, we demonstrate results that show the balance of the terms in the Hamiltonian and momentum of the full numerical solution.

We evolve initial conditions (3.1)–(3.2) with $A = 0.1$ and $c_{init} = 1$ until time $t = 600$. After computing the speed of the solution and finding a Stokes wave with the same velocity, we split our solution in the form (3.3)–(3.4). In Figure 3.3, we show the mixed term (blue line) and remainder term (green line) of the Hamiltonian (left panel) and momentum (right panel) with their corresponding average values. We see that the mixed terms in the Hamiltonian and momentum behave similarly, and their time averages are not close to zero. They are of the same order as time averages for the remainder terms of the Hamiltonian and momentum. We assume time averages of $\mathcal{H}_{mt}$, $\mathcal{P}_{mt}$ are not close to zero due to the way we find the background Stokes wave.

Let us consider the mixed terms in the Hamiltonian and momentum more closely. We split the H_{mt} and P_{mt} into terms that depend on δy and $\delta\Psi$. In the Figure 3.4, we plot δy (magenta line) and $\delta\Psi$ (yellow line) terms of the Hamiltonian and momentum

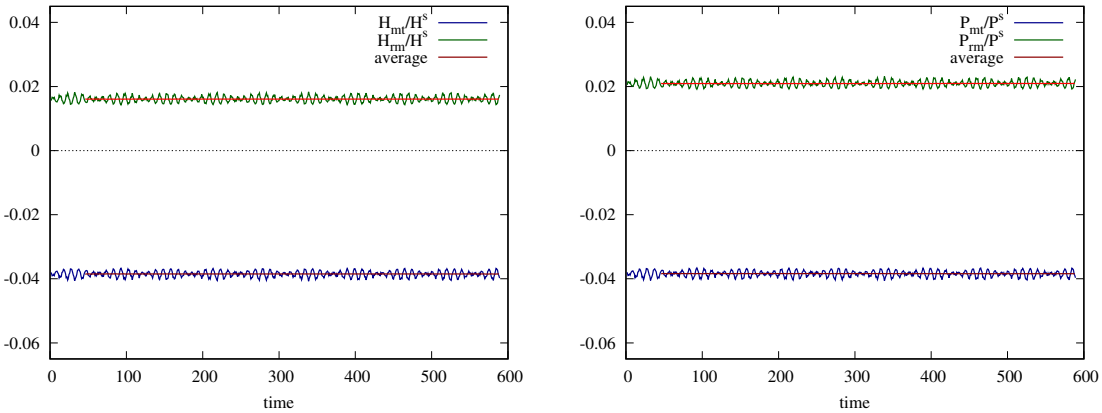

Figure 3.3: The mixed term and the remainder term for the Hamiltonian and momentum for the initial speed $c_{ini} = 1$ and the time averages.

for the mixed terms and zoom into time interval $450 \leq t \leq 470$. The average values of the δy and $\delta\Psi$ terms are close to each other (dark red line), and both contribute to the average values of mixed terms. By changing the background Stokes wave, we may make these averages become zero.

Other choices of initial data yield qualitively similar results.

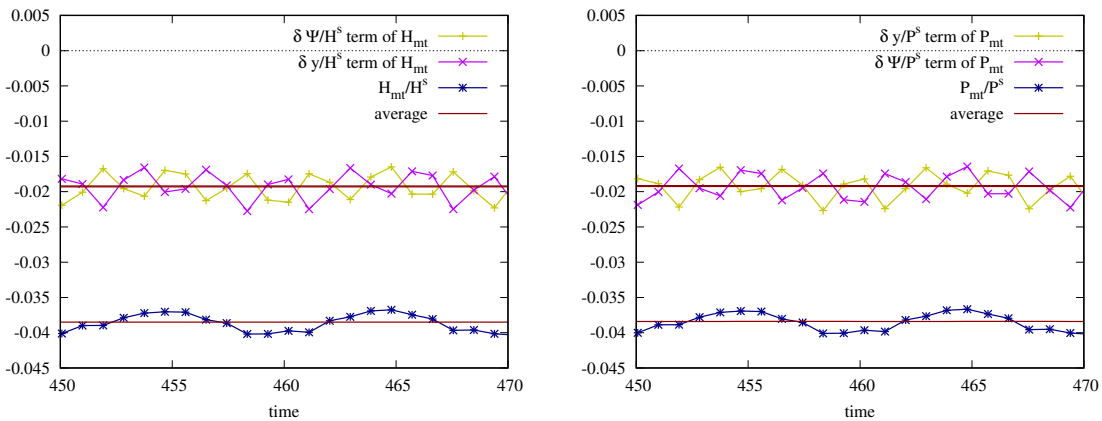

Figure 3.4: The mixed term of the Hamiltonian and momentum for the initial constant $c_{ini} = 1$ and their time averages.

3.4 Change of Coordinate System

Despite there being no criterion for wave breaking, it is observed that large amplitude solutions tend to develop overhanging shapea and break in numerical simulations. Therefore, we consider a small amplitude plane wave to prevent the solution from wave breaking. We consider a simulation with amplitude $A = 0.099875$ and velocity $c_{init} = 1.005$. In this simulation, we start with the initial speed that matches the speed of a small amplitude Stokes wave. The solution is evolved until much longer times ($t = 5000$) and its velocity is $c_s = 1.00516$ which is matched to a corresponding Stokes wave. We notice that the Stokes wave with c_s has non zero values for the averages of mixed terms for Hamiltonian and momentum similar to results of previous section. The potential energy of the Stokes wave does not explicitly depend on its velocity, and the mixed term of the potential energy of the numerical solution is matched to a potential energy of some Stokes wave. This way we find the Stokes wave that corresponds to the average value of the mixed term of potential energy being zero. Moreover, the average of mixed terms of kinetic energy and momentum also end up being close to zero. The best match was the Stokes wave with $H/L = 0.0316130972106355$ and velocity $c_s = 1.004944$. This velocity however does not match the one we found via the least squares method, and the waves move away from each other as time grows. This results in the average values of the integrals varying on a long time scale. In order to make the numerical solution and the chosen Stokes wave travel at the same speed, we go to a moving frame of reference. To do so, we apply Fourier transform to $z_S(u, t)$ to evolve the Stokes in time with velocity $c_s = 1.00516$. Our conjecture is that the reference frame of the system moves with the velocity corresponding to the difference between the Stokes velocity 1.004944 and computed solution velocity $c_s = 1.00516$.

For the above initial condition and Stokes wave, the average value of both mixed terms in the Hamiltonian and the momentum are close to zero. We also find that

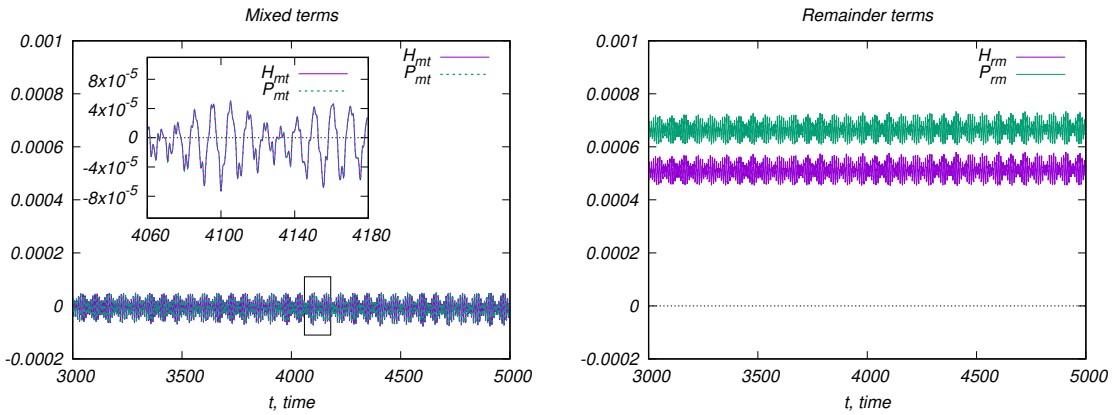

Figure 3.5: (left) The mixed terms of the Hamiltonian and momentum. (right) The remainder terms of the Hamiltonian and momentum.

the remainder terms are larger than the mixed terms as shown in the Figures 3.5 and 3.6. In the Figure 3.7, we plot $\mathcal{H}_{mt}$ and $\mathcal{P}_{mt}$ (red and green lines respectively) and remainder terms $\mathcal{H}_{rm}$, $\mathcal{P}_{rm}$ (blue and yellow lines respectively) as functions of initial speeds. As the speed increases the absolute values of remainder terms increase and the values of mixed terms stay close to zero.

This work is far from being complete and the final goal would be to write equations for the remainder to understand if the remainder gets absorbed into the background of a Stokes wave solution at long time.

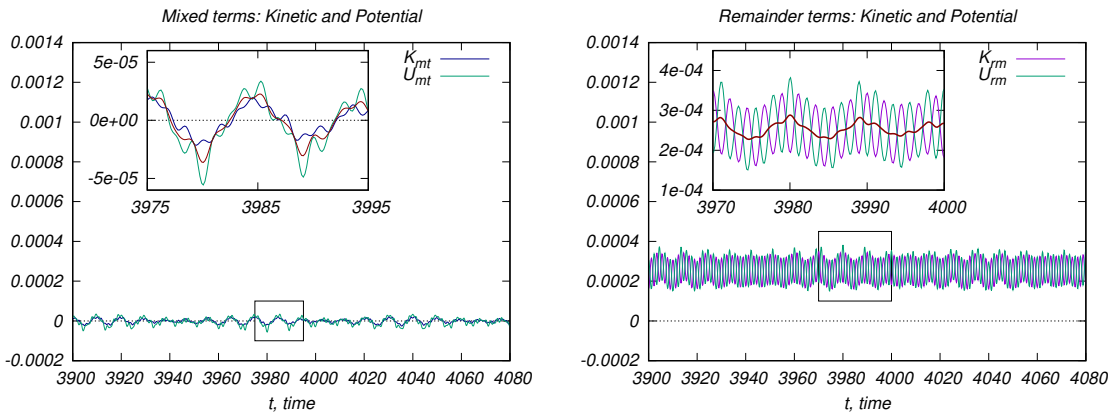

Figure 3.6: (left) Mixed terms of kinetic and potential energy and the average of total energy. (right) Remainder terms of kinetic and potential energy and the average of total energy.

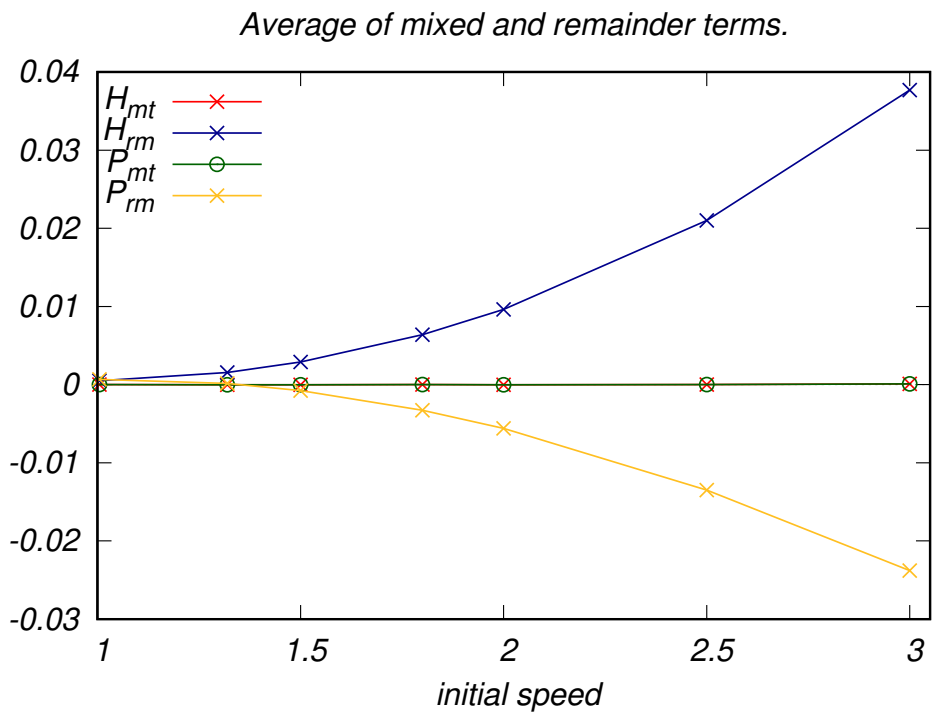

Figure 3.7: Average of the Hamiltonian and momentum mixed terms (red and green lines respectively) and remainder terms (blue and yellow lines respectively) as functions of initial speed. As speed increases the absolute value of the remainder terms increases and the value of mixed terms stay close to zero.

Chapter 4

Stability of Stokes Waves

In this chapter, we study superharmonic instabilities of Stokes waves. We use the ratio of crest-to-trough height, H, to wavelength, L as a definition of wave steepness. The method of frozen coefficients to study eigenvalues of the linearized equations does not provide conclusive results. It was stated by Longuet-Higgins [27] that Stokes waves remain stable with respect to superharmonic perturbations up to the steepness $H/L = 0.1387$ when the Stokes wave speed $c(H/L)$ passes through the first extremum. In 1983 Tanaka [28] showed that the first instability appears at a steepness $H/L = 0.1366$ when the Hamiltonian $\mathcal{H}$ has its first extremum. We solve the eigenvalue problem numerically and for the first time we get to the third unstable eigenmode and predict apperance of new modes at steepness corresponding to extrema of the Hamiltonian confirming previous observations of Longuet-Higgins and Tanaka [1] in the process.

4.1 Method of Frozen Coefficients

4.1.1 Linearization Around a Stokes Wave Solution and Method of Frozen Coefficients for ψ and y

We look at a linearization of the general time-dependent equations around a Stokes wave solution:

$$y_t = (y_u\hat{H} - x_u)\left[\frac{1}{|z_u|^2}\hat{H}\psi_u\right] \tag{4.1}$$

and

$$\psi_t = \psi_u\hat{H}\left[\frac{1}{|z_u|^2}\hat{H}\psi_u\right] + \frac{1}{|z_u|^2}\hat{H}\left[\psi_u\hat{H}\psi_u\right] - gy, \tag{4.2}$$

where g is free-fall acceleration.

We write $y = y + \delta y$ and $\psi = \psi + \delta\psi$ where y and ψ on the right side are the pure Stokes wave solution, and δy and $\delta\psi$ are small perturbations. The linearization of the equations (4.1)–(4.2) leads to the following system for δy and $\delta\psi$:

$$\begin{aligned}
\delta y_t =&(\delta y_u\hat{H} + \hat{H}[\delta y_u])\left[\frac{1}{|z_u|^2}\hat{H}\psi_u\right] + (y_u\hat{H} - x_u)\left[\frac{1}{|z_u|^2}\hat{H}\delta\psi_u\right] - \\
&- (y_u\hat{H} - x_u)\left[\frac{(\hat{H}\psi_u)}{|z_u|^4}\Big(-2x_u\hat{H}\partial_u\delta y + 2y_u\partial_u\delta y\Big)\right] \qquad (4.3)\\
\delta\psi_t =&\delta\psi_u\hat{H}\left[\frac{1}{|z_u|^2}\hat{H}\psi_u\right] + \psi_u\hat{H}\left[\frac{1}{|z_u|^2}\hat{H}\delta\psi_u\right] - \\
&- \psi_u\hat{H}\left[\frac{(\hat{H}\psi_u)}{|z_u|^4}\Big(-2x_u\hat{H}\partial_u\delta y + 2y_u\partial_u\delta y\Big)\right] - \\
&- \frac{-2x_u\hat{H}\partial_u\delta y + 2y_u\partial_u\delta y}{|z_u|^4}\hat{H}\left[\psi_u\hat{H}\psi_u\right] + \\
&+ \frac{1}{|z_u|^2}\hat{H}\left[\delta\psi_u\hat{H}\psi_u\right] + \frac{1}{|z_u|^2}\hat{H}\left[\psi_u\hat{H}\delta\psi_u\right] - g\delta y. \qquad (4.4)
\end{aligned}$$

The equations (4.3) and (4.4) are written in vector form with a 2×2 operator matrix as follows:

$$\mathbf{Q}_t = \hat{M}\mathbf{Q}, \quad \mathbf{Q} \equiv \begin{pmatrix} \delta y \\ \delta\psi \end{pmatrix}, \tag{4.5}$$

where

$$\hat{M} = \begin{pmatrix} \hat{M}_{11} & \hat{M}_{12} \\ \hat{M}_{21} & \hat{M}_{22} \end{pmatrix} \tag{4.6}$$

and

$$\begin{aligned}
\hat{M}_{11}q =& \Big((\partial_u q)\hat{H} + [\hat{H}\partial_u q]\Big)\left[\frac{1}{|z_u|^2}\hat{H}\psi_u\right] - \\
&- (y_u\hat{H} - x_u)\left[\frac{(\hat{H}\psi_u)}{|z_u|^4}\Big(-2x_u\hat{H}\partial_u q + 2y_u\partial_u q\Big)\right], \\
\hat{M}_{12}q =& (y_u\hat{H} - x_u)\left[\frac{1}{|z_u|^2}\hat{H}\partial_u q\right], \\
\hat{M}_{21}q =& -\psi_u\hat{H}\left[\frac{(\hat{H}\psi_u)}{|z_u|^4}\Big(-2x_u\hat{H}\partial_u q + 2y_u\partial_u q\Big)\right] - \\
&- \frac{-2x_u\hat{H}\partial_u q + 2y_u\partial_u q}{|z_u|^4}\hat{H}\left[\psi_u\hat{H}\psi_u\right] - gq, \\
\hat{M}_{22}q =& (\partial_u q)\hat{H}\left[\frac{1}{|z_u|^2}\hat{H}\psi_u\right] + \psi_u\hat{H}\left[\frac{1}{|z_u|^2}\hat{H}(\partial_u q)\right] + \frac{1}{|z_u|^2}\hat{H}\left[(\partial_u q)\hat{H}\psi_u\right] + \\
&+ \frac{1}{|z_u|^2}\hat{H}\left[\psi_u\hat{H}(\partial_u q)\right].
\end{aligned} \tag{4.7}$$

Instead of working directly with the matrix operator (4.7), we linearize it over y and ψ keeping only the linear terms (but notice that $x_u = 1 - \hat{H}y_u$ which implies that $\frac{1}{|z_u|^2} = 1 + 2\hat{H}y_u + O(y_u^2)$) which means that we assume that we linearize about

a weakly nonlinear solution (like a Stokes wave far from the limiting wave). The linearization then gives

$$\begin{aligned}
\hat{M}_{11}q &= -(\partial_u q)\psi_u - (\hat{H}\psi_u)\hat{H}\partial_u q,\\
\hat{M}_{12}q &= -y_u\partial_u q - \hat{H}\partial_u q - (\hat{H}y_u)\hat{H}\partial_u q,\\
\hat{M}_{21}q &= -gq,\\
\hat{M}_{22}q &= -2(\partial_u q)\psi_u + \hat{H}\left[(\partial_u q)\hat{H}\psi_u + \psi_u\hat{H}(\partial_u q)\right].
\end{aligned} \tag{4.8}$$

It is immediately seen from Eq. (4.8) that $\hat{M}$ is not self-adjoint with respect to the scalar product

$$\langle \mathbf{f}, \mathbf{g}\rangle \equiv \int_{-\pi}^{\pi} \mathbf{g}^T\mathbf{f}\, du, \tag{4.9}$$

where $\mathbf{f}$ and $\mathbf{g}$ are two arbitrary vector functions.

We consider the full equations (4.7) and study their stability via the method of frozen coefficients. We treat terms in (4.7) independent of q as constants or frozen coefficients and approximate expressions of the form $\hat{H}[f(\psi_u, y_u)q_u]$ by $\hat{H}[f(\psi_u, y_u)q_u] = -e^{\mathrm{i}ku}|k|f(\psi_u, y_u)q_k$ where we assume that $q \propto e^{\lambda t}e^{\mathrm{i}ku}q_k$ and $f(\psi_u, y_u)$ are arbitrary functionals of ψ_u and y_u. Equations (4.7) are transformed into,

$$\begin{aligned}
e^{-\mathrm{i}ku}\hat{M}_{11}q &= q_k\left(\mathrm{i}k\hat{H} - |k|\right)\left[\frac{1}{|z_u|^2}\hat{H}\psi_u\right] + q_k\frac{(\hat{H}\psi_u)}{|z_u|^4}2|k||A|^2,\\
e^{-\mathrm{i}ku}\hat{M}_{12}q &= q_k\frac{|k|\bar{A}}{|z_u|^2},\\
e^{-\mathrm{i}ku}\hat{M}_{21}q &= q_k\frac{2|k|A}{|z_u|^4}\left\{-\psi_u\mathrm{i}\,\mathrm{sign}(k)(\hat{H}\psi_u) - \hat{H}\left[\psi_u\hat{H}\psi_u\right]\right\} - gq_k,\\
e^{-\mathrm{i}ku}\hat{M}_{22}q &= q_k\left(\mathrm{i}k\hat{H} - |k|\right)\left[\frac{1}{|z_u|^2}\hat{H}\psi_u\right] - 2\mathrm{i}kq_k\psi_u\frac{1}{|z_u|^2},
\end{aligned} \tag{4.10}$$

where

$$|k|A \equiv (x_u|k| + \mathrm{i}ky_u) = |k|(x_u + \mathrm{i}\,\mathrm{sign}(k)y_u) \quad \text{and} \quad |A|^2 = |z_u|^2 \tag{4.11}$$

As a result, we can express the linearized problem (4.5) in the following form,

$$\lambda \begin{pmatrix} \delta y_k \\ \delta \psi_k \end{pmatrix} = \begin{pmatrix} \hat{M}_{11} & \hat{M}_{12} \\ \hat{M}_{21} & \hat{M}_{22} \end{pmatrix} \begin{pmatrix} \delta y_k \\ \delta \psi_k \end{pmatrix}. \tag{4.12}$$

We consider two cases, when $g = 0$ and $g \neq 0$. In the case when $g = 0$, by evaluating the determinant of (4.12) we get the following expression,

$$\begin{aligned} \lambda &= \left(\mathrm{i}k\hat{H} - |k|\right)\left[\frac{1}{|z_u|^2}\hat{H}\psi_u\right] + \frac{|k||A|^2\hat{H}\psi_u}{|z_u|^4} - \frac{\mathrm{i}k\psi_u}{|z_u|^2} \\ &\pm \frac{\sqrt{-|k|^2\left(-|A|^4(\hat{H}\psi_u)^2 + 2|A|^2\hat{H}\left[\psi_u\hat{H}\psi_u\right]|z_u|^2 + \psi_u^2|z_u|^4\right)}}{|z_u|^4} \\ &= \mathrm{i}k\hat{H}\left[\frac{1}{|z_u|^2}\hat{H}\psi_u\right] - \frac{\mathrm{i}k\psi_u}{|z_u|^2}, \end{aligned} \tag{4.13}$$

i.e. λ is purely imaginary. To compute (4.13) we used equations (4.11) and the following identity,

$$-(\hat{H}\psi_u)^2 + 2\hat{H}\left[\psi_u\hat{H}\psi_u\right] + \psi_u^2 = 0 \tag{4.14}$$

which is obtained from the properties of the Hilbert transform.

In the case $g \neq 0$, the expression for λ has the form,

$$\lambda = \mathrm{i}k\hat{H}\left[\frac{1}{|z_u|^2}\hat{H}\psi_u\right] - \frac{\mathrm{i}k\psi_u}{|z_u|^2} \pm \sqrt{\frac{-\bar{A}g|k|}{|z_u|^2}}, \tag{4.15}$$

i.e. λ is not purely imaginary. We see that $Re(\lambda) \simeq \pm\frac{\mathrm{sign}(k)y_u}{2}\sqrt{g|k|}$ for waves with small steepness and the real part of λ is small.

If we want to compute growth rates of Stokes waves in the moving frame of reference ($y(u,t) = y(u-ct)$ and $\psi(u,t) = \psi(u-ct)$), we need to consider $q \propto e^{\lambda t}e^{\mathrm{i}k(u-ct)}q_k$. Then the expression of λ for any choice of g becomes,

$$\lambda = \mathrm{i}kc + \mathrm{i}k\hat{H}\left[\frac{1}{|z_u|^2}\hat{H}\psi_u\right] - \frac{\mathrm{i}k\psi_u}{|z_u|^2} \pm \sqrt{\frac{-\bar{A}g|k|}{|z_u|^2}}, \tag{4.16}$$

and the only difference is the addition of the term $\mathrm{i}ck$ to the imaginary part of λ.

4.1.2 Linearization and Method of Frozen Coefficients for R and V Variables

We consider the Dyachenko equations (1.13)–(1.14),

$$\begin{aligned}
\frac{\partial R}{\partial t} &= \mathrm{i}\left(UR_u - RU_u\right),\\
U &= \hat{P}^-(R\bar{V} + \bar{R}V), \quad B = \hat{P}^-(|V|^2),\\
\frac{\partial V}{\partial t} &= \mathrm{i}\left[UV_u - RB_u\right] + g(R-1),
\end{aligned}$$

Similarly to the ψ, y variables, we express R and V as a sum of a pure Stokes wave solution R, V and δR, δV as small perturbations, $R = R + \delta R$ and $V = V + \delta V$. We write the linearization of equations (1.13)–(1.14) and get the following system for δR and δV,

$$\frac{\partial \delta R}{\partial t} = \mathrm{i}\left(\delta U R_u + U\delta R_u - \delta R U_u - R\delta U_u\right), \tag{4.17}$$

$$\delta U = \hat{P}^-(\delta R\bar{V} + R\delta\bar{V} + \delta\bar{R}V + \bar{R}\delta V), \quad \delta B = \hat{P}^-(\delta V\bar{V} + V\delta\bar{V}), \tag{4.18}$$

$$\frac{\partial \delta V}{\partial t} = \mathrm{i}\left[\delta U V_u + U\delta V_u - \delta R B_u - R\delta B_u\right] + g\delta R. \tag{4.19}$$

We study the stability of solutions of equations in R and V variables by assuming that $\delta R, \delta V \propto e^{\lambda t}e^{\mathrm{i}ku}$ with $k < 0$ (requirement of analyticity in $\mathbb{C}^-$) and $|k| \gg 1$. Equations (4.17)–(4.19) are transformed into

$$\begin{aligned}
\lambda\delta R_k =& \mathrm{i}([\delta R_k\bar{V} + \bar{R}\delta V_k]R_u + \mathrm{i}kU\delta R_k - \delta R_k U_u - \mathrm{i}kR[\delta R_k\bar{V} + \bar{R}\delta V_k] -\\
& R[\delta R_k\bar{V}_u + \bar{R}_u\delta V_k]) \simeq \mathrm{i}\left(\mathrm{i}kU\delta R_k - \mathrm{i}kR[\delta R_k\bar{V} + \bar{R}\delta V_k]\right), \qquad (4.20)\\
\lambda\delta V_k =& \mathrm{i}\left[(\delta R_k\bar{V} + \bar{R}\delta V_k)V_u + \mathrm{i}kU\delta V_k - \delta R_k B_u - \mathrm{i}kR(\delta V_k\bar{V}) - R(\delta V_k\bar{V}_u)\right] +\\
& g\delta R_k \simeq \mathrm{i}\left[\mathrm{i}kU\delta V_k - \mathrm{i}kR(\delta V_k\bar{V})\right] + g\delta R, \qquad (4.21)
\end{aligned}$$

where

$$\delta U \simeq \delta R\bar{V} + \bar{R}\delta V, \quad \delta B = \delta V. \tag{4.22}$$

In matrix form the above equations can be written as,

$$\lambda \begin{pmatrix} \delta R_k \\ \delta V_k \end{pmatrix} = \begin{pmatrix} -k(U - R\bar{V}) & -k|R|^2) \\ g & -k(U - R\bar{V}) \end{pmatrix} \begin{pmatrix} \delta R_k \\ \delta V_k \end{pmatrix}, \tag{4.23}$$

and eigenvalues have the form,

$$\lambda = k(-U + R\bar{V}) \pm \sqrt{gk|R|^2}. \tag{4.24}$$

We recall that we linearized R and V about Stokes waves, and use properties of Stokes waves to simplify and study the expression (4.24). From the property $\Pi_u = c(z_u - 1)$, we get that

$$\begin{aligned} V &= \mathrm{i}\frac{\Pi_u}{z_u} = \mathrm{i}\frac{c(z_u - 1)}{z_u} = \mathrm{i}c(1 - R), \\ U &= \hat{P}(R\bar{V} + \bar{R}V) = \mathrm{i}c\hat{P}(-(R-1) + (\bar{R} - 1)) = -\mathrm{i}c(R-1) = V, \\ R\bar{V} - U &= -\hat{P}(R\bar{V} + \bar{R}V) + R\bar{V} = \mathrm{i}c(|R|^2 - 1), \\ B_u &= c^2\hat{P}(|1 - R|^2)_u. \end{aligned} \tag{4.25}$$

The expression for the Stokes wave growth rate follows from (4.24) and (4.25),

$$\lambda = \mathrm{i}ck(|R|^2 - 1) \pm \sqrt{gk|R|^2}. \tag{4.26}$$

We see that λ is purely imaginary for $k < 0$, and it has no instability for any g.

In the moving frame of reference ($R(u,t) = R(u - ct)$ and $V(u,t) = V(u - ct)$), we consider $\delta R, \delta V \propto e^{\lambda t}e^{\mathrm{i}k(u-ct)}\delta R_k, \delta V_k$ and the expression for λ changes to,

$$\lambda = \mathrm{i}kc + \mathrm{i}ck(|R|^2 - 1) \pm \sqrt{gk|R|^2}. \tag{4.27}$$

The only difference is the addition of the term $\mathrm{i}ck$ to the imaginary part of λ.

4.1.3 Next Order in k for Arbitrary Nonlinearity for ψ, y and R, V

We consider the next order in k for ψ, y and R, V, and use equations (4.5)–(4.7) and equations (4.17)–(4.19) respectively. We compute expressions of the form

$\hat{H}[f(\psi_u, y_u)q_u]$ for y and ψ equations as,

$$\hat{H}[f(\psi_u, y_u)q_u] = e^{\mathrm{i}ku}\mathrm{i}\,\mathrm{sign}(k)f(\psi_u, y_u)[\mathrm{i}kq_k + (q_k)_u] = \\ = -|k|e^{\mathrm{i}ku}f(\psi_u, y_u)\left[q_k - \frac{\mathrm{i}\,\mathrm{sign}(k)}{|k|}(q_k)_u\right], \tag{4.28}$$

where as before we assume that $f(\psi_u, y_u)$ are the arbitrary functional of ψ_u and y_u and $q = e^{\lambda t}e^{\mathrm{i}ku}q_k(u)$. We omit derivations here and provide the resulting expressions for λ,

$$\lambda \simeq \mathrm{i}ck + \mathrm{i}k\hat{H}\left[\frac{1}{|z_u|^2}\hat{H}\psi_u\right] - \frac{\mathrm{i}k\psi_u}{|z_u|^2} \\ \pm |k|^{1/2}\sqrt{(\hat{H}\psi_{uu} + \mathrm{i}\,\mathrm{sign}(k)\psi_{uu})2\psi_u - (x_u - \mathrm{i}\,\mathrm{sign}(k)y_u)g|z_u|^2}. \tag{4.29}$$

We see that λ is not purely imaginary for both cases $g \neq 0$ and $g = 0$ in the next order of approximation.

Similarly, we consider the next order in k for equations (4.20)–(4.21) in R and V variables. In those equations, we consider all terms including ones with $O(k^0)$. The corresponding eigenvalues have the following form,

$$\lambda = \mathrm{i}ck + \mathrm{i}ck(|R|^2 - 1) \pm \sqrt{2\mathrm{i}c^2kR\bar{R}_u(1 - |R|^2) + \left(\frac{g}{R} + \mathrm{i}c^2\bar{R}R_u\right)k|R|^2} + O(k^0). \tag{4.30}$$

We conclude that the expression under the square root in equation (4.30) has an imaginary component thus λ has a nonzero real part with both signs, i.e. this equation indicates instability.

In Figure 4.1, we show the real part of the eigenvalue (4.29) and (4.30) as a function of u for fixed $k = -5000$ computed using the method frozen coefficients. There are three panels in the Figure 4.1, the left panel corresponds to a small Stokes wave with velocity $c = 1.001$, the center panel amounts to a Stokes wave with $c = 1.026$, and the right panel shows a result for the steepest Stokes wave (among these three) with $c = 1.09289$. The blue color shows results for ψ, y variables and the green color corresponds to R, V variables, and the solid and dotted lines correspond

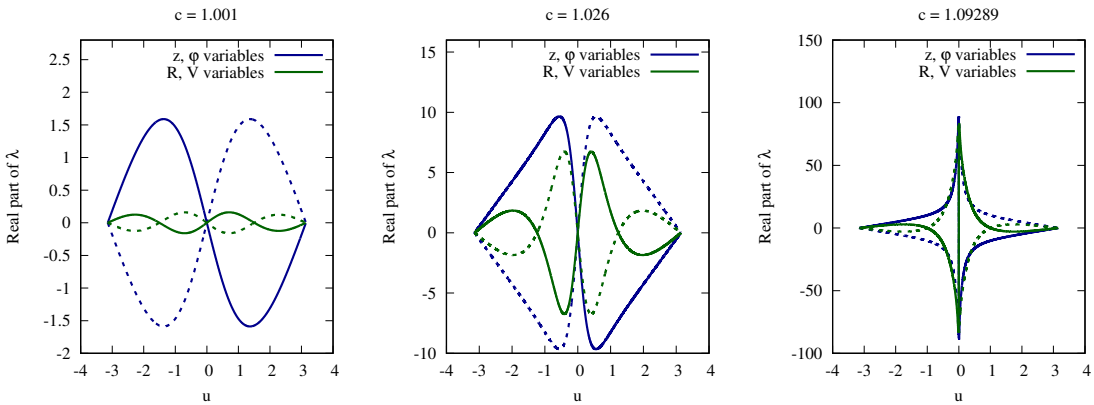

Figure 4.1: In all three panels, we present the real part of eigenvalues vs u with $k = -5000$. The eigenvalue in z, ψ variables corresponding to (4.29) are in blue and the eigenvalues in R, V variables corresponding to equation (4.30) are in green. The solid line corresponds to one branch and the dotted to the other. (Left) Stokes wave with $c = 1.001$; (Center) Stokes wave with $c = 1.026$; (Right) Stokes wave with $c = 1.09289$

to the two branches of the eigenvalue. We see that the real part of the eigenvalues grows with increase in steepness of Stokes waves.

From the theory of frozen coefficients, the next order correction in k gives little insight into stability of Stokes waves. Instead, an accurate portrayal of eigenvalues behaviour can be found by numerically solving the linearized operator.

Table 4.1: Mean values of real part of eigenvalues from the figure 4.1

Mean of real part of eigenvalues	$c = 1.001$	$c = 1.026$	$c = 1.09289$
z, ψ variables, (solid) branch	-1.6×10^{-16}	3.9×10^{-15}	8.2×10^{-15}
z, ψ variables, (dotted) branch	-2.9×10^{-16}	-1.4×10^{-15}	-3.1×10^{-15}
R, V variables, (solid) branch	-2.2×10^{-17}	-4.6×10^{-16}	-2.4×10^{-15}
R, V variables, (dotted) branch	2.2×10^{-17}	4.6×10^{-16}	2.4×10^{-15}

4.2 Numerical Solution of Eigenvalue Problem

In this section, we linearize the equations of motion and solve the associated eigenvalue problem numerically for superharmonic instability of Stokes waves.

4.2.1 Extrema of Hamiltonian of Stokes Waves

It is known that integral quantities associated with the Stokes solution oscillate as a function of wave steepness in the vicinity of the limiting Stokes wave. It is convenient to use the ratio of crest-to-trough height, H, to wavelength, L, as a definition of wave steepness

$$s = H/L. \tag{4.31}$$

Following the asymptotic theory of Longuet-Higgins and Fox [30] and Longuet-Higgins and Dommermuth [31], we may identify the extremal points of the Hamiltonian as Stokes waves approach the wave of greatest height.

The asymptotic theory ([30], [31]) provides formulae for Stokes wave speed, and total energy, $\mathcal{H}$, in the vicinity of limiting wave:

$$c^2(\epsilon) = \frac{g}{k}\left(1.1931 - 1.18\epsilon^3 \cos(2.143 \ln \epsilon + 2.22)\right), \tag{4.32}$$

$$\mathcal{H}(\epsilon) = \frac{g}{k}\left(0.07286 - 0.383\epsilon^3 \cos(2.143 \ln \epsilon + 1.59)\right), \tag{4.33}$$

where ϵ provides a different parameterization of the Stokes wave family. It is defined as follows:

$$\epsilon^2 = \frac{kq^2}{2g}, \tag{4.34}$$

where k is the wavelength, and q is the velocity of a fluid particle located at the crest of the wave measured in the reference frame moving with the speed c. We may

n	$\frac{H}{L}$ (Simulation)	$\mathcal{H}$ (Simulation)
1	1.366035366678e-01	4.651771802692e-01
2	1.407965842848e-01	4.577057808638e-01
3	1.410496267216e-01	4.577972786501e-01
4	1.410627373980e-01	4.577961527320e-01

Table 4.2: Extrema of Hamiltonian and corresponding steepness values from the numerical computations.

n	$\frac{H}{L}$ (LH)	$\mathcal{H}$ (LH)
1	1.36258683901074e-01	4.64823018228553e-01
2	1.40827871097976e-01	4.57706391816943e-01
3	1.41061656416396e-01	4.57793945537506e-01
4	1.41074235010001e-01	4.57792868390338e-01

Table 4.3: Predictions of Longuet-Higgins (LH) theory first improve with proximity to the limiting wave, but lack of significant digits in the formula (4.33) results in loss of accuracy close to the limiting wave.

differentiate the formula (4.33) with respect to ϵ to determine the extrema points of Hamiltonian:

$$\frac{\partial \mathcal{H}}{\partial \epsilon} = 0, \quad \text{when} \quad \tan\left(2.143 \ln \epsilon + 1.59\right) = 1.4, \tag{4.35}$$

the theoretical predictions improve with proximity of the limiting wave, however more digits are required for accurate approximation close to the limiting wave.

4.2.2 Linearization Around Stokes Wave in a Moving Frame of Reference

The equations (1.13)–(1.14) can be linearized around a Stokes solution of arbitrary height to determine the spectrum of the linearized operator. This investigation was studied in the works Longuet-Higgins [27], Tanaka [28] and Longuet-Higgins and Tanaka [1], and has led to the conclusion that Stokes waves become linearly unstable

due to appearance of real eigenvalues at extremal points of the Hamiltonian.

The linearization around the Stokes solution is written in the moving frame, where the Stokes wave is a stationary solution. In the frame moving with speed c the unknown functions are dependent on $u - ct$ and given by $R(u,t) = R(u - ct, t)$ and $V(u,t) = V(u - ct, t)$. The equations of motion now have the form:

$$R_t = (c + iU)R_u - iU_u R, \tag{4.36}$$

$$V_t = (c + iU)V_t - iB_u R + g(R - 1). \tag{4.37}$$

To find the linearization operator we consider:

$$R(u,t) = R(u) + \delta R, \quad \text{and} \quad V(u,t) = V(u) + \delta V, \tag{4.38}$$

where $R(u)$ and $V(u)$ are independent of time in a frame moving with the crest of the Stokes wave and correspond to the Stokes wave solution. The functions δR and δV are assumed small and are time–dependent. The linearization operator is found by substitution of the equations (4.38) into equations (4.36)–(4.37) and yields:

$$\frac{\partial \delta R}{\partial t} = i\left[\delta U R_u + (U - ic)\,\delta R_u - \delta R U_u - R\delta U_u\right], \tag{4.39}$$

$$\frac{\partial \delta V}{\partial t} = i\left[\delta U V_u + (U - ic)\,\delta V_u - \delta R B_u - R\delta B_u\right] + g\delta R, \tag{4.40}$$

where δU and δB are given by:

$$\delta U = \hat{P}^-(\delta R\bar{V} + R\delta\bar{V} + \delta\bar{R}V + \bar{R}\delta V), \quad \delta B = \hat{P}^-(\delta V\bar{V} + V\delta\bar{V}). \tag{4.41}$$

The perturbations δR and δV are written in the form:

$$\delta R(u,t) = e^{\lambda t}\delta R_\lambda(u) + e^{\bar{\lambda} t}\delta R_{\bar{\lambda}}(u), \tag{4.42}$$

$$\delta V(u,t) = e^{\lambda t}\delta V_\lambda(u) + e^{\bar{\lambda} t}\delta V_{\bar{\lambda}}(u), \tag{4.43}$$

where λ is a complex constant, and $\bar{\lambda}$ is its complex conjugate. The eigenvalue problem is found by substitution of these formulas into linearized equations for R_t (4.39)

and collecting terms with exponentials $e^{\lambda t}$ and $e^{\bar{\lambda} t}$:

$$\lambda \delta R_\lambda = i\left[\delta U_\lambda R_u + (U - ic)(\delta R_\lambda)_u - \delta R_\lambda U_u - R(\delta U_\lambda)_u\right], \tag{4.44}$$

$$\lambda \delta \bar{R}_{\bar{\lambda}} = -i\left[\delta \bar{U}_{\bar{\lambda}} \bar{R}_u + (\bar{U} + ic)(\delta \bar{R}_{\bar{\lambda}})_u - \delta \bar{R}_{\bar{\lambda}} \bar{U}_u - \bar{R}(\delta \bar{U}_{\bar{\lambda}})_u\right], \tag{4.45}$$

and similarly for the equation for V_t (4.40) and collecting terms at the respective exponentials:

$$\lambda \delta V_\lambda = i\left[\delta U_\lambda V_u + (U - ic)(\delta V_\lambda)_u - \delta R_\lambda B_u - R(\delta B_\lambda)_u\right] + g\delta R_\lambda, \tag{4.46}$$

$$\lambda \delta \bar{V}_{\bar{\lambda}} = -i\left[\delta \bar{U}_{\bar{\lambda}} \bar{V}_u + (\bar{U} + ic)(\delta \bar{V}_{\bar{\lambda}})_u - \delta \bar{R}_{\bar{\lambda}} \bar{B}_u - \bar{R}(\delta \bar{B}_{\bar{\lambda}})_u\right] + g\delta \bar{R}_{\bar{\lambda}}. \tag{4.47}$$

and

$$\delta U_\lambda = \hat{P}^-(\delta R_\lambda \bar{V} + R\delta \bar{V}_{\bar{\lambda}} + \delta \bar{R}_{\bar{\lambda}} V + \bar{R}\delta V_\lambda), \tag{4.48}$$

$$\delta \bar{U}_{\bar{\lambda}} = \hat{P}^+(\delta \bar{R}_{\bar{\lambda}} V + \bar{R}\delta V_\lambda + \delta R_\lambda \bar{V} + R\delta \bar{V}_{\bar{\lambda}}), \tag{4.49}$$

$$\delta B_\lambda = \hat{P}^-(\delta V_\lambda \bar{V} + V\delta \bar{V}_{\bar{\lambda}}), \tag{4.50}$$

$$\delta \bar{B}_{\bar{\lambda}} = \hat{P}^+(\delta \bar{V}_{\bar{\lambda}} V + \bar{V}\delta V_\lambda), \tag{4.51}$$

The resulting eigenvalue problem is posed for a vector of four functions,

$$\delta \mathbf{f} = \left(\delta R_\lambda, \delta \bar{R}_{\bar{\lambda}}, \delta V_\lambda, \delta \bar{V}_{\bar{\lambda}}\right)^T.$$

The eigenvalue problem is solved numerically, and we discuss the details of the implementation in the section "Numerical Method".

4.2.3 Main Results

The works by Tanaka [28], and Longuet-Higgins and Tanaka [1] demonstrated that eigenvalues become unstable at the extrema of the Hamiltonian, $\mathcal{H}$ as a function of H/L, where $\mathcal{H}$ is given by the formula:

$$\mathcal{H} = \frac{1}{2}\int \psi \hat{k} \psi \, du + \frac{g}{2}\int y^2 x_u \, du, \tag{4.52}$$

and observed two unstable eigenmodes associated with the first two extrema of $\mathcal{H}$. Further approach to the limiting wave is difficult because of the slow convergence rate of Fourier coefficients of the Stokes wave. We have solved the eigenvalue problem associated with linearization of the dynamical equations of motion on the background of a collection of Stokes waves that are in close vicinity to the limiting wave, confirming the numerical observations of Longuet-Higgins and Tanaka [1]. In the Figure 4.2, we show the square of the first (left panel) and second (right panel) unstable eigenvalues as a function of H/L. In both panels we include data for the first and second unstable eigenvalues (blue squares) from Longuet-Higgins and Tanaka [1]. We zoom into regions where λ_1^2, λ_2^2 cross the horizontal axis and switch sign from negative to positive. We include data points below zero to show that unstable eigenmodes switch form being purely imaginary to real. In the zoomed plots, we fit the numerical data around the instability threshold to a function $f(H/L) = a(H/L - H_n/L)$ where for the first unstable eigenvalues $a = 21.5956$, $H_1/L = 0.136603552635709$, and $a = 407.643$, $H_2/L = 0.140796170578837$ for the second unstable eigenvalue. We get that the first 6 decimal digits of H_1/L and H_2/L match the positions of Hamiltonian extrema (by comparing results from the table 4.2) and confirm numerical observations of Longuet-Higgins and Tanaka [1].

We were able to solve the eigenvalue problem for Stokes waves around the third extremum of the Hamiltonian as well. In the left panel of Figure 4.3, we show the third unstable eigenvalue and zoom into the region where λ_3^2 intersects the horizontal axis. We fit the data around the third instability threshold to a function $f(H/L) = a(H/L - H_3/L)$ with $a = 7800$, $H_3/L = 0.141049633798808$. The first 6 digits of $s_3 = H_3/L$ match the position of the second maximum of $\mathcal{H}$, and thus it confirms that unstable eigenmodes occur at extrema of the Hamiltonian.

We have found that unstable eigenvalues appear as a result of collision of a pair of imaginary eigenvalues at the origin in the complex plane. The right panel

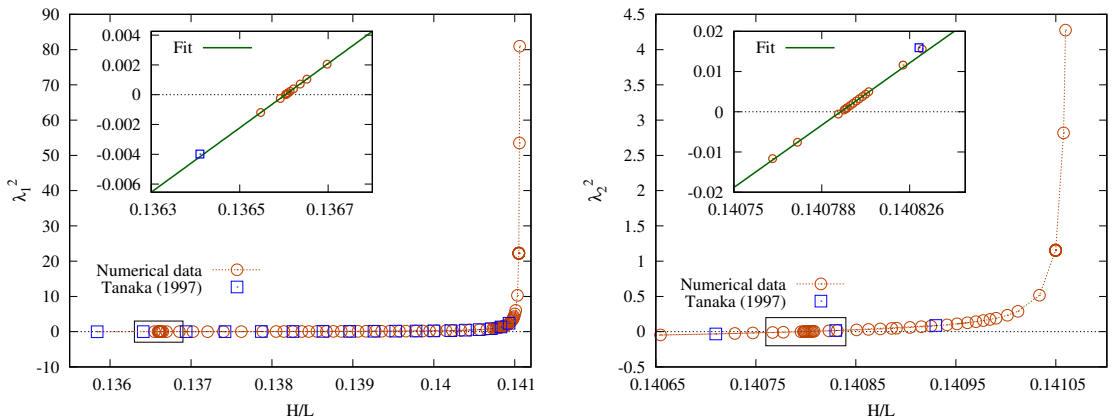

Figure 4.2: (Left) The square of first eigenvalue $\lambda_1^2(H/L)$ to cross the instability threshold at $H/L = 0.1366035$ when Hamiltonian goes through the first extremum. The eigenvalues computed in present work (orange circles), the numerical data of the work [1] (blue squares) and numerical fit of the data (green line). (Right) The square of the second eigenvalue $\lambda_2^2(H/L)$ that becomes unstable at the value of $H/L = 0.1408279$ when $\mathcal{H}$ goes through a second extremum, the numerical data of the work [1] and numerical fit of the data (green line).

of Figure 4.3 illustrates a snapshot of the smallest magnitude eigenvalues of the linearized operator as they cross zero to collide and produce unstable eigenmodes near the first extremum of the Hamiltonian in the vicinity of the limiting wave. We plot real and imaginary parts of eigenvalues on the vertical and horizontal axes respectively. Green, yellow and red circles represent eigenvalues that correspond to 3 different steepnesses. Blue pentagons show purely imaginary stable eigenvalues that are motionless with respect to change of steepness s. The direction in which unstable eigenmodes move as s grows toward the limiting Stokes wave is shown by the arrows.

We found that all eigenvalues that become unstable follow the same curve after a proper normalization. In Figure 4.4, we plot the first (green circles), second (yellow triangles) and third (blue triangles) eigenvalues and data from Longuet-Higgins and Tanaka [1], normalizing the horizontal variable to $\frac{s_{max}-s}{s_{max}-s_n}$, where s_{max} is the steepness

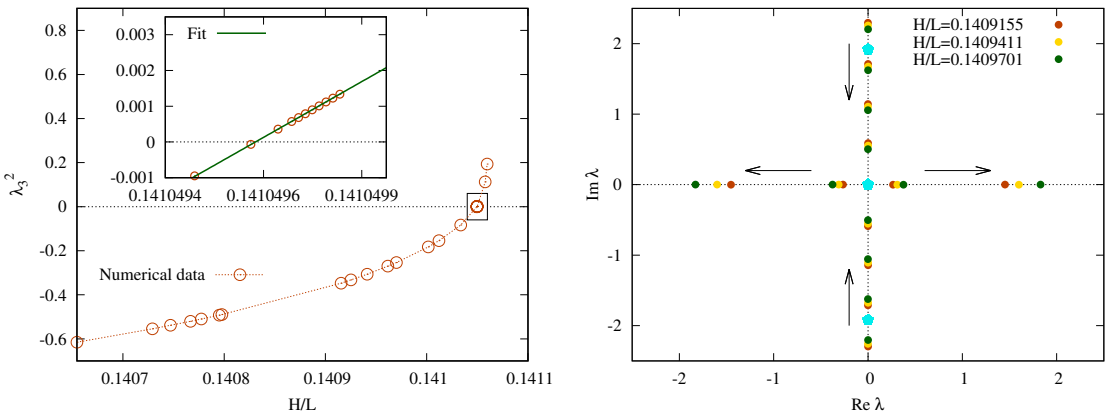

Figure 4.3: (Left) The square of the third eigenvalue to cross the instability threshold at $H/L = 1.410496$ at the third extremum of the Hamiltonian. Circles are numerical solutions of eigenvalue problem, and solid line is a fit to power law. (Right) A snapshot of eigenvalues near the origin for a linearization just after the second extremum of the Hamiltonian, $\mathcal{H}$. It shows that there are two kinds of eigenvalues, the ones that are sensitive to small changes in H/L (red, yellow and green), and the ones that remain stationary (cyan). It is evident that more eigenvalues are moving to the origin to collide and produce more unstable eigenmodes.

of the limiting Stokes wave, and s_n with $n = 1, 2, 3$ is the steepness of the Stokes waves at the extremum in the Hamiltonian.

4.2.4 Numerical Method

We solve the eigenvalue problem given by the equations (4.44)–(4.47). The background Stokes wave is computed numerically in quadruple precision using the Newton-CG method (Dyachenko *et al* [17]). The functions $R(u)$ and $V(u)$ are represented by Fourier series in q, that is related to u as described by Lushnikov *et al* in [19] by the means of formula:

$$\tan\frac{u}{2} = l\tan\frac{q}{2}, \tag{4.53}$$

where l is a parameter chosen in such a way so the decay rate of Fourier coefficients is the fastest. We use a uniform grid for q, so that we may use fast Fourier transform (FFT) to apply the linearized operator efficiently to the basis of complex exponentials. A uniform grid in q translates to a highly concentrated grid in u, so that the singularity of the Stokes wave is resolved accurately. After a Stokes wave has been found, we solve the eigenvalue problem for the linearized problem, which may be written in matrix form as follows:

$$\hat{A}\delta\mathbf{f} = \lambda\delta\mathbf{f}, \tag{4.54}$$

where $\hat{A}$ is a 4×4 operator matrix. It can be reduced to a matrix of coefficients A by applying $\hat{A}$ to the standard Fourier basis in q.

The eigenvalue problem is solved by means of shift–and–invert technique (see Saad [66]). We consider the modified eigenvalue problem:

$$(A - \sigma I)^{-1}\mathbf{x} = \nu\mathbf{x} \tag{4.55}$$

where σ is a guess chosen such that $\sigma \neq \lambda$, and eigenvalues have the form,

$$\nu_j = \frac{1}{\lambda_j - \sigma}. \tag{4.56}$$

These eigenvalues have the largest magnitude when λ_k is closest to σ. We use ARPACK subroutine [67], [68] (which is based on the Arnoldi method (Arnoldi [69], Trefethen and Bau [70])) to get ν_j. Once we find ν_j, we can recover $\lambda_j = \sigma + \frac{1}{\nu_j}$ of the original eigenvalue problem. Currently, we use LU factorization for $A - \sigma I$, but we want to improve to a matrix–free implementation of the eigenvalue solver.

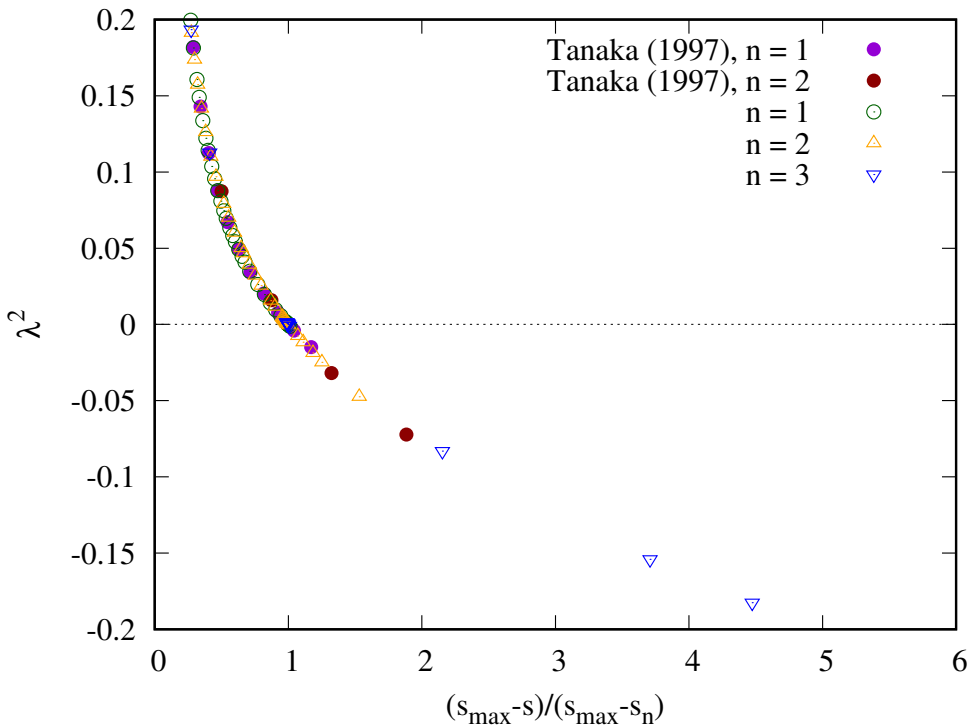

Figure 4.4: Eigenvalues found by Longuet-Higgins and Tanaka [1] are marked by purple circles (first to become unstable $n = 1$) and red circles (second to become unstable $n = 2$). The first eigenvalues ($n = 1$) to become unstable are shown with green circles. The second ($n = 2$) and third ($n = 3$) eigenvalues are yellow triangles and blue triangles respectively. On horizontal axis we use normalized variable $\frac{s_{max}-s}{s_{max}-s_n}$ where $n = 1, 2, 3$. All eigenvalues lie on a single curve that describes their position particularly well at $s = s_n$.

Chapter 5

Conclusion of Part I

We computed the first three unstable eigenmodes of linearization operator of Stokes Waves, and demonstrated that they occur for steepnesses that correspond to the extrema of the Hamiltonian verifying and extending observations of Longuet-Higgins and Tanaka [1]. We see that unstable eigenvalues appear as a result of collision of a pair of imaginary eigenvalues at the origin in the complex plane. Our conjecture based on the results in Figure 4.4 is that all eigenvalues (that turn into unstable eigenvalues) lie on a single curve after a change of variable from steepness (4.31) s to $\frac{s_{max}-s}{s_{max}-s_n}$ where s_{max} is the steepness of the limiting Stokes wave, and s_n (with $n = 1, 2, 3$) is the steepness of Stokes waves at extrema in the Hamiltonian. Our simulations suggest a power law for $\lambda_n^2 \sim \frac{1}{s_{max}-s}$ in the vicinity of the limiting wave for all n, but further analytical work is required to develop a theory that would explain these observations.

Computation of Stokes waves near the third extremum becomes tedious, and numerical solution of the eigenvalue problem becomes numerically costly. The present approach can be improved by employing the conformal map suggested in Hale and Tee [71], so that many more extrema can be resolved. The present approach can

be extended to Stokes waves with constant vorticity where the conformal variable approach has been discovered in the work Dosaev *et al* [72]. It is worthwhile to mention that a problem of stability of Stokes waves is of particular importance in the subharmonic context (Benjamin and Feir [24]), however a different approach has to be developed. In order to consider subharmonic perturbations, the problem has to be considered on an infinite line rather than periodic interval which is outside of the scope of the present work.

For a generic plane wave we have found that the question of formation of a Stokes wave to be quite complicated. Long time dynamics of a plane wave results in a solution that may be represented as a Stokes wave with a significant perturbation. However, the splitting of the solution into a Stokes wave and the perturbation is nontrivial. We have found that matching the potential energy of the Stokes wave to the time–averaged potential energy of the solution is the best criterion. We plan to study the Hamiltonian of the perturbation, and determine the equations of motion for the perturbation. The question of whether the perturbations are absorbed into the Stokes wave remains open.

Part II

Split-Step and Hamiltonian Integration Methods for Simulation of Nonlinear Schrödinger Equation

Chapter 1

Introduction

1.1 Problem Formulation

As was mentioned before, NLSE is one of the most important equations describing nonlinear waves. In the part II, we present the work published in our paper Semenova *et al* [56].

Let us consider NLSE in its simplest form (rescaling of coordinate, time, and amplitude can bring NLSE into this form without loss of generality):

$$i\Phi_t + \Phi_{xx} + \gamma|\Phi|^2\Phi = 0, \tag{1.1}$$

where $\Phi(x,t)$ is a complex function, $\gamma = \pm 1$ denotes the focusing and defocusing NLSE respectively, and subscript denotes partial derivative with respect to x and t. The latter equation is solved on an interval $x \in [-L, L]$ subject to periodic boundary conditions, and $t \in [0, T]$. We consider NLSE in one spatial dimension, although both methods (HIM and SS2) are applicable to any dimensions (for example, HIM was originally formulated for a 2D problem in Dyachenko *et al* [51]).

1.2 Constants of Motion

The Hamiltonian $\mathcal{H}$ and the number of particles $\mathcal{N}$ given by:

$$\mathcal{H} = \int \Big(|\Phi_x|^2 - \frac{\gamma}{2}|\Phi|^4 \Big) dx \quad \text{and} \quad \mathcal{N} = \int |\Phi|^2 \, dx, \tag{1.2}$$

are conserved quantities for (1.1). We integrate over one spatial period $[-L, L]$ and drop the integration limits for brevity. The NLSE is an integrable system (Shabat and Zakharov [73]), and it has infinitely many nontrivial integrals of motion, that may be used to track accuracy of a numerical simulation. We consider the first two nontrivial integrals of motion, that are given by Shabat and Zakharov [73], Novikov *et al* [74]:

$$\mathcal{C}_4 = \int \left[\Phi \bar{\Phi}_{xxx} + \frac{3\gamma}{2} \Phi \bar{\Phi}_x |\Phi|^2 \right] dx, \tag{1.3}$$

$$\mathcal{C}_5 = \int \left[|\Phi_{xx}|^2 + \frac{\gamma^2}{2}|\Phi|^6 - \frac{\gamma}{2}\left(|\Phi|_x^2\right)^2 - 3\gamma |\Phi|^2 |\Phi_x|^2 \right] dx. \tag{1.4}$$

We denote them $\mathcal{C}_4$ and $\mathcal{C}_5$ because the first three are trivial integrals of motion: the number of particles $\mathcal{N}$, the Hamiltonian $\mathcal{H}$ (1.2), and the momentum.

1.3 Exact Solutions of NLSE

Shabat and Zakharov show in [73] that NLSE has soliton solutions, and when the equation (1.1) is considered on an infinite spatial interval, it may be solved by means of the inverse scattering transform. We use solutions of NLSE that decay at $x \to \pm\infty$, such as N-soliton solutions derived by Shabat and Zakharov in [73], and they may be used on a periodic interval when the magnitude of $|\Phi|$ is close enough to zero at the endpoints $x = \pm L$. In this work we consider the case when $\gamma = 1$ in the equation (1.1).

The one-soliton solution is given by the formula:

$$\Phi = \frac{\sqrt{2\lambda}e^{i\left(\frac{1}{2}vx+\left(\lambda-\frac{1}{4}v^2\right)t+\Phi_0\right)}}{\cosh\left[\sqrt{\lambda}\,(x-vt-x_0)\right]}, \tag{1.5}$$

where x_0, and v are the constants that determine the initial position and the propagation speed of the soliton, and the constants λ and Φ_0 determine the soliton amplitude and the initial phase respectively.

Another exact solution of (1.1) on infinite line is the two-soliton solution which can be obtained by the dressing method [75] and is given by the formula:

$$\Phi = \frac{\left[1+\dfrac{e^{\eta_2+\bar{\eta}_2}(p_1-p_2)^2}{2(p_1+\bar{p}_2)^2(p_2+\bar{p}_2)^2}\right]e^{\eta_1}+\left[1+\dfrac{e^{\eta_1+\bar{\eta}_1}(p_1-p_2)^2}{2(\bar{p}_1+p_2)^2(p_1+\bar{p}_1)^2}\right]e^{\eta_2}}{D}, \tag{1.6}$$

where D has the form:

$$D = 1+\frac{e^{\eta_1+\bar{\eta}_1}}{2(p_1+\bar{p}_1)^2}+\frac{e^{\eta_2+\bar{\eta}_2}}{2(p_2+\bar{p}_2)^2}+\frac{e^{\eta_1+\bar{\eta}_2}}{2(p_1+\bar{p}_2)^2}+\frac{e^{\bar{\eta}_1+\eta_2}}{2(\bar{p}_1+p_2)^2}+ \\ +\frac{e^{\eta_1+\bar{\eta}_1+\eta_2+\bar{\eta}_2}|p_1-p_2|^4}{4(p_1+\bar{p}_1)^2(p_2+\bar{p}_2)^2|p_1+\bar{p}_2|^4} \tag{1.7}$$

and η_1,η_2 are determined by the expression:

$$\eta_{1,2} = p_{1,2}\,x + ip_{1,2}^2\,t + a_{1,2}, \tag{1.8}$$

here $p_{1,2}$ and $a_{1,2}$ are complex constants. The width and the propagation speed of solitons are defined by the real and the imaginary parts of p_1 and p_2 respectively. The initial positions of the first and second soliton are described by a_1 and a_2.

Chapter 2

Description of Numerical Methods

We describe two numerical methods the second order Split Step method (SS2) and the Hamiltonian integration method (HIM) that we later compare in the chapter "Numerical Methods Performance".

2.1 Numerical Solution on Periodic Interval

We use Fourier series to approximate $\Phi(x,t)$ on the periodic interval $x \in [-L, L]$ using a pseudo spectral approach by means of the discrete Fourier transform (DFT) that is computed using the fast Fourier transform library FFTW [76]. In physical space we use a uniform grid,

$$x_j = \frac{2L}{N} j - L \quad \text{where } j = 0, \ldots N-1 \tag{2.1}$$

to discretize the interval $[-L, L]$. We introduce a grid function,

$$\Phi_j^n = \Phi(x_j, n\Delta t), \tag{2.2}$$

where Δt is an elementary time step.

2.2 Split Step Method

In the SS2 method, the linear and nonlinear terms of (1.1) are treated separately in a style of Strang splitting [52].

We define $\hat{L} = i\partial^2/\partial x^2$ to be the operator for the linear term and $\hat{N} = i\gamma|\Phi|^2$ represent the operator for the nonlinear term of the equation (1.1), and it can be rewritten as $\Phi_t(x,t) = (\hat{L}+\hat{N})\Phi(x,t)$. This equation has the formal solution $\Phi(x,t+\Delta t) = e^{(\hat{L}+\hat{N})\Delta t}\Phi(x,t)$ on a time step Δt. In the SS2 method (Taha and Ablowitz [46]) we approximate the exponential term by the product of separate exponents:

$$e^{(\hat{L}+\hat{N})\Delta t} = e^{\hat{L}\frac{\Delta t}{2}}e^{\hat{N}\Delta t}e^{\hat{L}\frac{\Delta t}{2}} + \frac{\Delta t^3}{12}\{[\hat{L},[\hat{N},\hat{L}]] + \frac{1}{2}[\hat{N},[\hat{N},\hat{L}]]\} + \ldots, \tag{2.3}$$

that is accurate up to third order in time. This is a special case of application of the Campbell-Baker-Hausdorff formula (Varadarajan [77]). By doing this, the evolution of the linear part and nonlinear part on the step Δt can be carried out separately. In the context of NLSE this is particularly attractive because both evolutions can be carried out analytically. We note that the linear PDE $i\Phi_t = -\Phi_{xx}$, can be solved exactly in the Fourier domain:

$$\Phi_k(t+\Delta t) = e^{-ik^2\Delta t}\Phi_k(t), \tag{2.4}$$

where $\Phi_k(t)$ denotes the Fourier coefficient, corresponding to wavenumber k, of $\Phi(x,t)$. The nonlinear part of (1.1) given by $i\Phi_t = -\gamma|\Phi|^2\Phi$ is an ODE, and can be solved exactly:

$$\Phi(x,t+\Delta t) = e^{i\gamma|\Phi|^2\Delta t}\Phi(x,t). \tag{2.5}$$

Equations (2.4) and (2.5) give us explicit expressions for $e^{\hat{L}}$ and $e^{\hat{N}}$ correspondingly. The only complexity is that these two exact solutions are given in Fourier and coordinate spaces which requires switching between them in order to represent $e^{\hat{L}\frac{\Delta t}{2}}e^{\hat{N}\Delta t}e^{\hat{L}\frac{\Delta t}{2}}$ in (2.3) consecutively.

In a similar manner one may construct higher order split step methods, by alternating linear and nonlinear steps. The SS2 method is stable if the condition,

$$\Delta t \leq \frac{\Delta x^2}{\pi} \tag{2.6}$$

described in Weideman and Herbst [78] is satisfied.

One can note that both steps (linear and nonlinear) in SS2 methods are performing only a rotation of phase, so conservation of the number of particles $\mathcal{N}$ is an intrinsic property of the method.

2.3 Hamiltonian Integration Method

The main feature of the HIM method (introduced in Dyachenko *et al* [51]) is its exact conservation of the Hamiltonian, $\mathcal{H}$, and number of particles, $\mathcal{N}$. This is achieved by requiring that the difference in $\mathcal{H}$ (and $\mathcal{N}$) on subsequent time steps vanishes, the details of the derivation of HIM are given in Appendix B.1. HIM is an implicit scheme:

$$i\frac{\Phi_j^{n+1}-\Phi_j^n}{\Delta t} = -\frac{\left[\Phi_j^{n+1}+\Phi_j^n\right]_{xx}}{2} - \frac{(\Phi_j^{n+1}+\Phi_j^n)(|\Phi_j^{n+1}|^2+|\Phi_j^n|^2)}{4}. \tag{2.7}$$

where Φ_j^n is a grid function defined in (2.2). Equation (2.7) implicitly defines the solution at the subsequent time steps and is solved by means of fixed point iterations. In Fourier space the formula (2.7) transforms into the following expression:

$$\hat{\Phi}_k^{n+1}-\hat{\Phi}_k^n = -\frac{ik^2\Delta t}{2}(\hat{\Phi}_k^{n+1}+\hat{\Phi}_k^n) + \frac{i\Delta t}{4}\hat{F}\left[(\Phi^{n+1}+\Phi^n)(|\Phi^{n+1}|^2+|\Phi^n|^2)\right], \tag{2.8}$$

where $\hat{\Phi}_k^n = \hat{F}\left[\Phi^n\right]$ is the k-th Fourier coefficient of the grid function Φ_j^n. Following the work of Korotkevich *et al* [57], the linear part of the equation (2.8) can be resolved for $\hat{\Phi}_k^{n+1}$ which yields:

$$\hat{\Phi}_k^{n+1} = \frac{1-i\frac{k^2\Delta t}{2}}{1+i\frac{k^2\Delta t}{2}}\hat{\Phi}_k^n + i\frac{\Delta t}{4(1+i\frac{k^2\Delta t}{2})}\hat{F}\left[(\Phi^{n+1}+\Phi^n)(|\Phi^{n+1}|^2+|\Phi^n|^2)\right]. \tag{2.9}$$

We solve the equation (2.9) by fixed point iterations:

$$\hat{\Phi}_k^{n+1,s+1} = \frac{1 - i\frac{k^2\Delta t}{2}}{1 + i\frac{k^2\Delta t}{2}}\hat{\Phi}_k^n + \frac{i\Delta t}{4(1 + i\frac{k^2\Delta t}{2})}\hat{F}\left[(\Phi^{n+1,s} + \Phi^n)(|\Phi^{n+1,s}|^2 + |\Phi^n|^2)\right], \tag{2.10}$$

where s denotes the iteration number and $\hat{\Phi}_k^{n+1,0} = \hat{\Phi}_k^n$. The expression (2.10) is iterated until the residual condition:

$$\left\|\hat{\Phi}_k^{n+1,s+1} - \hat{\Phi}_k^{n+1,s}\right\|_2 = \sqrt{\sum_k \left|\hat{\Phi}_k^{n+1,s+1} - \hat{\Phi}_k^{n+1,s}\right|^2} \leq \varepsilon\,, \tag{2.11}$$

is satisfied. In this formula $\|\cdot\|_2$ denotes the l_2 norm on $[-L, L]$, and ε is the tolerance for fixed point iterations. The initial values $\Phi^{n+1,0}$ are computed using one step of Forward Euler. From the paper [51], the fixed point iterations of HIM converge when the following condition is satisfied,

$$\Delta t < \frac{2}{\sqrt{3}\max_j(|\Phi_j^n|^2)}. \tag{2.12}$$

Derivation of this condition is given in Appendix B.2.

For the time step that satisfies the above condition, the fixed point iterations typically converge in 4 to 6 steps with the tolerance $\varepsilon \leq 10^{-11}$.

Chapter 3

Physical Units Relevant to Optical Fiber

We would like to estimate the characteristic time of a simulation that corresponds to the dynamics of a pulse in a physically realistic fiber. In order to do so we consider a trans–Atlantic fiber described in the reference paper [40] by Lushnikov subject to:

$$iA_z - \frac{1}{2}\beta_2 A_{\tau\tau} + \sigma_1 |A|^2 A = 0\,. \tag{3.1}$$

We use the values for $\beta_2 = -20\,\mathrm{ps}^2\,\mathrm{km}^{-1}$ (the group velocity dispersion) and $\sigma_1 = 1.3 \times 10^{-3}\,\mathrm{km}^{-1}\mathrm{mW}^{-1}$ (the strength of nonlinearity for a fiber) provided in [40].

The dimensionless NLSE given by (1.1) must be rewritten in the original dimensional units. To do that, we consider dimensional units:

$$z = lt,\ \tau = \frac{x}{\omega_0},\ \text{and}\ A = A_0\Phi. \tag{3.2}$$

The derivatives with respect to t and x are given by the formulas:

$$\partial_t = l\partial_z \text{ and } \partial_x = \frac{1}{\omega_0}\partial_\tau, \tag{3.3}$$

and the resulting equation in the dimensional units transforms into:

$$iA_z + \frac{1}{\omega_0^2 l} A_{\tau\tau} + \frac{|A|^2 A}{A_0^2 l} = 0. \tag{3.4}$$

We compare the two equations (3.1) and (3.4) and get that:

$$\beta_2 \left[\frac{ps^2}{km}\right] = \frac{-2}{\omega_0^2 l} \ , \tag{3.5}$$

$$\sigma_1 \left[\frac{1}{km\ mW}\right] = \frac{1}{A_0^2 l} \ , \tag{3.6}$$

where $A_0 = 1\,\mathrm{mW}^{1/2}$. By using the equations (3.5)–(3.6) and the parameters β_2 and σ_1 from the reference paper [40], we find that $l \approx 769\,\mathrm{km}$, $\omega_0^2 = 1.3 \times 10^{-4}\,\mathrm{ps}^{-2}$. We see that it is necessary to simulate the fiber until the dimensionless time $t_{max} \approx 13$ in order to mimic a 10^4 km fiber. The nonlinear time is then given by $t_{NL} = \frac{\pi}{|\Phi|^2} = \frac{\pi}{2|\lambda|}$ which in physical units corresponds to $z_{NL} = t_{NL} l$.

Chapter 4

Hamiltonian Integration Method for MMT Model

In 1997 a new model of one-dimensional dispersive wave turbulence was introduced by Majda, McLaughlin, and Tabak [59]. The MMT equation has the form:

$$i\psi_t = |\partial_x|^{\alpha}\psi + \gamma|\partial_x|^{-\beta/4}\left(||\partial_x|^{-\beta/4}\psi|^2|\partial_x|^{-\beta/4}\psi\right), \tag{4.1}$$

and it can be considered as a generalization of NLSE. Here $\alpha > 0$ and β are real parameters. This model describes a Hamiltonian system with $\mathcal{H}$ given by:

$$\mathcal{H}_{MMT} = \int \left(||\partial_x|^{\alpha/2}\psi|^2 + \frac{\gamma}{2}||\partial_x|^{-\beta/4}\psi|^4\right) dx. \tag{4.2}$$

The MMT conserves the number of particles $\mathcal{N}$ (wave number) similar to NLSE. For $\alpha = 2$ and $\beta = 0$ MMT is almost identical to NLSE. A derivative ∂_x is replaced by a nonlocal operator $|\partial_x|$ in the kinetic energy (4.2), which results in the opposite sign in front of the linear term of (4.1). The MMT model is widely used (see e.g. Zakharov *et al* [79], Lee *et al* [80], Rumpf and Newell [81]) for investigation of the wave turbulence theory Zakharovs *et al* [82] for 2D hydrodynamics with a 1D free surface. We use the same approach as in Appenidx B.1 to the MMT equation and

get the following numerical scheme for HIM:

$$i\frac{\psi_j^{n+1}-\psi_j^n}{\Delta t} = \frac{|\partial_x|^\alpha\psi_j^{n+1}+|\partial_x|^\alpha\psi_j^n}{2}+ \\ +\gamma|\partial_x|^{-\beta/4}\left(\frac{|\partial_x|^{-\beta/4}\psi_j^{n+1}+|\partial_x|^{-\beta/4}\psi_j^n}{2}\frac{||\partial_x|^{-\beta/4}\psi_j^{n+1}|^2+||\partial_x|^{-\beta/4}\psi_j^n|^2}{2}\right). \tag{4.3}$$

Similarly to NLSE, the Hamiltonian $\mathcal{H}_{MMT}$ and the number of particles $\mathcal{N}_{MMT}$ are conserved exactly. Solving for ψ_j^{n+1} in the linear part of (4.3) and applying the same approach as in Appendix B.2, we get the following convergence condition:

$$\Delta t < \frac{2}{|\gamma|\sqrt{3}k_{max}^{\beta/2}\max\limits_j(||\partial_x|^{-\beta/4}\Phi_j^n|^2)}, \tag{4.4}$$

where k_{max} is the maximum of the absolute value of wave number. If $\beta = 0$, the condition for Δt coincides with the convergence condition (2.12) of HIM for NLSE.

Chapter 5

Numerical Methods Performance

In this chapter, various N-soliton ($N = 1, 2, 3$) intial conditions are considered: one soliton, two–soliton and three–soliton solutions. We compare the HIM and SS2 numerical methods by performing a set of experiments with these various initial conditions.

We note that in exact arithmetic, HIM conserves the Hamiltonian $\mathcal{H}$ and number of particles $\mathcal{N}$ up to any precision governed by the tolerance threshold chosen for fixed point iterations, and SS2 conserves the number of particles exactly by the construction of the method. However, in double precision the error in conservation of $\mathcal{H}$ and $\mathcal{N}$ is due to round-off errors inherent to floating point arithmetic. So, the round-off error accumulates in time and causes the number of particles for SS2 and HIM, and the Hamiltonian for HIM to change gradually for all initial conditions.

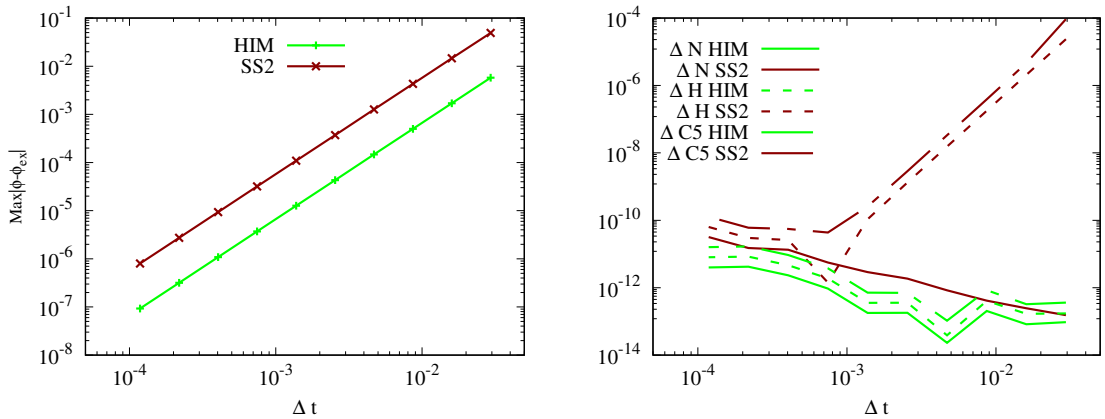

Figure 5.1: (Stationary one-soliton solution on a fully resolved grid) (Left) Convergence rate of numerical methods, HIM (green) and SS2 (red). Both methods have second order convergence, but $\mathcal{L}_\infty$ error in solution is about one order smaller for HIM compared to SS2 for the same time steps. (Right) Error in conserved quantities: number of particles $\mathcal{N}$ (solid), Hamiltonian $\mathcal{H}$ (dotted), and $\mathcal{C}_5$(dash-dotted) for various time steps. When time step is larger than the stability condition of SS2, errors in $\mathcal{H}$ and $\mathcal{C}_5$ start to grow. For HIM, the error is dominated by accumulation of round-off errors and is smaller by several orders of magnitude compared with SS2.

5.1 Stationary One-Soliton Solution

In this simulation we check the convergence rate of HIM and SS2 by running a sequence of simulations with various time steps. As the initial condition we consider a one-soliton solution (1.5) with the following parameters:

$$\lambda = 2, \quad \text{and} \quad \Phi_0 = x_0 = v = 0. \tag{5.1}$$

We run the simulation on a fully resolved (highest harmonics are of round-off level) uniform grid of $N = 2048$ grid points, and $L = 25\pi$. The tolerance for HIM iterations is set to $\varepsilon = 10^{-15}$ and simulation time is $T = 5$. The convergence of both methods is demonstrated in Figure 5.1. We omit $\mathcal{C}_4$ in the Figure 5.1 because this quantity is identically zero for a stationary one-soliton solution. The error in the integrals of motion for the SS2 method is dominated by accumulation of round-off errors for

small Δt, and by the order of method for large Δt as shown in the Figure 5.1. The critical value of Δt for which the transition occurs is close to the stability condition of SS2 method.

5.2 Moving One-Soliton Solution

In these simulations we investigate how the traveling speed v of the one-soliton solution (1.5) affects the accuracy of both numerical methods. It is known that dispersion of waves by the SS2 method is identical to the dispersion of NLSE, while from (2.9) it follows that the dispersion of HIM is only accurate up to third order in $k^2\Delta t$. We expect that for a sufficiently large time step the travel speed of the soliton will deviate from its true value. We show the results of the simulations with various travel speeds in Figure 5.2. The initial data for these simulations is given by (1.5) with parameters:

$$\lambda = 2, \quad \text{and} \quad \Phi_0 = x_0 = 0, \quad \text{and} \quad v \in [0, 5]. \tag{5.2}$$

The computational box size is $L = 25\pi$ and the number of grid points is $N = 2048$. The tolerance for HIM iterations is $\varepsilon = 10^{-14}$ and the simulation time is $T = 100$. The time step for both methods is set to be $\Delta t = \frac{0.5\Delta x^2}{\pi}$.

It should be noted, that soliton velocity is given in dimensionless units. In the left panel of Figure 5.2, we observe that the error in the solution has no dependence on travel speed of the soliton for the SS2 method. For HIM, the error in the solution depends on travel speed which is due to the inexact dispersion relation of HIM method:

$$\omega_{HIM}(k) = \frac{i}{\Delta t} \ln \frac{1 - i\frac{k^2\Delta t}{2}}{1 + i\frac{k^2\Delta t}{2}} = k^2 \left(1 - \frac{k^4\Delta t^2}{12} + \dots\right), \tag{5.3}$$

where $\omega_{HIM}(k)$ is the angular frequency of the k–th Fourier harmonic.

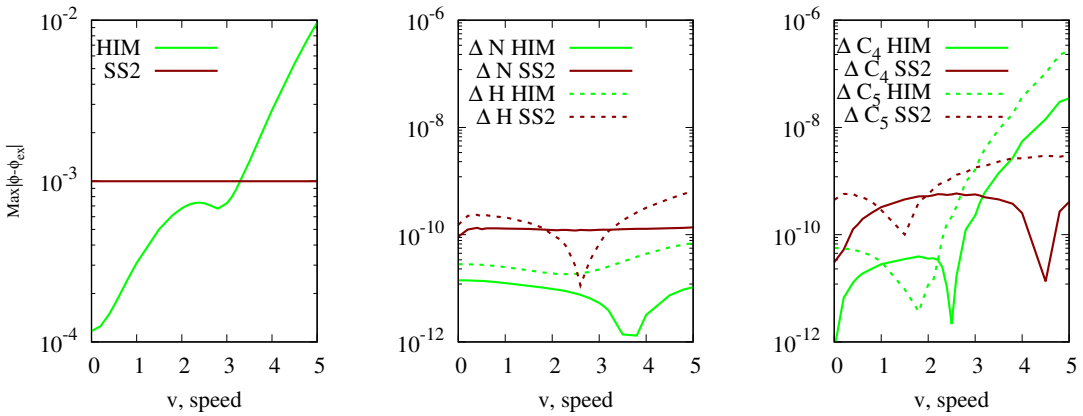

Figure 5.2: (Moving one-soliton solution on a fully resolved grid) (Left) The maximum absolute error of the solution at time $T = 100$ as a function of propagation speed of the soliton. The SS2 method (red) has no dependence of the error on travel speed of the soliton because it naturally captures the dispersion relation of NLSE, while HIM (green) has dispersion relation accurate up to Δt^3. (Center) The error in integral quantities, $\mathcal{N}$ (solid), and $\mathcal{H}$ (dotted) is about seven orders of magnitude smaller than the error in the solution. (Right) The error in integral quantities, $\mathcal{C}_4$ (solid), and $\mathcal{C}_5$ (dotted) is about seven orders of magnitude smaller than the error in the solution. For travel speed $v \leq 3$ HIM and SS2 give comparable accuracy in $\mathcal{C}_4$ and $\mathcal{C}_5$, but HIM behaves worse as soon as v is larger than 3.

In the center panel, we look at the absolute error in integral quantities, $\mathcal{N}$ and $\mathcal{H}$. It is about seven orders of magnitude smaller than the error in the solution. On the right panel, we consider the absolute error in integral quantities, $\mathcal{C}_4$ and $\mathcal{C}_5$. Similarly to $\mathcal{N}$ and $\mathcal{H}$, it is about seven orders of magnitude smaller than the error in the solution. We notice that for travel speed $v \leq 3$, HIM and SS2 give comparable accuracy in $\mathcal{C}_4$ and $\mathcal{C}_5$, but the error in HIM becomes larger as soon as v gets larger than 3. We see dips in the error of integral quantities as a function of speed. The magnitude of the dips is about one order, and it has no correlation to the error in solution, which is significantly larger. Note that the error in the solution does not always correlate with the error in integral quantities.

5.3 Stationary Two-Soliton Solution

In this simulation we demonstrate the difference between SS2 and HIM when the initial data is a two-soliton solution with the following set of parameters:

$$\begin{aligned} &p_1 = 2.0 \text{ and } p_2 = 1.9 \\ &a_1 = 60 + i = -\bar{a}_2. \end{aligned} \tag{5.4}$$

The simulation time is $T = 5$, the solution is underresolved on a grid with $N = 1024$ points. The computation box is $x \in [-L, L]$ where $L = 25\pi$. The time step is $\Delta t = \frac{0.5\Delta x^2}{\pi}$. It is typical to have the solution not resolved to round–off error in long and/or multichannel simulations of light pulses propagating in optical fibers. A smaller number of Fourier harmonics implies faster computations. For this experiment, the smallest amplitudes were of the order 10^{-8}.

We present the results of the simulation in Figures 5.3 - 5.4. At the time $T = 5$, the background radiation around the stationary solitons emitted in SS2 is several orders of magnitude larger than for HIM. The SS2 method radiates waves continuously over the course of the simulation, while the HIM emits localized small amplitude perturbations that travel in the computational box and are reflected and transmitted through the stationary solitons.

In the course of simulation we observe that the error in $\mathcal{H}$ and $\mathcal{C}_5$ is one to two orders of magnitude smaller in HIM than in SS2. The number of particles is better conserved by SS2 and the error is two orders of magnitude smaller.

5.4 Interaction of Two-Solitons

In this section, we study the dynamics of the two-soliton solution (1.6). We present parameters of simulations in sections 5.4.1 - 5.4.3, and discuss results of simulations

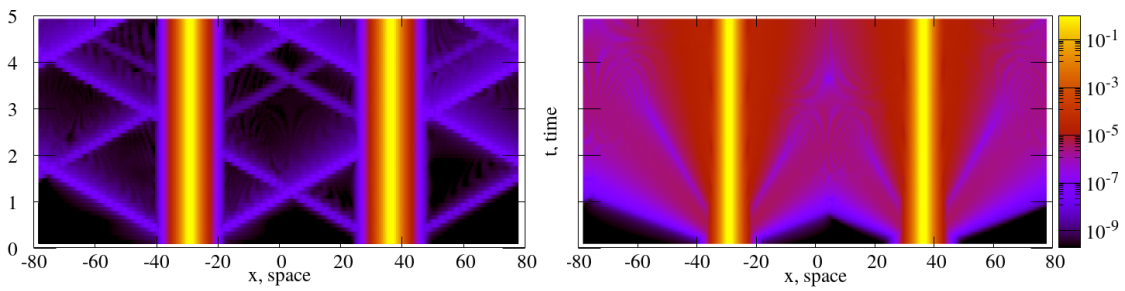

Figure 5.3: (Stationary Two-Soliton Solution on Unresolved Grid) 2D plots of absolute value of the solution $|\Phi(x,t)|$ of NLSE with HIM method (left) and SS2 method (right) with x on horizontal axis and t on vertical. The SS2 method radiates waves continuously over the course of the simulation, while the HIM emits localized small amplitude perturbations that travel in the computational box and are reflected and transmitted through the stationary solitons. At the time $T = 5$, the background radiation around the stationary solitons emitted in SS2 is several orders of magnitude larger than for HIM.

in the section 5.4.4. We use a periodic box with $L = 25\pi$ and $N = 4096$ grid points for fully resolved simulations and $N = 1024$ for unresolved simulations. The time step is $\Delta t = \frac{0.8\Delta x^2}{\pi} < \frac{\Delta x^2}{\pi}$ to satisfy the stability condition (2.6) in all three simulations. The HIM iterations tolerance is $\epsilon = 10^{-12}$.

5.4.1 Collision with Stationary Soliton

The initial condition is given by the two-soliton solution formula (1.6) where one of the solitons is moving towards the other soliton which is at rest. The simulation time is $T = 50$, and over the course of simulation two solitons interact once. We present the results of the simulation in the Figures 5.5 - 5.7.

The parameters for this two–soliton solution are given by:

$$\begin{aligned} p_1 &= 1.2 \text{ and } p_2 = 1.3 + i \\ a_1 &= 2.5 + i \text{ and } a_2 = 65 + i. \end{aligned} \tag{5.5}$$

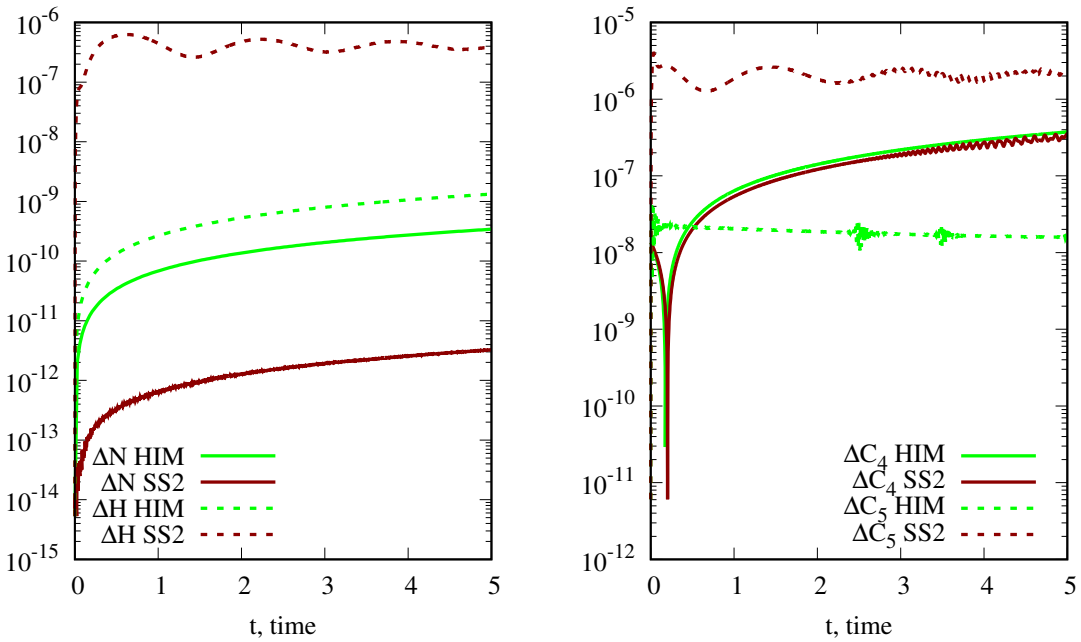

Figure 5.4: (Stationary two-soliton solution on underresolved grid) Conserved integrals in a simulation with initial data (5.4). (Left) The number of particles (solid) and the Hamiltonian (dotted) computed via SS2 (red) and HIM (green). (Right) The integrals $\mathcal{C}_4$(solid) and $\mathcal{C}_5$ (dotted) via SS2 (red) and HIM (green).

5.4.2 Headon Collision of Solitons

The initial condition is given by the two-soliton solution formula (1.6) with solitons moving toward each other. The final time of the simulation is $T = 45$, and two solitons interact once. We present the results of the simulation in Figures 5.8 - 5.10. The parameters for this simulation are the following:

$$p_1 = 1.2 - 0.5i \text{ and } p_2 = 1.3 + i$$
$$a_1 = -20 + i \text{ and } a_2 = 60 + i. \tag{5.6}$$

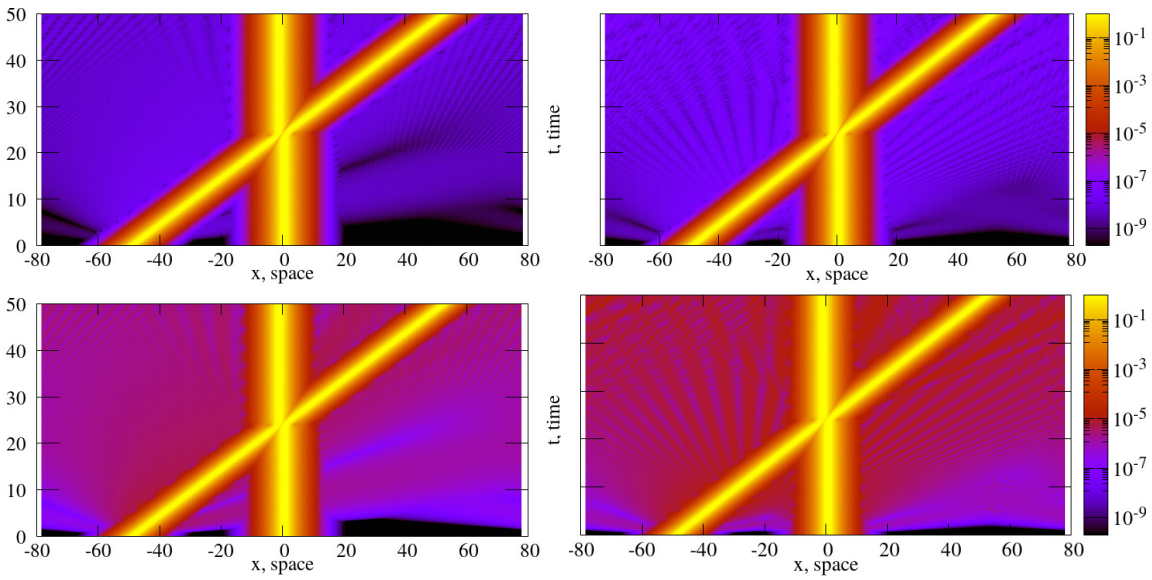

Figure 5.5: (Collision with stationary soliton) (Top) Numerical solution for HIM (left) and SS2 (right) methods on a fully resolved grid $N = 4096$. (Bottom) Numerical solution for HIM (left) and SS2 (right) methods on an underresolved grid with $N = 1024$.

5.4.3 Collision with Pursuing Soliton

The initial condition is given by the two-soliton solution formula (1.6) with one soliton pursuing another soliton. The final time of simulation is $T = 54$. The pursuing soliton overtakes and interacts with the slower soliton once. The results of this simulation are presented in the Figures 5.11 - 5.13, and parameters of the initial condition are as follows:

$$\begin{aligned} p_1 = 1.7 + 0.5i \text{ and } p_2 = 1.9 + i \\ a_1 = 50 + i \text{ and } a_2 = 110 + i. \end{aligned} \tag{5.7}$$

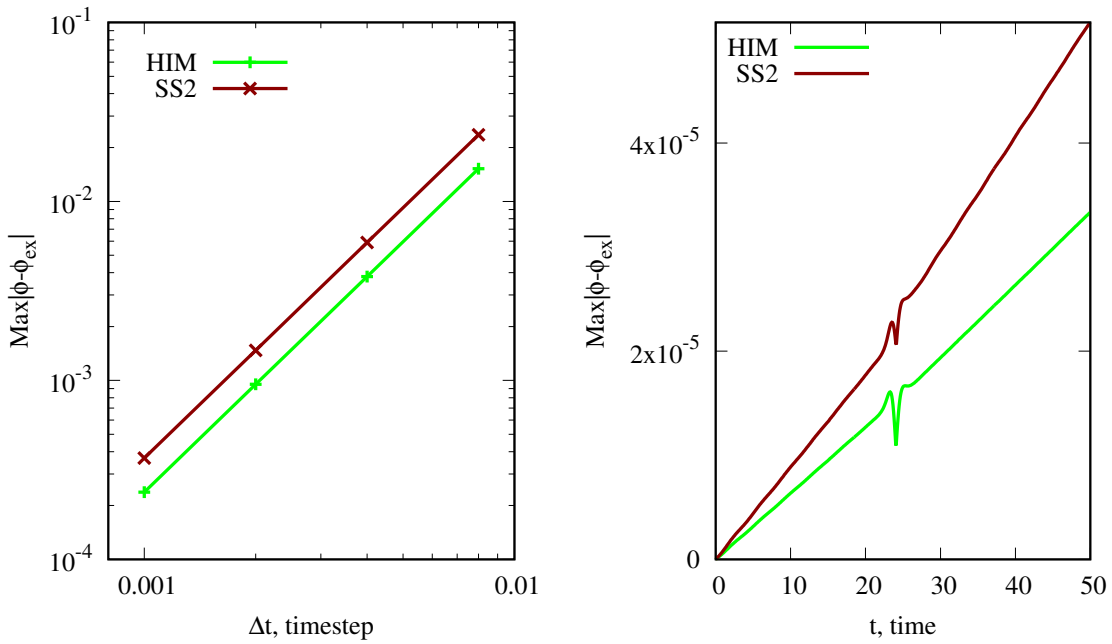

Figure 5.6: (Collision with stationary soliton on a fully resolved grid) (Left) Error in the solution in $\mathcal{L}_\infty$-norm as a function of time step in double-logarithmic scale shows second order convergence in Δt. (Right) Absolute error as a function of time, the solitons interact at approximately $t = 25$. The error vs time is close to a straight line before and after the collision. Its slope, m, changes from $m = 6.35 \times 10^{-7}$ to $m = 7.00 \times 10^{-7}$ for HIM method, and from $m = 8.85 \times 10^{-7}$ to $m = 1.10 \times 10^{-6}$ for SS2. During collision, the phase of the solution changes rapidly and numerical errors grow faster than during soliton propagation. The error in the phase is observed to contribute to the change of the slope of the error after collision.

5.4.4 Results of the Simulations

In the latter sequence of three simulations involving two-soliton collision, we found that the radiation level in the SS2 simulation has been consistently higher than in simulations with the HIM method. In both methods we observe that conservation of integrals of motion $\mathcal{H}$, $\mathcal{N}$, $\mathcal{C}_4$ and $\mathcal{C}_5$ does not imply highly accurate solution in $\mathcal{L}_\infty$-norm. In all the cases we found that the HIM method gives smaller $\mathcal{L}_\infty$ error in the solution by a factor of at least 1.5-2 with the same time step. In order to compute

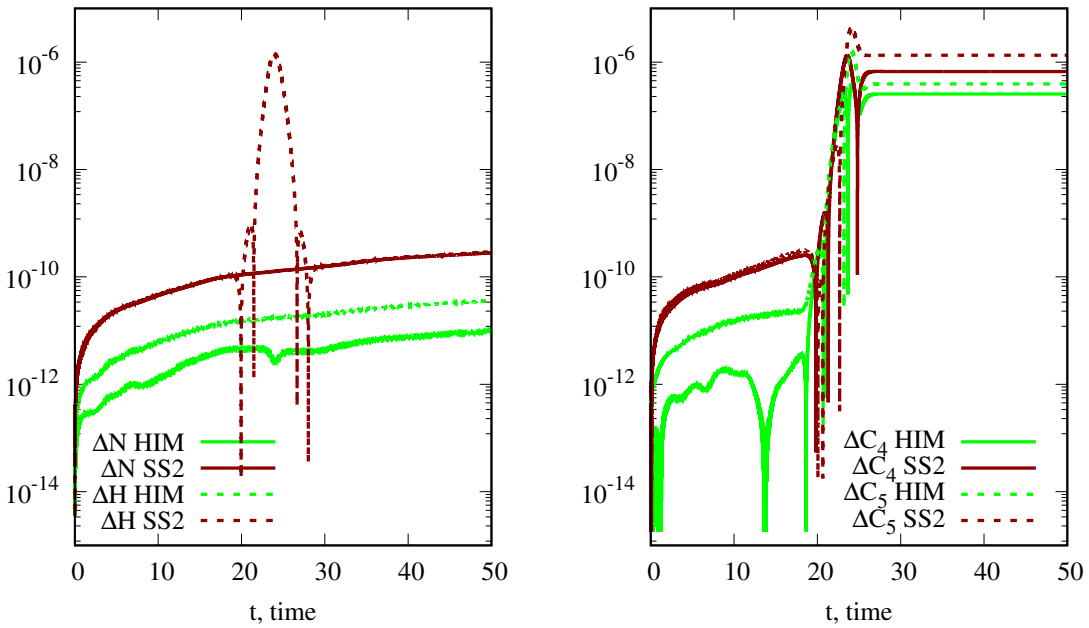

Figure 5.7: (Collision with stationary soliton on a fully resolved grid) The conserved quantities plotted as a function of time over the course of the simulation, note that SS2 demonstrates a strong peak in error in $\mathcal{H}$ at the time of solitons interaction. After the moment of interaction the $\mathcal{C}_4$, and the $\mathcal{C}_5$ exhibit jump and increase in error with in SS2 and HIM.

the $\mathcal{L}_\infty$ error we use the exact solution given by the formula (1.6). The simulation time is chosen so that there is a single collision in the periodic box $[-L, L]$. The formula (1.6) gives a solution on an infinite line, whereas the simulation is performed on a periodic box and thus the simulation time must not exceed the time it takes the solitons to reach the boundary of the box. Moreover, the soliton must still be exponentially small near the end of the box, so that the comparison with the exact formula is applicable. During collision, the phase of the solution changes rapidly and numerical errors grow faster than during soliton propagation. The error in the phase is observed to contribute to the change of the slope of the error after collision.

Despite the $\mathcal{L}_\infty$ error of the solution not being smaller than 10^{-5}, we observe that the integrals of motion $\mathcal{H}, \mathcal{N}$ are conserved up to 5×10^{-10}. Nevertheless, at the time

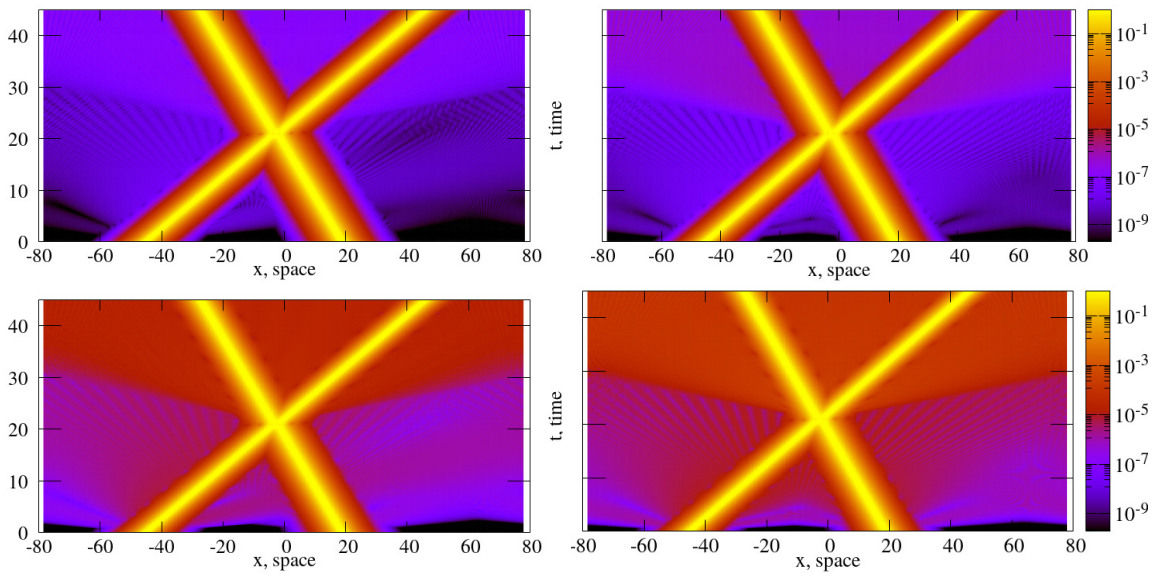

Figure 5.8: (Headon collision of solitons) (Top) Numerical solution for HIM (left) and SS2 (right) methods on a fully resolved grid $N = 4096$. (Bottom) Numerical solution for HIM (left) and SS2 (right) methods on an underresolved grid with $N = 1024$.

of collision we find that $\Delta\mathcal{H}$ experiences a jump up to 5 orders of magnitude in the SS2 method, while in HIM it is conserved by construction of the method. Both methods exactly conserve $\mathcal{N}$ aside from accumulation of round-off errors over the course of simulations. The two nontrivial integrals of motion, $\mathcal{C}_4$ and $\mathcal{C}_5$ are not conserved exactly, nevertheless we observe that until the time of collision these quantities vary only in 9-th decimal place. After the collision these values demonstrate a large jump (up to four orders of magnitude) in both methods. Unlike the Hamiltonian, $\mathcal{H}$, in the SS2 method, these integrals do not revert to their original values after the collision.

5.5 Three Solitons Interaction Simulation

It is known that solitons of the NLSE interact as particles, and interchange momenta during collision [74]. The details of the process can be complicated, but once

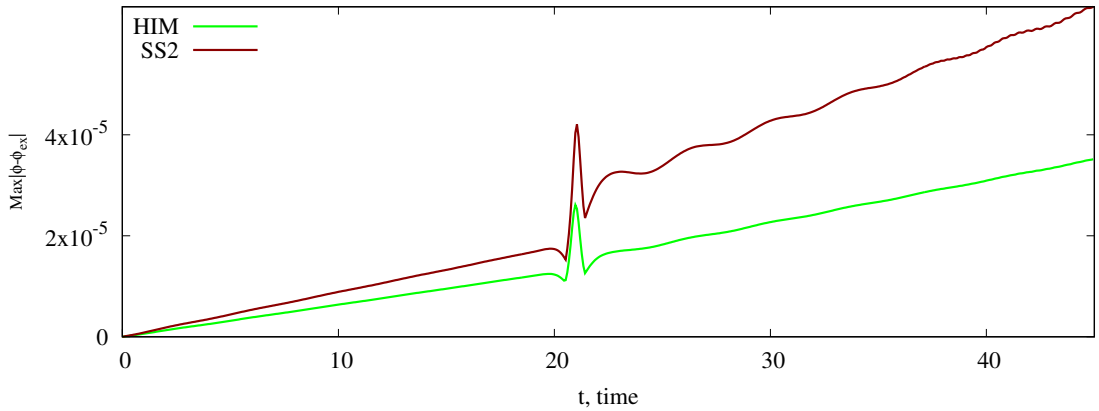

Figure 5.9: (Headon collision of solitons on a fully resolved grid) Error in $\mathcal{L}_\infty$-norm of the solution vs time computed for SS2 (red) and HIM (green) methods. The collision occurs at the time approximately $t = 21$ where we observe a spike in the error. The error vs time is close to a straight line before and after collision. Its slope, m changes from $m = 8.85 \times 10^{-7}$ to $m = 1.5 \times 10^{-6}$ for SS2 method, and from $m = 6.3 \times 10^{-7}$ to $m = 8.3 \times 10^{-7}$ for HIM method.

the solitons move sufficiently far from each other, they behave like separate pulses propagating without change of shape.

In dimensionless units the one–soliton solution is given by (1.5). For this simulation, the initial condition is the sum of three distinct one–soliton solutions:

$$\Phi(x, t = 0) = \Phi_1 + \Phi_2 + \Phi_3, \tag{5.8}$$

where $\Phi_{1,2,3}$ are given by (1.5) with the following set of parameters:

$$\lambda_1 = 2.4,\ \lambda_2 = 2.9,\ \lambda_3 = 3.2, \tag{5.9}$$

$$v_1 = 0,\ v_2 = 0,\ v_3 = \frac{2}{3}, \tag{5.10}$$

$$x_{0,1} = 40,\ x_{0,2} = -20,\ x_{0,3} = -60, \tag{5.11}$$

and zero initial phases. This set of parameters gives us two stationary solitons and one moving. To make sure that we use an approximation of a three-soliton solution

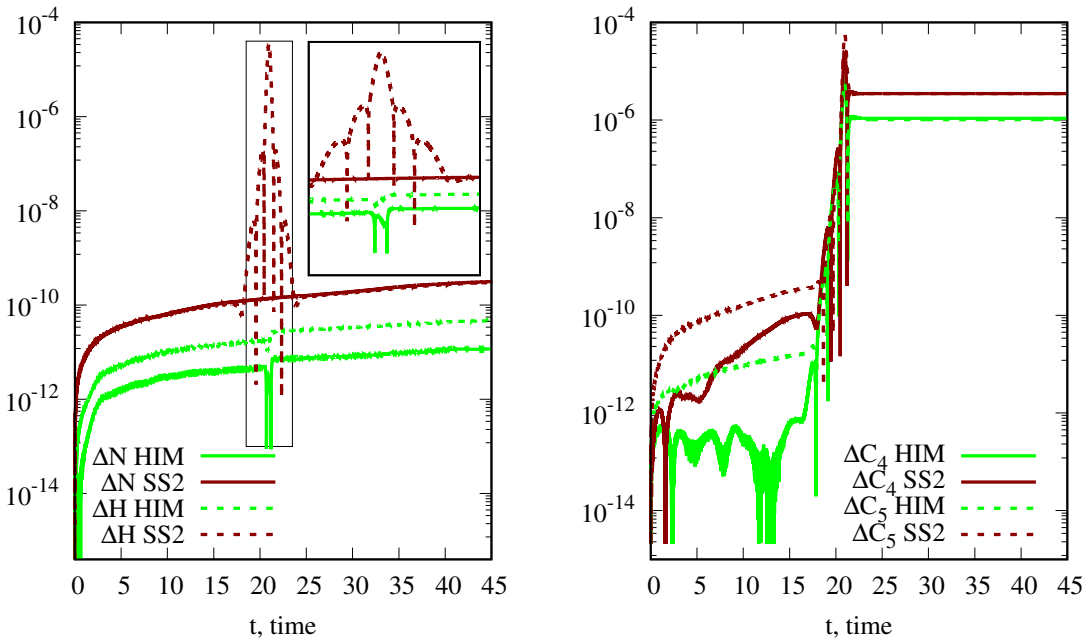

Figure 5.10: (Headon collision of solitons on a fully resolved grid) The conserved quantities (left) $\Delta\mathcal{N}$ (solid), $\Delta\mathcal{H}$ (dotted), and (right) $\Delta\mathcal{C}_4$ (solid), and $\Delta\mathcal{C}_5$ (dotted) as a function of time over the course of the simulation with HIM (green) and SS2 (red). Note that SS2 demonstrates a strong peak in error in $\mathcal{H}$ at the time of soliton interaction. After the interaction time the $\mathcal{C}_4$, and the $\mathcal{C}_5$ exhibit large error with both SS2 and HIM.

on a periodic boundary, we make the overlap between solitons about 10^{-16} and at the boundary $|\Phi(x, t = 0)| \approx 10^{-16}$.

After using the formulas (3.2), we translate this initial data to dimensional units. In the dimensional units the characteristic widths, τ_c, and amplitudes, A, are given by:

$$\tau_c = \frac{1}{\omega_0\sqrt{\lambda}} \approx 50\,\mathrm{ps}$$
$$A = \sqrt{2\lambda}A_0 \approx 2.5\,\mathrm{mW}^{1/2}$$

and the value of λ varies from approximately is 2.4 to 3.2. Whereas in the original paper [40] the parameters of Gaussian pulses at the end of the fiber vary in amplitude

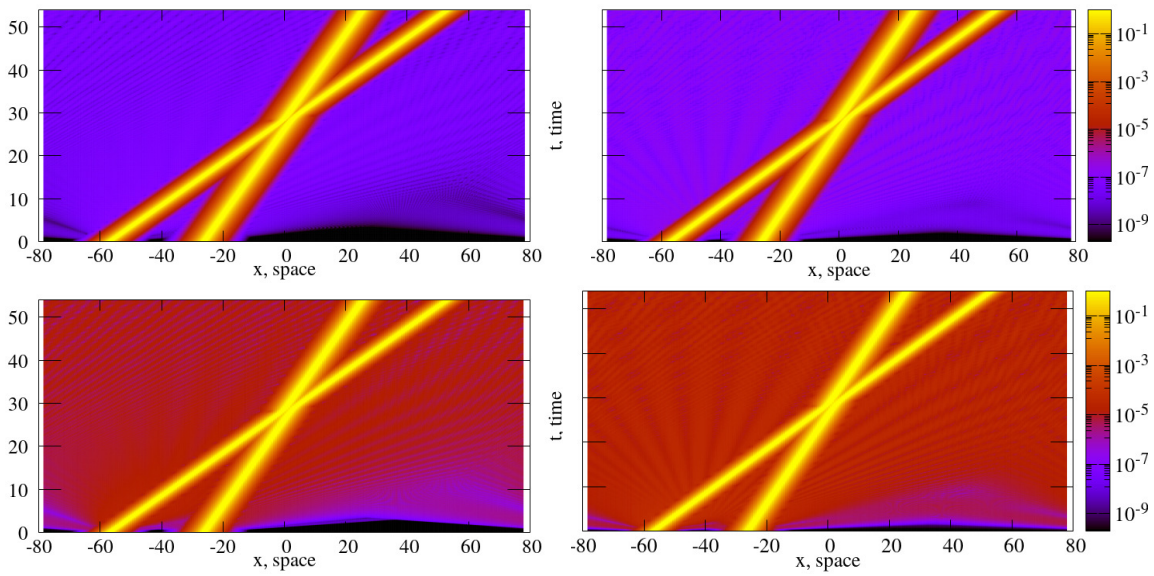

Figure 5.11: (Collision with pursuing soliton) (Top) Numerical solution for HIM (left) and SS2 (right) methods on a fully resolved grid with $N = 4096$ points. (Bottom) Numerical solution for HIM (left) and SS2 (right) methods on an underresolved grid with $N = 1024$ points.

from approximately $1.0 - 2.2\,\mathrm{mW}^{1/2}$ and have characteristic widths $10 - 20\,\mathrm{ps}$.

The nonlinear time is given by $t_{NL} = \frac{\pi}{|\Phi|^2} = \frac{\pi}{2|\lambda|} \approx 0.5$ which in physical units corresponds to $z_{NL} = t_{NL} l \approx 377$ km. If a transatlantic fiber is considered, this amounts to approximately $26 t_{NL}$. We will illustrate the performance of HIM and SS2, on a time scale of $400 t_{NL} \approx 200$ which is still physically relevant.

The solution is computed on a grid of $N = 4096$ points (which corresponds to fully resolved spectrum of the solution) with $L = 25\pi$. The fixed point iterations tolerance is $\varepsilon = 10^{-12}$ for the HIM method. The time step for the split step method is chosen to be $\Delta t_{SS2} = \frac{0.8\Delta x^2}{\pi}$. During simulation time $t = 200$ the numerical solitons interact two times.

In this simulation the results are presented in Figure 5.14, we take $\Delta t_{HIM} = 64\Delta t_{SS2}$, and due to the larger time step the HIM computation time is approximately

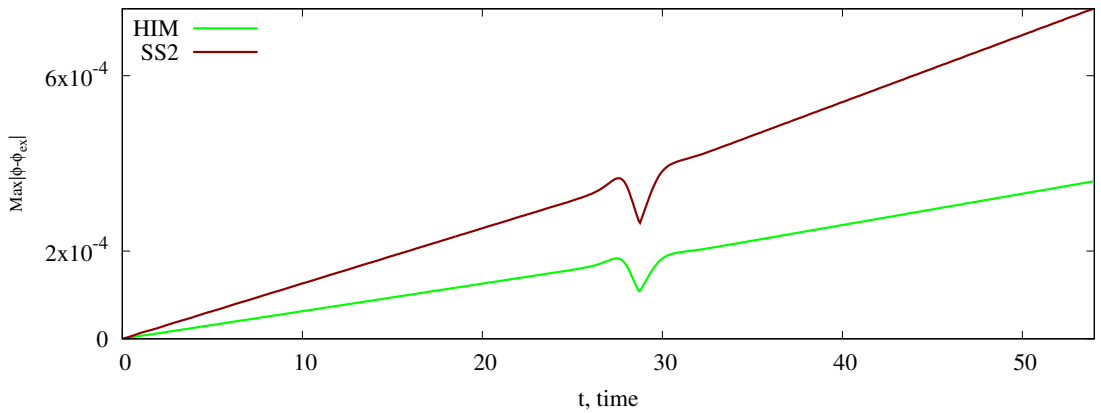

Figure 5.12: (Collision with pursuing soliton on a fully resolved grid) Error in the solution vs time for SS2(red) and HIM(green) methods in the simulation with one soliton pursuing the other. The time of collision is approximately $t = 28$. We observe that the slope, m of the straight line of error vs time changes at the collision for both methods. In SS2 it changes from $m = 1.26 \times 10^{-5}$ to $m = 1.5 \times 10^{-6}$, and in HIM the slope changes from $m = 6.3 \times 10^{-6}$ to $m = 7.12 \times 10^{-6}$.

5.76 times faster. It takes 27.15 seconds for HIM, and 156.45 seconds for SS2 to complete the computation on Intel Core I7-6700HQ CPU with frequency 2.6 GHz and 8 GB RAM in Matlab on a single thread.

The amplitude of radiation in the tails of solitons is about 10^{-7} for SS2, and 10^{-4} for HIM while the time step for HIM is 64 times larger than for SS2. This time step allows HIM to accurately depict the positions of the interacting solitons: at the final time the discrepancy in the location of stationary solitons is less than Δx. Moreover, if the time step for HIM is increased to $128\Delta t_{SS2}$ then the discrepancy in the location is still below $2\Delta x$ and CPU time is 21.30 seconds on a single thread (7.35 times faster than SS2). We note that the amplitude of radiation in the tails of the solitons scales as Δt^2 for both methods. In exact arithmetic and infinitely small Δt the magnitude of the solution in these regions is exponentially small.

In Figure 5.15, we illustrate the conservation of integrals of motion by showing

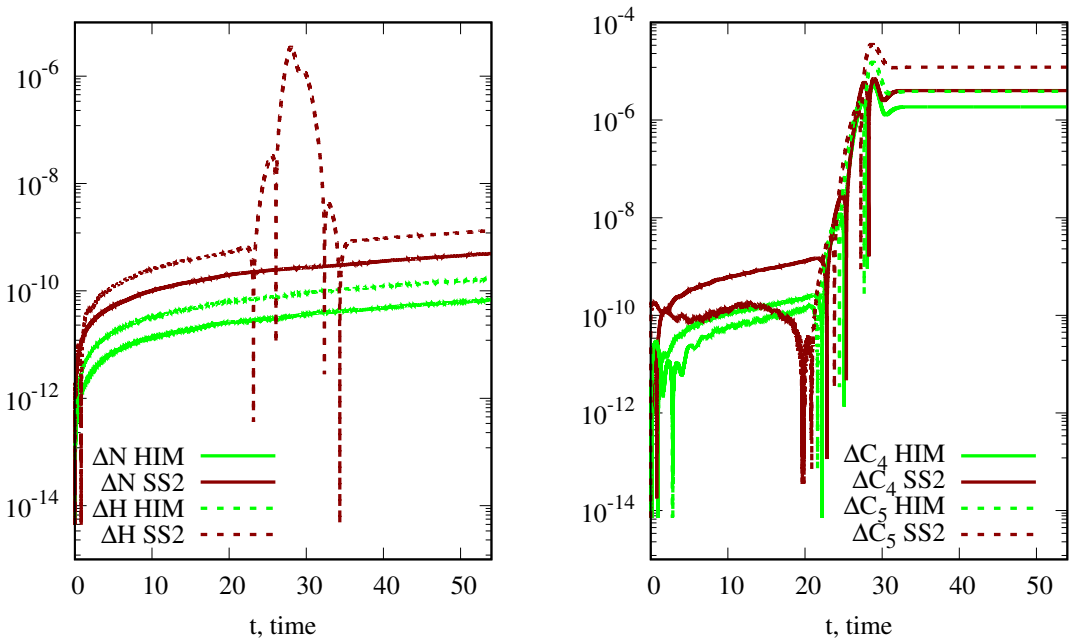

Figure 5.13: (Collision with pursuing soliton on a fully resolved grid) The error in conserved quantities (left) $\Delta\mathcal{N}$ (solid), $\Delta\mathcal{H}$ (dotted), and (right) $\Delta\mathcal{C}_4$ (solid), and $\Delta\mathcal{C}_5$ (dotted) as a function of time over the course of the simulation with HIM (green) and SS2 (red). Note that SS2 demonstrates a strong peak in error in $\mathcal{H}$ at the time of soliton interaction. After the interaction time the $\mathcal{C}_4$, and the $\mathcal{C}_5$ exhibit large error with both SS2 and HIM.

the difference between the Hamiltonian, the number of particles, and the integrals C_4 and C_5 at time t and their values at the initial time. We note that the number of particles varies no more than 10^{-7} for HIM, and less than 10^{-8} for SS2. The value of the Hamiltonian varies no larger than 10^{-7} for HIM, however for SS2 it varies significantly at the time of soliton interaction. We note however, that the accuracy of the actual solution is not representative of these number, and the pointwise error of the numerical solution can be much larger. The integral C_4 is equal to zero in this example, and is not presented in the figure, but the integral C_5 is not zero. It experiences jumps at the time of soliton interactions, and is conserved up to 10^{-2} in the HIM method due to the much larger time step, $\Delta t_{HIM} = 64\Delta t_{SS2}$.

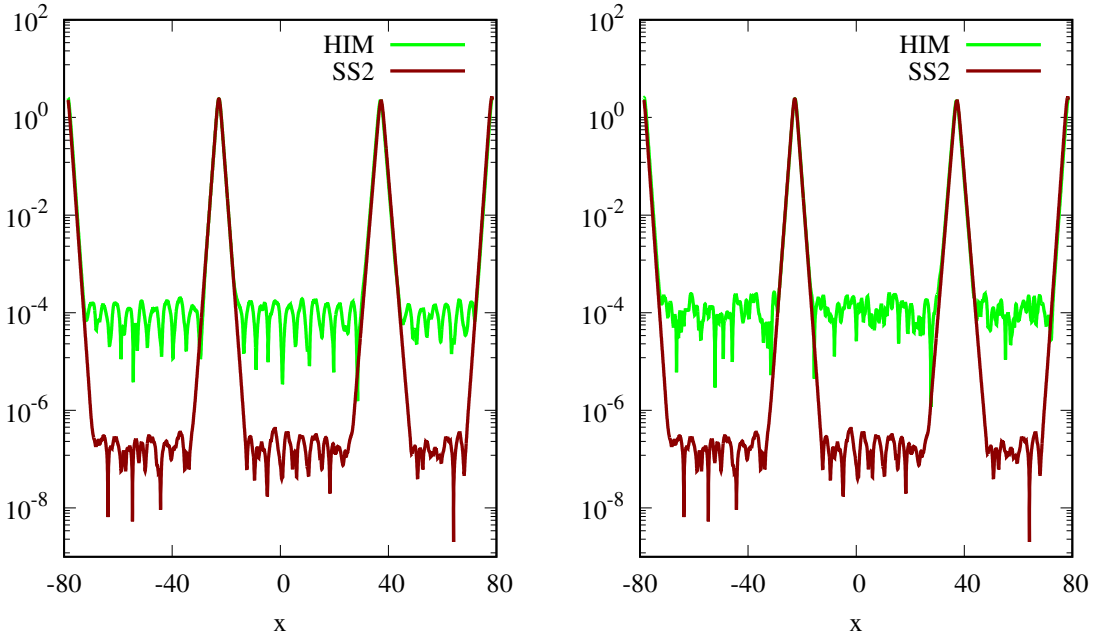

Figure 5.14: (Left) Soliton solution for SS2 (red) with $\Delta t_{SS2} = \frac{0.8\Delta x^2}{\pi}$ and HIM (green) $\Delta t_{HIM} = 64\Delta t_{SS2}$. (Right) Soliton solution for SS2 (red) with $\Delta t_{SS2} = \frac{0.8\Delta x^2}{\pi}$ and HIM (green) $\Delta t_{HIM} = 128\Delta t_{SS2}$.

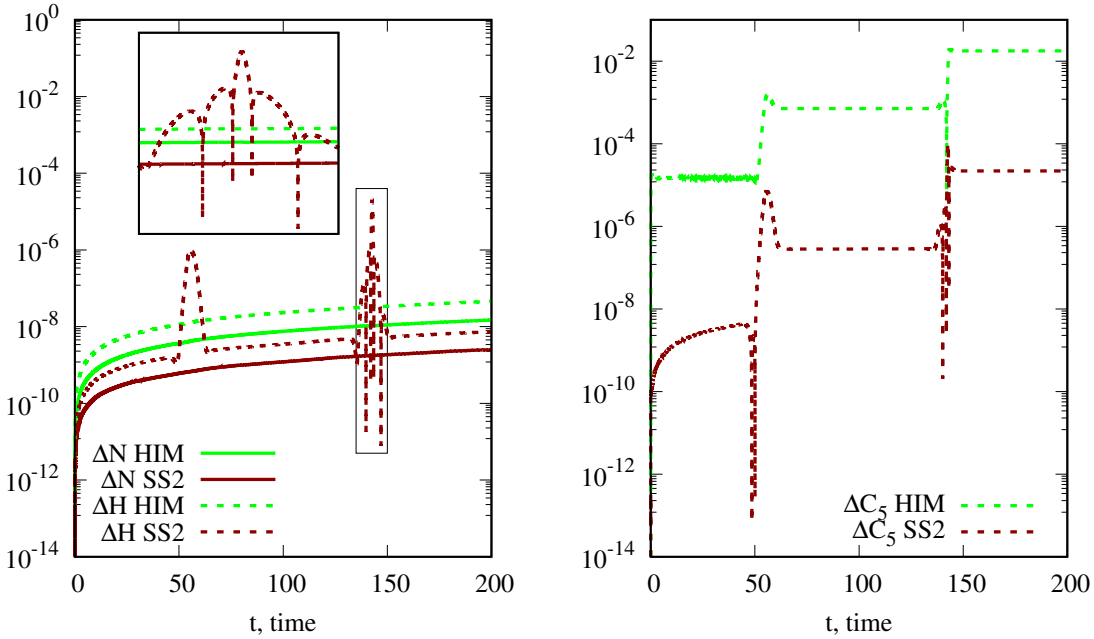

Figure 5.15: (Left) Error in number of particles, ΔN, and Hamiltonian, ΔH for SS2 (red) with $\Delta t_{SS2} = \frac{0.8\Delta x^2}{\pi}$ and HIM (green) with $\Delta t_{HIM} = 64\Delta t_{SS2}$. (Right) Error ΔC_5 for SS2 (red) with $\Delta t_{SS2} = \frac{0.8\Delta x^2}{\pi}$ and HIM (green) with $\Delta t_{HIM} = 128\Delta t_{SS2}$.

Chapter 6

Multi Soliton and Breather Type Solutions

6.1 Initial Condition in the Form of $A\,\mathrm{sech}$

In the set of simulations below, we use the function $A\,\mathrm{sech}\,\frac{x}{\sqrt{2}}$ with $A \in \mathbb{N}$ as an initial condition. These types of initial conditions are proposed in the paper of Satsuma and Yajima [83]. The case $A = 1$ corresponds to one stationary soliton solution (1.5).

We investigate the condition $A = 2$. For this case, the solution of NLSE has the form [83],

$$\Phi(x,t) = 4e^{\frac{-it}{2}} \frac{\cosh\left(\frac{3x}{\sqrt{2}}\right) + 3e^{-4it}\cosh\left(\frac{x}{\sqrt{2}}\right)}{\cosh\left(\frac{4x}{\sqrt{2}}\right) + 4\cosh\left(\frac{2x}{\sqrt{2}}\right) + 3\cos(4t)}. \tag{6.1}$$

This solution is periodic in time with period $t_p = 4\pi$. The equation (6.1) reduces to $\Phi(x,0) = 2\,\mathrm{sech}(\frac{\mathrm{x}}{\sqrt{2}})$ when $t = 0$. We use it as the initial condition.

The simulation is performed on $N = 2048$ grid points and interval $[-L, L]$ with $L = 12\pi$. The time of simulation is $T = 40\pi = 10t_p$, and time step for both methods

is $\Delta t = \frac{0.8}{\pi}\Delta x^2$. The tolerance for HIM iterations is chosen to be $\epsilon = 10^{-13}$.

In Figure 6.1, we plot the $\mathcal{L}_\infty$ norm of the error in the solution (left panel) and maximum of the absolute value of the solution (right panel). The $\mathcal{L}_\infty$ error in the solutions grows with time for both methods. The error is smaller by about one order of magnitude in HIM compared to SS2. The maximum of absolute value of the solution has 10 repetitions in both methods, and this corresponds to the behaviour of the exact solution. The absolute value of the solution is about 2 orders less accurate in SS2 compared to HIM.

We show the absolute value of the difference between values of the integrals of motion at time $t = 0$ and all subsequent times, in the Figure 6.2. Both methods conserve $\mathcal{N}$ equally well. The Hamiltonian is conserved by HIM up to 10^{-9} and by SS2 up to 10^{-4}. There are spikes in $\Delta\mathcal{H}$ from $5 \cdot 10^{-9}$ up to 10^{-4} in the SS2 method. The constant of motion C_4 is preserved up to 10^{-12} by HIM and 10^{-10} by SS2. HIM conserves $\mathcal{C}_5$ up to 10^{-8} whereas for SS2 there are spikes in $\Delta\mathcal{C}_5$ from 10^{-8} up to 10^{-4}.

6.2 Kuznetsov-Ma Soliton Solution

Kuznetsov-Ma soliton solution (Kuznetsov [84], Ma [85], Kibler *et al* [86]) of NLSE has the form,

$$\Phi(x,t) = e^{it}\left[1 + \frac{2(1-2a)\cosh(bt) + ib\sinh(bt)}{\sqrt{2a}\cos(wx) - \cosh(bt)}\right] \tag{6.2}$$

where $b = \sqrt{8a(1-2a)}$, $w = 2\sqrt{1-2a}$. It is a periodic function of time with period,

$$t_p = \frac{2\pi}{\sqrt{8a(2a-1)}}. \tag{6.3}$$

The expression (6.2) (taken from Kibler *et al* [86]) represents the Kuznetsov-Ma soliton solution when the parameter $a > \frac{1}{2}$.

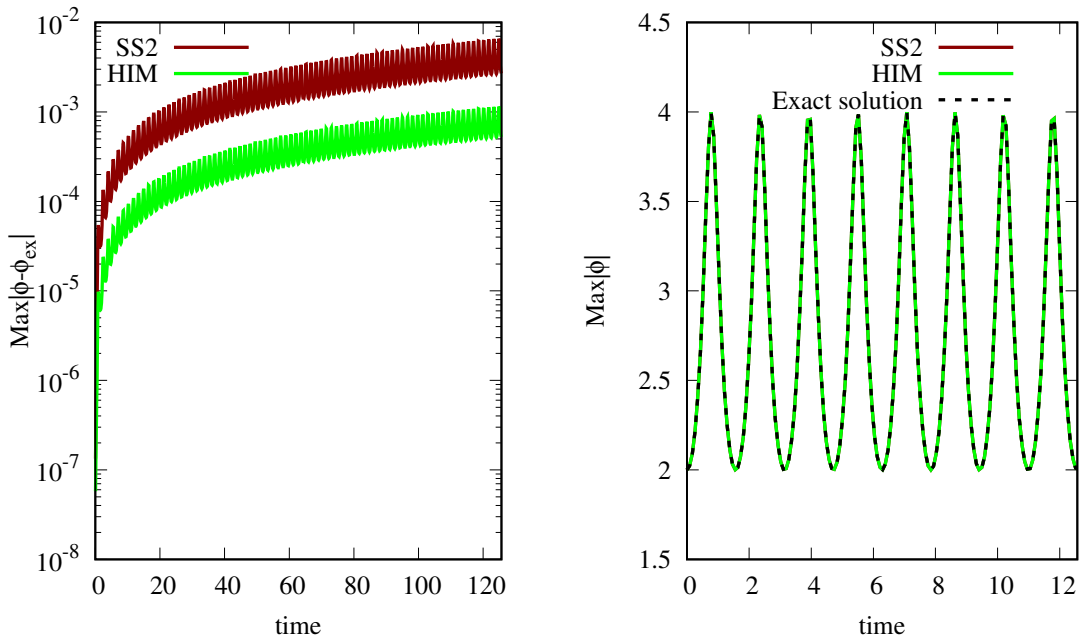

Figure 6.1: (Simulation of initial condition $2\,\mathrm{sech}\,\frac{x}{\sqrt{2}}$ on a fully resolved grid) (Left) The maximum absolute error of the solution as a function of time. The HIM method (green) is about 1 order more accurate than SS2 method (red). (Right) Maximum of the absolute values of solution. Exact solution (black dotted line) oscillates with period (6.2).

We study the case $a = 1$. Parameters of the numerical simulation that we use are $N = 1024$ grid points and box size $[-L, L]$ with $L = 12\pi$. The evolution time is chosen to be 10 time periods of the solution $T = 7\frac{\pi}{\sqrt{2}}$, and the time step is $\Delta t = \frac{0.8}{\pi}\Delta x^2$ for both methods. The tolerance for HIM iterations is chosen to be $\epsilon = 10^{-13}$.

In the Figure 6.3, we plot the $\mathcal{L}_\infty$ error in the solutions (left panel) and maximum of absolute value of the solution (right panel) as functions of time. The error in the solution grows with time, and it is larger in SS2 compared to HIM. We see that the SS2 method loses accuracy in the solution at earlier times (approximately $t \approx 13$) than HIM (approximately $t \approx 15$). If we consider the transatlantic fiber, then the final time of computations needs to be approximately $t \approx 13$, and HIM produces

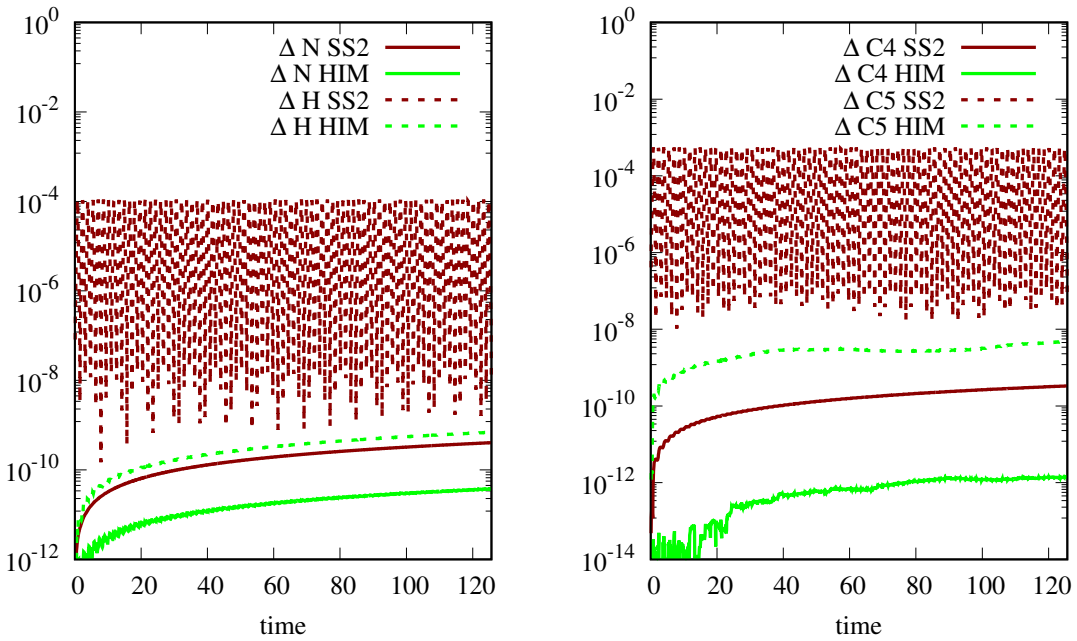

Figure 6.2: (Simulation of initial condition $2\,\mathrm{sech}\,\frac{x}{\sqrt{2}}$ on a fully resolved grid) (Left) The error in integral quantities, $\mathcal{N}$ (solid), and $\mathcal{H}$ (dotted) is about seven orders of magnitude smaller than the error in the solution. (Right) The error in integral quantities, $\mathcal{C}_4$ (solid), and $\mathcal{C}_5$ (dotted). The errors in $\mathcal{H}$ and $\mathcal{C}_5$ are represented by dark red dotted lines for SS2. We omit the details of these curves, but we see that they vary from about 10^{-9} to 10^{-4} for Hamiltonian and about 10^{-8} to 10^{-4} for $\mathcal{C}_5$.

more accurate results up to this time.

In the Figure 6.4, we show the absolute error in conserved quantities $\mathcal{N}$, $\mathcal{H}$ (left panel) and $\mathcal{C}_4$, $\mathcal{C}_5$ (right panel). Both methods conserve the number of particles, $\mathcal{N}$. The accuracy in the Hamiltonian, $\mathcal{H}$, is about 6 orders of magnitude different between SS2 and HIM. Similarly,the difference between SS2 and HIM in $\Delta\mathcal{C}_5$ is about 6 orders of magnitude at early times but grows to 2 orders of magnitude at the end of the simulation. The integral $\mathcal{C}_4 = 0$ and is conserved by both methods well.

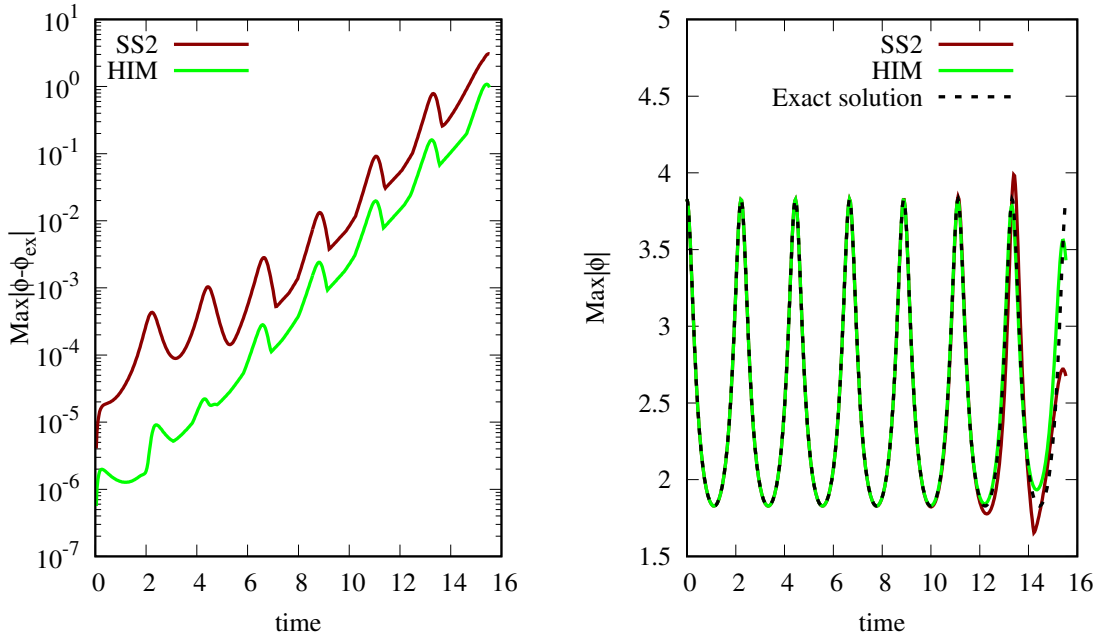

Figure 6.3: (Kuznetsov-Ma soliton solution on a fully resolved grid) SS2 starts to noticeably deviate at about time 12 and HIM at approximately time 14 (Left) The maximum absolute error of the solution as a function of time. The HIM method (green) is about 1 order more accurate than SS2 method (red).
(Right) Maximum of the absolute values of solution. Exact solution (black dotted line) oscillates with period (6.2).

6.3 Akhmediev Breather

Akhmediev breather is the solution of NLSE that is periodic in space and localized in time. The formula (6.2) describes the Akhmediev breather solution when the parameter $a < \frac{1}{2}$.

We take $a = \frac{1}{4}$ and run simulations on the interval $[-L, L]$ with $L = 2\pi$ and $N = 128$ grid points. The tolerance for HIM iterations is chosen to be $\epsilon = 10^{-13}$. The time step for both of methods is $\Delta t = \frac{0.8}{\pi}\Delta x^2$.

The final time of the simulation is taken to be $t = 100$. We zoom into the time interval $t \in [0, 30]$ in the Figure 6.5. We show the $\mathcal{L}_\infty$ error in the solution (left panel)

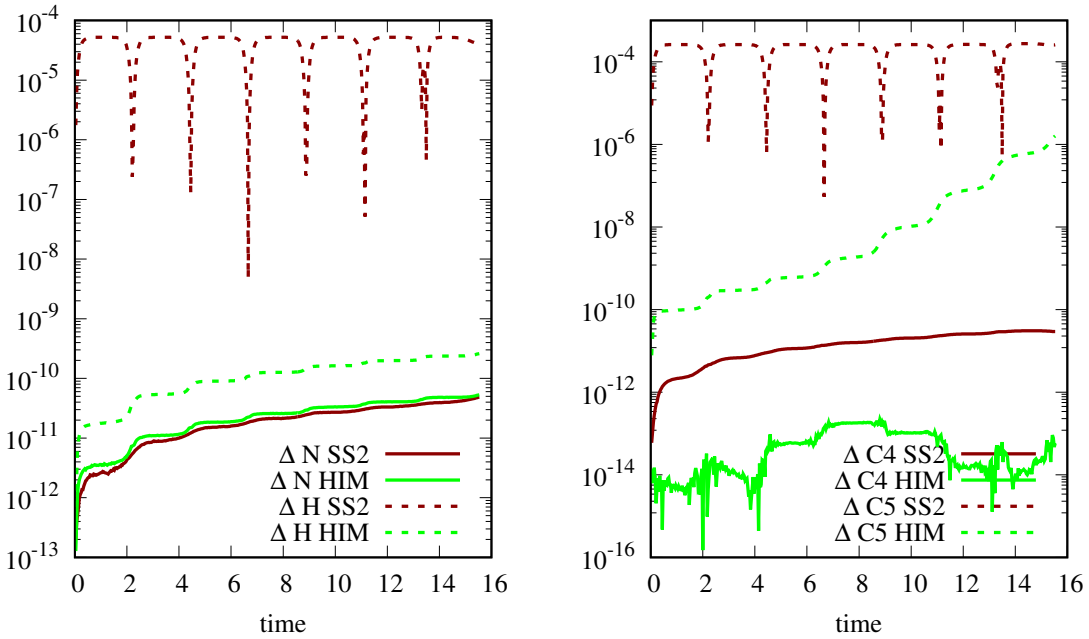

Figure 6.4: (Kuznetsov-Ma soliton solution on a fully resolved grid) (Left) The error in integral quantities, $\mathcal{N}$ (solid), and $\mathcal{H}$ (dotted) is about seven orders of magnitude smaller than the error in the solution. (Right) The error in integral quantities, $\mathcal{C}_4$ (solid), and $\mathcal{C}_5$ (dotted).

and maximum absolute value of the solution (right panel) as functions of time. SS2 stops producing correct solution at about time $t \approx 15$ while the error in the solution is approximately 10^{-6} for HIM at that time. The error in the HIM starts to grow from about time $t \approx 17$ and reaches the same order as SS2 at approximately time $t \approx 30$. On the right panel, we see that the maximum of absolute value of the exact solution approaches a constant while solutions from SS2 and HIM have repetitive behaviour in time. Initially numerical solutions approach the same constant value as the exact solution, but as time increases they start to diverge from it.

For the simulation time $t = 100$, there are oscillations in numerical solutions that appear and disappear in time that can be seen in the Figure 6.6. If we look at the $\mathcal{L}_\infty$ error in the solution (left panel), we see that the error in the solution decreases as the

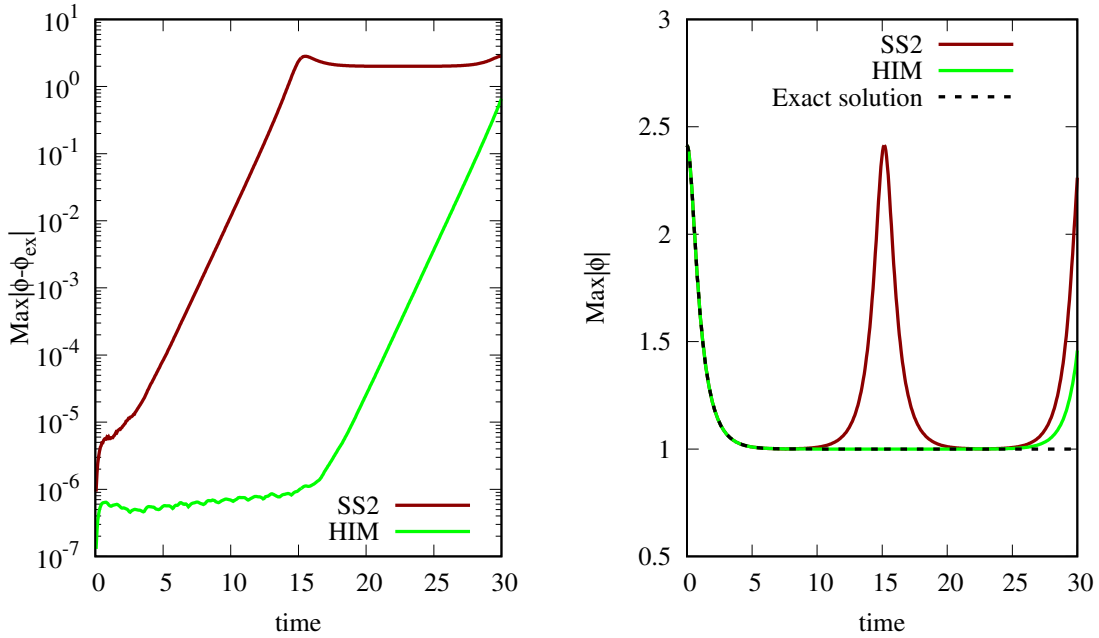

Figure 6.5: (Akhmediev soliton solution on a fully resolved grid until time $t = 30$) (Left) The maximum absolute error of the solution as a function of time. The error in the SS2 method (red) grows starting from small values of time, and in HIM (green) stays at about 10^{-6} until about time 18. (Right) Maximum of absolute value of solution as a function of time. Exact solution (black dotted line) approaches a constant as time goes to infinity. SS2 (red) and HIM (green) have oscilations during simulations that deviate from the exact solution with repietition.

solution approaches the exact solution during the oscillations. The same behaviour is seen in the maximum absolute value of the solution as a function of time (right panel).

In the Figure 6.7, we show the absolute error in constants of motion $\mathcal{N}$, $\mathcal{H}$ (left panel) and $\mathcal{C}_4$, $\mathcal{C}_5$ (right panel). SS2 conserves $\mathcal{N}$ and $\mathcal{C}_4$ with good accuracy. It conserves $\mathcal{H}$ and $\mathcal{C}_5$ up to 10^{-5}, and the absolute error in both of these quantities oscillates. HIM conserves all 4 constant of motion $\mathcal{N}$, $\mathcal{H}$, $\mathcal{C}_4$, $\mathcal{C}_5$ up to 10^{-11}–10^{-12}.

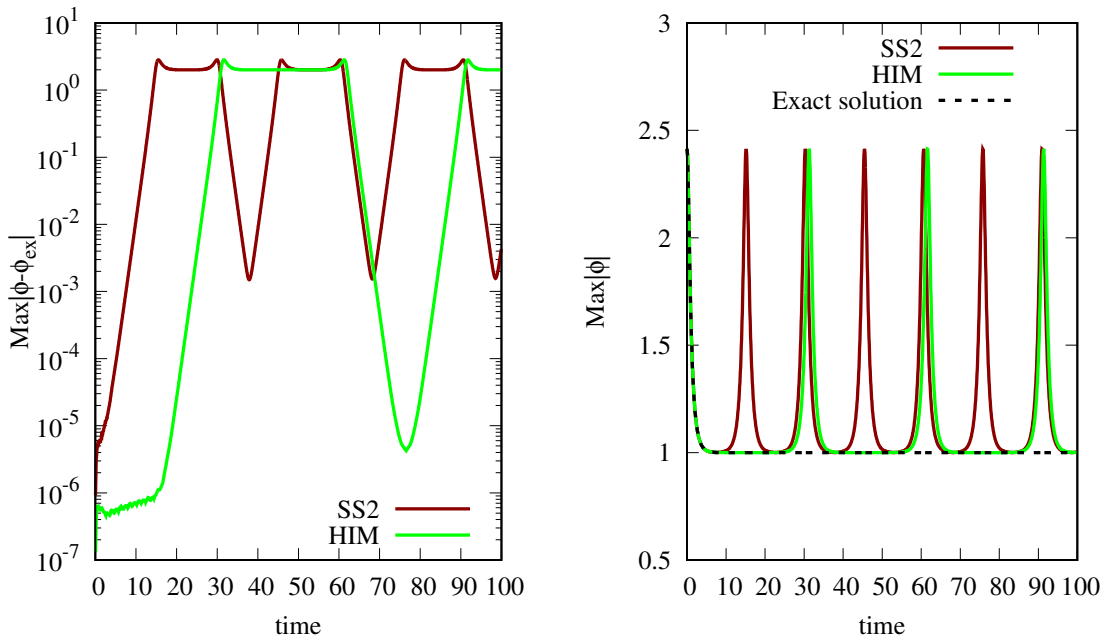

Figure 6.6: (Akhmediev soliton solution on a fully resolved grid until time $t = 100$) (Left) The maximum absolute error of the solution as a function of time. (Right) Maximum of absolute value of solution as a function of time. Exact solution (black dotted line) approaches a constant as time goes to infinity. SS2 (red) and HIM (green) have a couple of oscillations in the solution.

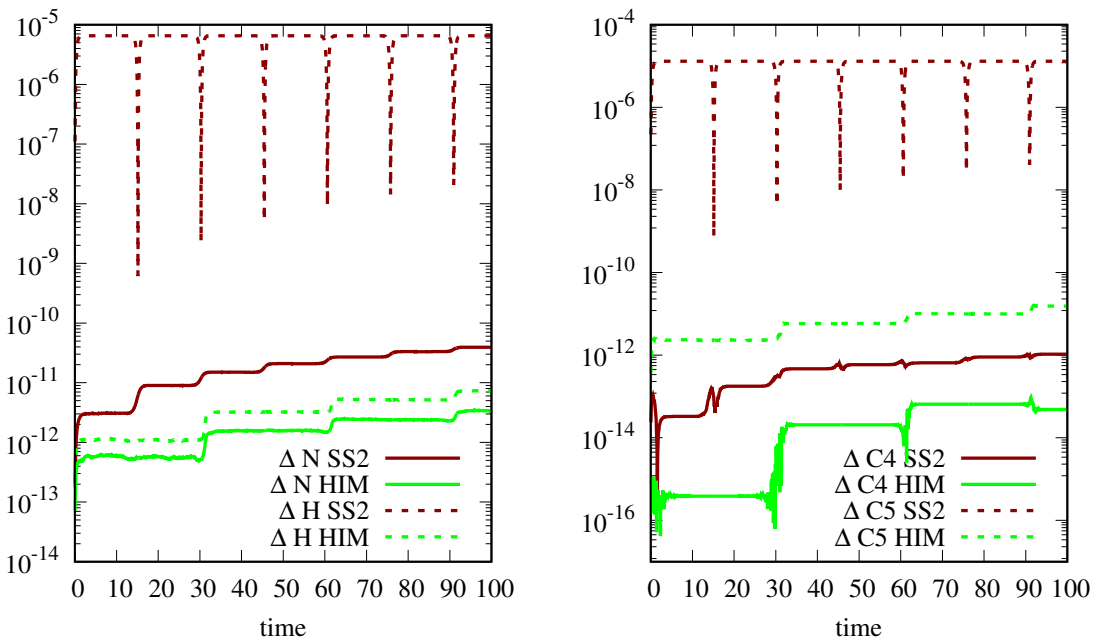

Figure 6.7: (Akhmediev soliton solution on a fully resolved grid) (Left) The error in integral quantities, $\Delta\mathcal{N}$ (solid), and $\Delta\mathcal{H}$ (dotted) as a function of time. The error in $\mathcal{H}$ is about 5 orders of magnitude is smaller in HIM compared to SS2, and equivalent in both methods for $\mathcal{N}$. (Right) The conserved quantities quantities $\Delta\mathcal{C}_4$ (solid), and $\Delta\mathcal{C}_5$ (dotted) as a function of time. The error in $\mathcal{C}_\bigtriangledown$ is several orders of magnitude smaller in HIM. The error in $\mathcal{C}_\bigtriangleup$ is comparable in both methods.

Chapter 7

Conclusion of Part II

We performed a detailed comparison of two algorithms for simulation of NLSE: Hamiltonian integration proposed in Dyachenko *et al* [51] and the widely used second order split-step method. In all cases the Hamiltonian integration demonstrates better conservation of the Hamiltonian at the time of soliton collision. The other constants of motion N, C_4 and C_5 are conserved better by HIM when the time step is the same or slightly larger than the one used for the split-step method. However, if the time step is increased several orders of magnitude, the accuracy of conservation of integrals of motion in HIM may be lower. On the other hand, the pointwise error between the numerical solution and analytic formula is significantly larger than the variation of conserved quantities, which means that integrals of motion reflect the quality of the solution rather poorly. In experiments we observe this error to be about 10^{-2}-10^{-3} in the maximum norm. For this reason a criterion of convergence of fixed point iterations by the number of particles or Hamiltonian, that was used in the original paper [51], is suboptimal, and it is more accurate to control convergence of the residual (2.11) as proposed in this work.

However, if the primary goal is to accurately portray the interaction of solitons

over the physically relevant time, such as propagation distance in an optical fiber, it is significantly more advantageous to use the HIM method with a large time step rather than the SS2 method which requires smaller time steps to satisfy the stability criterion. Violation of the stability criterion for SS2 results in complete disintegration of the solution for long time simulations (Lakoba [87]). In our simulations for 400 nonlinear times, the time step for HIM is about 64–128 times larger than the instability criterion for SS2. However, in a simulation for significantly longer time it may lead to accumulation of errors in positioning of the solitons (jitter). For example if one simulates for 4000 nonlinear times, the inaccuracy in the soliton position is about $10\Delta x$, and in order to keep the soliton positioning accuracy at Δx one would need to decrease the time step for HIM which results in smaller gains in computation time.

The accurate portrayal of soliton interactions is crucial for the simulation of interactions in a soliton gas Zakharov [88], Agafontsev and Zakharov [89], Turitsyn *et al* [90, 91], or the fast developing field of integrable turbulence (Zakharov and Ostrovsky [37]). Both SS2 and HIM approaches are well suited for this. At the same time, the split-step method is simpler to implement and is more efficient memory-wise. In addition, the split-step method is explicit, whereas HIM is an implicit method.

As a summary, the Hamiltonian integration method is recommended for simulations requiring accurate description of soliton-soliton interactions or other subtle nonlinear phenomena in Hamiltonian systems especially when computation time is of the essence. Relevance of fast computational algorithms for optical problems can be illustrated by the papers Lushnikov [40] and Korotkevich and Lushnikov [92] where a massively parallel algorithm for a modification of NLSE was proposed and implemented. For multidimensional turbulence (for instance Falkovich and Vladimirova [93]), the split-step scheme of order two, and higher order split step methods (Yoshida [58],

Chung and Lushnikov [94]) can be an approach of choice.

Appendices

Appendix A

Free Surface Hydrodynamics, Stokes Waves

In this Appendix we give an outline of steps to derive the dynamical equations (1.5)–(1.6) that were omitted in Dyachenko *et al* [21] and described in detail (for the periodic boundary conditions) in the paper by Dyachenko *et al* [18].

A.1 Derivation of Implicit Equations of Motion

In the work [9], Zakharov showed that potential flow of an ideal fluid with a free surface is governed by the canonical Hamiltonian system for surface elevation and velocity potential at the surface:

$$\frac{\partial \eta}{\partial t} = \frac{\delta \mathcal{H}}{\delta \psi}, \quad \frac{\partial \psi}{\partial t} = -\frac{\delta \mathcal{H}}{\delta \eta}. \tag{A.1}$$

A.1.1 Change of Variables in Lagrangian

We outline steps to derive the implicit equations at a free surface in conformal variables. From equations (A.1), we consider extremum of the action:

$$\mathcal{S} = \int_{t_1}^{t_2} L dt. \tag{A.2}$$

with the constrained Lagrangian:

$$\mathcal{L} = \int_{-\pi}^{\pi} \psi \frac{\partial \eta}{\partial t} dx - \mathcal{H} + \int_{-\pi}^{\pi} (y - y_0 - \hat{H}\tilde{x}) f du. \tag{A.3}$$

We see that the first integral is in the x variable and should be converted into u. To do that, we consider the transformation $(x,t) \to (u,\tau)$ where $\tau = t$ and as described in Dyachenko *et al* [18] it can be shown that,

$$\frac{\partial \eta}{\partial t} = y_\tau - y_u \frac{x_\tau}{x_u}. \tag{A.4}$$

So, we use the change of variables $dxdt = dud\tau x_u$ and the expression (A.4) to find that:

$$\int\int \psi \frac{\partial \eta}{\partial t} dxdt = \int\int \psi \left(y_\tau - y_u \frac{x_\tau}{x_u} \right) x_u du d\tau = \int\int \psi (y_\tau x_u - y_u x_\tau) du d\tau. \tag{A.5}$$

So by substituting the expression (A.5) together with $\tau = t$ into (A.3) we get that the constrained Lagrangian in the u variable has the form,

$$\mathcal{L} = \int_{-\pi}^{\pi} \psi (y_t x_u - y_u x_t) du + \frac{1}{2} \int_{-\pi}^{\pi} \psi \hat{H} \psi_u du - \frac{g}{2} \int_{-\pi}^{\pi} y^2 x_u du + \int_{-\pi}^{\pi} (y - y_0 - \hat{H}\tilde{x}) f du, \tag{A.6}$$

where f is the Lagrange multiplier.

A.1.2 Variations of Action

We use the Hamilton's least action principle to get the implicit equations (1.5)–(1.6). We take the variational derivative of $\mathcal{S}$ with respect to ψ and the condition $\delta\mathcal{S}/\delta\psi = 0$ to get,

$$\frac{\delta\mathcal{S}}{\delta\psi} = y_t x_u - y_u x_t - \frac{\delta\mathcal{H}}{\delta\psi} = 0 \tag{A.7}$$

where $\frac{\delta\mathcal{H}}{\delta\psi} = \frac{\delta K}{\delta\psi}$ because only the kinetic term of the Hamiltonian depends on $\delta\psi$. Equation (A.7) transforms into the expression (1.5),

$$y_t x_u - y_u x_t = -\hat{H}\psi_u. \tag{A.8}$$

Now, we take the variational derivatives of $\mathcal{S}$ with respect to y and x and use conditions $\delta\mathcal{S}/\delta x = 0$, $\delta\mathcal{S}/\delta y = 0$ to get the following expressions:

$$\frac{\delta\mathcal{S}}{\delta y} = -\partial_t(\psi x_u) + \partial_u(\psi x_t) - g y x_u + f = 0, \tag{A.9}$$

$$\psi_t x_u - \psi_u x_t + g y x_u = f, \tag{A.10}$$

and

$$\frac{\delta\mathcal{S}}{\delta x} = \partial_t(\psi y_u) - \partial_u(\psi y_t) + \frac{1}{2} g \partial_u(y^2) + \hat{H} = 0, \tag{A.11}$$

$$\psi_t y_u - \psi_u y_t + g y y_u = -\hat{H} f. \tag{A.12}$$

From equations (A.10)–(A.12), we get that $f = \hat{H}\left(\psi_t y_u - \psi_u y_t\right)$. So, the second implicit equation (1.6) has the form,

$$\psi_t x_u - \psi_u x_t - \hat{H}\left(\psi_t y_u - \psi_u y_t\right) + g\left[y x_u - \hat{H} y y_u\right] = 0 \tag{A.13}$$

Appendix B

Hamiltonian Integration Method for Nonlinear Schrödinger Equation

In this Appendix we provide steps of derivations that we were omitted in the paper Dyachenko *et al* [51].

B.1 Derivation of HIM method for NLSE

We consider the equation (1.1) where $\gamma = 1$ and with the Hamiltonian (1.2). Let $\mathcal{H}^n = \int \left(|\Phi_x^n|^2 - \frac{\gamma}{2}|\Phi^n|^4\right)$ be the discretized in time Hamiltonian at the n-th time step. We consider the change of Hamiltonian after one time step Δt:

$$\Delta\mathcal{H} = \mathcal{H}^{n+1} - \mathcal{H}^n = I_1 + I_2, \tag{B.1}$$

where $I_1 := \int \left(|\Phi_x^{n+1}|^2 - |\Phi_x^n|^2\right) dx$ and $I_2 := \gamma \int \left(\frac{1}{2}|\Phi^n|^4 - \frac{1}{2}|\Phi^{n+1}|^4\right) dx$. We consider I_1 and I_2 separately.

By addition and subtraction to I_1 of the following terms, $\frac{1}{2}\Phi_x^n\bar{\Phi}_x^{n+1}$ and $\frac{1}{2}\Phi_x^{n+1}\bar{\Phi}_x^n$, under the integral sign, combining terms and using integration by parts, one gets:

$$I_1 = -\frac{1}{2}\int \left(\bar{\Phi}_{xx}^{n+1}\Delta\Phi + \Phi_{xx}^n\Delta\bar{\Phi} + \Phi_{xx}^{n+1}\Delta\bar{\Phi} + \bar{\Phi}_{xx}^n\Delta\Phi\right)dx,$$

here we have introduced $\Delta\Phi = \Phi^{n+1} - \Phi^n$.

By addition and subtraction to I_2 of the four following terms, $\frac{\gamma}{2}|\Phi^{n+1}|^2\Phi^n\bar{\Phi}^{n+1}$, $\frac{\gamma}{2}|\Phi^{n+1}|^2\Phi^{n+1}\bar{\Phi}^n$, $\frac{\gamma}{2}|\Phi^n|^2\Phi^{n+1}\bar{\Phi}^n$ and $\frac{\gamma}{2}|\Phi^n|^2\Phi^n\bar{\Phi}^{n+1}$, under the integral sign and combining terms, we arrive at

$$I_2 = -\frac{\gamma}{4}\int \left(\Delta\Phi(\bar{\Phi}^{n+1}+\bar{\Phi}^n)(|\Phi^{n+1}|^2+|\Phi^n|^2)+\Delta\bar{\Phi}(\Phi^{n+1}+\Phi^n)(|\Phi^{n+1}|^2+|\Phi^n|^2)\right)dx.$$

After combining the like terms, we arrive at the formula

$$\Delta\mathcal{H} = \frac{1}{2}\int [\Delta\Phi\left(-\bar{\Phi}_{xx}^{n+1} - \bar{\Phi}_{xx}^n - \frac{\gamma}{2}(\bar{\Phi}^{n+1}+\bar{\Phi}^n)(|\Phi^{n+1}|^2+|\Phi^n|^2)\right) + \Delta\bar{\Phi}\left(-\Phi_{xx}^{n+1} - \Phi_{xx}^n - \frac{\gamma}{2}(\Phi^{n+1}+\Phi^n)(|\Phi^{n+1}|^2+|\Phi^n|^2)\right)]dx. \quad \text{(B.2)}$$

If we divide (B.2) by Δt and require that the first and second expressions in square brackets are equal to $\frac{i\Delta\bar{\Phi}}{\Delta t}$ and $\frac{-i\Delta\Phi}{\Delta t}$ correspondingly, then $\Delta\mathcal{H}$ vanishes. We note that:

$$i\Phi_t = \frac{\delta\mathcal{H}}{\delta\bar{\Phi}}$$
$$i\bar{\Phi}_t = -\frac{\delta\mathcal{H}}{\delta\Phi}.$$

We get the following numerical scheme in time:

$$i\frac{\Phi^{n+1}-\Phi^n}{\Delta t} = -\frac{[\Phi^{n+1}+\Phi^n]_{xx}}{2} - \frac{\gamma(\Phi^{n+1}+\Phi^n)(|\Phi^{n+1}|^2+|\Phi^n|^2)}{4}. \quad \text{(B.3)}$$

B.2 Derivation of the stability condition

In order to solve the equation (1.1) one can use the iteration scheme (2.10):

$$\Phi_k^{n+1,s+1} = \frac{1-\frac{ik^2\Delta t}{2}}{1+\frac{ik^2\Delta t}{2}}\Phi_k^n + \frac{\frac{i\Delta t\gamma}{4}}{1+\frac{ik^2\Delta t}{2}}\hat{F}\left[(|\Phi^{n+1,s}|^2+|\Phi^n|^2)(\Phi^{n+1,s}+\Phi^n)\right]. \quad \text{(B.4)}$$

We consider $\Phi^{n+1,s+1} = \Phi_0^{n+1} + \delta\Phi^{s+1}$ and $\Phi^{n+1,s} = \Phi_0^{n+1} + \delta\Phi^{s}$ where Φ_0^{n+1} is the exact solution at the $(n+1)$-st time step. Let's keep only terms linear in $\delta\Phi^{s+1}$ and neglect terms with small scale perturbations $\delta\Phi^s$:

$$\delta\Phi_k^{s+1} = \frac{\frac{i\Delta t\gamma}{4}}{1+\frac{ik^2\Delta t}{2}}\left[2|\Phi_0^{n+1}|^2 + |\Phi^n|^2 + \Phi^n\bar{\Phi}_0^{n+1}\right]\delta\Phi_k^s + \\ + \frac{\frac{i\Delta t\gamma}{4}}{1+\frac{ik^2\Delta t}{2}}\left[(\Phi_0^{n+1})^2 + \Phi^n\Phi_0^{n+1}\right]\delta\bar{\Phi}_k^s \quad \text{(B.5)}$$

Therefore, we can compose the following system of linear equations:

$$\begin{bmatrix}\delta\Phi_k^{s+1}\\ \delta\bar{\Phi}_k^{s+1}\end{bmatrix} = A\begin{bmatrix}\delta\Phi_k^{s}\\ \delta\bar{\Phi}_k^{s},\end{bmatrix}$$

and

$$A = \begin{pmatrix} c\left[2|\Phi_0^{n+1}|^2 + |\Phi^n|^2 + \Phi^n\bar{\Phi}_0^{n+1}\right] & c\left[(\Phi_0^{n+1})^2 + \Phi^n\Phi_0^{n+1}\right] \\ \bar{c}\left[(\bar{\Phi}_0^{n+1})^2 + \bar{\Phi}^n\bar{\Phi}_0^{n+1}\right] & \bar{c}\left[2|\Phi_0^{n+1}|^2 + |\Phi^n|^2 + \bar{\Phi}^n\Phi_0^{n+1}\right] \end{pmatrix} \quad \text{(B.6)}$$

where $c = \frac{\frac{i\gamma\Delta t}{4}}{1+\frac{ik^2\Delta t}{2}}$ We need the matrix A to be a contracting map. As a result, we require its determinant to be smaller than 1. From $|\det(A)| < 1$, we can get the condition for the convergence of the HIM iterations:

$$\Delta t < \frac{2}{|\gamma|\sqrt{3}\max(|\Phi^n|^2)} \quad \text{(B.7)}$$

References

[1] M. Longuet-Higgins, M. Tanaka, On the crest instabilities of steep surface waves, Journal of Fluid Mechanics 336 (1997) 51–68.

[2] G. G. Stokes, On the theory of oscillatory waves, Transactions of the Cambridge Philosophical Society 8 (1847) 441.

[3] G. G. Stokes, On the theory of oscillatory waves, Mathematical and Physical Papers 1 (1880) 197.

[4] A. I. Nekrasov, On waves of permanent type I, Izv. Ivanovo-Voznesensk. Polite. Inst. 3 (1921) 52–65.

[5] T. Levi-Civita, Détermination rigoureuse des ondes permanentes d'ampleur finie, Mathematische Annalen 93 (1) (1925) 264–314.

[6] G. G. Stokes, Supplement to a paper on the Theory of Oscillatory Waves, Mathematical and Physical Papers 1 (1880) 314.

[7] P. I. Plotnikov, A proof of the Stokes conjecture in the theory of surface waves, Studies in Applied Mathematics 108 (2) (2002) 217–244.

[8] C. J. Amick, L. E. Fraenkel, J. F. Toland, On the Stokes conjecture for the wave of extreme form, Acta Mathematica 148 (1) (1982) 193–214.

[9] V. E. Zakharov, Stability of periodic waves of finite amplitude on the surface of a deep fluid, Journal of Applied Mechanics and Technical Physics 9 (2) (1968) 190–194.

[10] J. H. Michell, XLIV. The highest waves in water, The London, Edinburgh, and Dublin Philosophical Magazine and Journal of Science 36 (222) (1893) 430–437.

[11] M. A. Grant, The singularity at the crest of a finite amplitude progressive Stokes wave, J. Fluid Mech 59 (part 2) (1973) 257–262.

[12] L. W. Schwartz, Computer extension and analytic continuation of Stokes' expansion for gravity waves, Journal of Fluid Mechanics 62 (3) (1974) 553–578.

[13] J. M. Williams, Limiting gravity waves in water of finite depth, Philosophical Transactions of the Royal Society of London. Series A, Mathematical and Physical Sciences 302 (1466) (1981) 139–188.

[14] J. M. Williams, Tables of progressive gravity waves, Boston : Pitman Advanced Pub. Program, 1985.

[15] D. V. Maklakov, Almost-highest gravity waves on water of finite depth, European Journal of Applied Mathematics 13 (1) (2002) 67.

[16] I. S. Gandzha, V. P. Lukomsky, On water waves with a corner at the crest, Proceedings of the Royal Society A: Mathematical, Physical and Engineering Sciences 463 (2082) (2007) 1597–1614.

[17] S. A. Dyachenko, P. M. Lushnikov, A. O. Korotkevich, Complex singularity of a Stokes wave, JETP letters 98 (11) (2014) 675–679.

[18] S. A. Dyachenko, P. M. Lushnikov, A. O. Korotkevich, Branch cuts of Stokes wave on deep water. Part I: numerical solution and Padé approximation, Studies in Applied Mathematics 137 (4) (2016) 419–472.

[19] P. M. Lushnikov, S. A. Dyachenko, D. A. Silantyev, New conformal mapping for adaptive resolving of the complex singularities of Stokes wave, Proceedings of the Royal Society A: Mathematical, Physical and Engineering Sciences 473 (2202) (2017) 20170198.

[20] L. V. Ovsyannikov, Dynamika sploshnoi sredy, Lavrentiev Institute of Hydrodynamics, Sib. Branch Acad. Sci. USSR 15 (1973) 104.

[21] A. I. Dyachenko, E. A. Kuznetsov, M. Spector, V. E. Zakharov, Analytical description of the free surface dynamics of an ideal fluid (canonical formalism and conformal mapping), Physics Letters A 221 (1-2) (1996) 73–79.

[22] A. I. Dyachenko, On the dynamics of an ideal fluid with a free surface, in: Doklady Mathematics, Vol. 63, Pleiades Publishing, Ltd., 2001, pp. 115–117.

[23] T. B. Benjamin, Instability of periodic wavetrains in nonlinear dispersive systems, Proceedings of the Royal Society of London. Series A. Mathematical and Physical Sciences 299 (1456) (1967) 59–76.

[24] T. B. Benjamin, J. E. Feir, The disintegration of wave trains on deep water, J. Fluid mech 27 (3) (1967) 417–430.

[25] M. J. Lighthill, Contributions to the theory of waves in non-linear dispersive systems, IMA Journal of Applied Mathematics 1 (3) (1965) 269–306.

[26] G. B. Whitham, Non-linear dispersion of water waves, Journal of Fluid Mechanics 27 (2) (1967) 399–412.

[27] M. S. Longuet-Higgins, The instabilities of gravity waves of finite amplitude in deep water I. Superharmonics, Proceedings of the Royal Society of London. A. Mathematical and Physical Sciences 360 (1703) (1978) 471–488.

[28] M. Tanaka, The stability of steep gravity waves, Journal of the physical society of Japan 52 (9) (1983) 3047–3055.

[29] H. C. Longuet-Higgins, Integral properties of periodic gravity waves of finite amplitude, Proceedings of the Royal Society of London. A. Mathematical and Physical Sciences 342 (1629) (1975) 157–174.

[30] M. S. Longuet-Higgins, M. J. H. Fox, Theory of the almost–highest wave. Part 2. Matching and analytic extension, J. Fluid Mech. 85 (1978) 769–786.

[31] M. S. Longuet-Higgins, D. G. Dommermuth, Crest instabilities of gravity waves. Part 3. Nonlinear development and breaking, Journal of Fluid Mechanics 336 (1997) 33–50.

[32] M. S. Longuet-Higgins, E. D. Cokelet, The deformation of steep surface waves on water II. Growth of normal-mode instabilities, Proceedings of the Royal Society of London. A. Mathematical and Physical Sciences 364 (1716) (1978) 1–28.

[33] T. J. Bridges, Superharmonic instability, homoclinic torus bifurcation and water-wave breaking, Journal of Fluid Mechanics 505 (2004) 153–162.

[34] V. E. Zakharov, A. I. Dyachenko, A. O. Prokofiev, Freak waves as nonlinear stage of Stokes wave modulation instability, European Journal of Mechanics-B/Fluids 25 (5) (2006) 677–692.

[35] C. Sulem, P. Sulem, The Nonlinear Schrödinger Equation: Self-Focusing and Wave Collapse, Applied Mathematical Sciences, Springer New York, 1999.
URL `https://books.google.com/books?id=uTxYaEztjzgC`

[36] L. D. Landau, E. M. Lifshitz, Course of theoretical physics, Vol. 3: Quantum mechanics, Pergamon Press, 1958.

[37] V. E. Zakharov, L. A. Ostrovsky, Modulation instability: The beginning, Physica D: Nonlinear Phenomena 238 (5) (2009) 540–548.

[38] L. Pitaevskii, S. Stringari, Bose-Einstein Condensation, International Series of Monographs on Physics, Oxford University Press, Clarendon Press, 2003.

[39] G. P. Agrawal, Nonlinear fiber optics, Academic press, 2007.

[40] P. M. Lushnikov, Fully parallel algorithm for simulating dispersion-managed wavelength-division-multiplexed optical fiber systems, Optics letters 27 (11) (2002) 939–41.

[41] V. E. Zakharov, Collapse of Langmuir waves, Sov. Phys. JETP 35 (5) (1972) 908–914.

[42] D. A. Silantyev, P. M. Lushnikov, H. A. Rose, Langmuir wave filamentation in the kinetic regime. I. Filamentation instability of Bernstein-Greene-Kruskal modes in multidimensional Vlasov simulations, Phys. of Plasmas 24 (2017) 042104.

[43] K. B. Dysthe, Note on a modification to the nonlinear Schrödinger equation for application to deep water waves, Proceedings of the Royal Society of London. A. Mathematical and Physical Sciences 369 (1736) (1979) 105–114.

[44] A. I. Dyachenko, V. E. Zakharov, Modulation instability of Stokes wave - freak wave, Journal of Experimental and Theoretical Physics Letters 81 (6) (2005) 255–259.

[45] J. Crank, P. Nicolson, A practical method for numerical evaluation of solutions of partial differential equations of the heat-conduction type, Vol. 43 of Mathematical Proceedings of the Cambridge Philosophical Society, Cambridge University Press, 1947.

[46] T. R. Taha, M. I. Ablowitz, Analytical and numerical aspects of certain nonlinear evolution equations. II. Numerical, nonlinear Schrödinger equation, Journal of Computational Physics 55 (2) (1984) 203–230.

[47] I. Greig, J. Morris, A Hopscotch method for the Korteweg–de–Vries equation, Journal of Computational Physics 20 (1) (1976) 64–80.

[48] M. J. Ablowitz, J. F. Ladik, A nonlinear difference scheme and inverse scattering, Studies in Applied Mathematics 55 (3) (1976) 213–229.

[49] M. J. Ablowitz, J. F. Ladik, Nonlinear differential–difference equations and Fourier analysis, Journal of Mathematical Physics 17 (6) (1976) 1011–1018.

[50] R. H. Hardin, F. D. Tappert, Applications of the Split-Step Fourier Method to the Numerical Solution of Nonlinear and Variable Coefficient Wave Equations, SIAM Rev. Chronicle 15 (1973) 423.

[51] S. Dyachenko, A. C. Newell, A. Pushkarev, V. E. Zakharov, Optical turbulence: weak turbulence, condensates and collapsing filaments in the nonlinear Schrödinger equation, Physica D: Nonlinear Phenomena 57 (1) (1992) 96–160.

[52] G. Strang, On the construction and comparison of difference schemes, SIAM Journal on Numerical Analysis 5 (3) (1968) 506–517.

[53] T. I. Lakoba, Instability analysis of the split-step Fourier method on the background of a soliton of the nonlinear Schrödinger equation, Numerical Methods for Partial Differential Equations 28 (2) (2012) 641–669.

[54] J.-B. Chen, M.-Z. Qin, Y.-F. Tang, Symplectic and multi-symplectic methods for the nonlinear Schrödinger equation, Computers & Mathematics with Applications 43 (8) (2002) 1095–1106.

[55] Y. Gong, Q. Wang, Y. Wang, J. Cai, A conservative Fourier pseudo-spectral method for the nonlinear Schrödinger equation, Journal of Computational Physics 328 (2017) 354–370.

[56] A. Semenova, S. A. Dyachenko, A. O. Korotkevich, P. M. Lushnikov, Comparison of Split-Step and Hamiltonian Integration Methods for Simulation of the Nonlinear Schrödinger Equation, arXiv preprint, arXiv:2008.03938 (2020).

[57] A. O. Korotkevich, A. I. Dyachenko, V. E. Zakharov, Numerical simulation of surface waves instability on a homogeneous grid, Physica D: Nonlinear Phenomena 321 (2016) 51–66.

[58] H. Yoshida, Construction of higher order symplectic integrators, Physics Letters A 150 (5) (1990) 262–268.

[59] A. J. Majda, D. W. McLaughlin, E. G. Tabak, A one-dimensional model for dispersive wave turbulence, Journal of Nonlinear Sciences 7 (1997) 1432–1467.

[60] A. I. Dyachenko, V. E. Zakharov, E. A. Kuznetsov, Nonlinear dynamics of the free surface of an ideal fluid, Plasma Physics Reports 22 (10) (1996) 829–840.

[61] V. E. Zakharov, E. A. Kuznetsov, A. I. Dyachenko, Dynamics of free surface of an ideal fluid without gravity and surface tension, Fizika Plasmy 22 (1996) 916–928.

[62] K. I. Babenko, Some remarks on the theory of surface waves of finite amplitude, in: Doklady Akademii Nauk, Vol. 294, Russian Academy of Sciences, 1987, pp. 1033–1037.

[63] J. Yang, Newton-conjugate-gradient methods for solitary wave computations, Journal of Computational Physics 228 (18) (2009) 7007–7024.

[64] J. Yang, Nonlinear waves in integrable and nonintegrable systems, SIAM, 2010.

[65] J. R. Shewchuk, et al., An introduction to the conjugate gradient method without the agonizing pain (1994).

[66] Y. Saad, Numerical methods for large eigenvalue problems, Manchester University Press, 1992.

[67] R. Lehoucq, K. Maschhoff, D. Sorensen, C. Yang, ARPACK software package, Rice University (1996).

[68] R. B. Lehoucq, D. C. Sorensen, C. Yang, ARPACK users' guide: solution of large-scale eigenvalue problems with implicitly restarted Arnoldi methods, SIAM, 1998.

[69] W. E. Arnoldi, The principle of minimized iterations in the solution of the matrix eigenvalue problem, Quarterly of applied mathematics 9 (1) (1951) 17–29.

[70] L. N. Trefethen, D. Bau III, Numerical linear algebra, Vol. 50, Siam, 1997.

[71] N. Hale, T. W. Tee, Conformal maps to multiply slit domains and applications, SIAM Journal on Scientific Computing 31 (4) (2009) 3195–3215.

[72] A. S. Dosaev, Y. I. Troitskaya, M. I. Shishina, Simulation of surface gravity waves in the Dyachenko variables on the free boundary of flow with constant vorticity, Fluid Dynamics 52 (1) (2017) 58–70.

[73] A. B. Shabat, V. E. Zakharov, Exact theory of two-dimensional self-focusing and one-dimensional self-modulation of waves in nonlinear media, Soviet Physics JETP 34 (1) (1972) 62.

[74] S. Novikov, S. V. Manakov, L. P. Pitaevskii, V. E. Zakharov, Theory of solitons: the inverse scattering method, Springer Science & Business Media, 1984.

[75] V. E. Zakharov, A. B. Shabat, A scheme for integrating the nonlinear equations of mathematical physics by the method of the inverse scattering problem. I, Functional analysis and its applications 8 (3) (1974) 226–235.

[76] M. Frigo, S. G. Johnson, The Design and Implementation of FFTW3, Proceedings of the IEEE 93 (2) (2005) 216–231, special issue on "Program Generation, Optimization, and Platform Adaptation".

[77] V. S. Varadarajan, Lie groups, Lie algebras and their representation, Prentice-Hall, Englewood Cliffs, 1974.

[78] J. A. C. Weideman, B. M. Herbst, Split-step methods for the solution of the nonlinear Schrödinger equation, SIAM Journal on Numerical Analysis 23 (3) (1986) 485–507.

[79] V. E. Zakharov, O. A. Vasilyev, A. I. Dyachenko, Kolmogorov spectra in one-dimensional weak turbulence, JETP Letters 73 (2) (2001) 1090–6487.

[80] W. Lee, G. Kovačič, D. Cai, Generation of dispersion in nondispersive nonlinear waves in thermal equilibrium, Proceedings of the National Academy of Sciences 110 (9) (2013) 3237–3241.

[81] B. Rumpf, A. C. Newell, Wave instability under short-wave amplitude modulations, Physics Letters A 377 (18) (2013) 1260 – 1263.

[82] V. E. Zakharov, V. S. Lvov, G. Falkovich, Kolmogorov Spectra of Turbulence I, Springer-Verlag, Berlin, 1992.

[83] J. Satsuma, N. Yajima, B. initial value problems of one-dimensional self-modulation of nonlinear waves in dispersive media, Progress of Theoretical Physics Supplement 55 (1974) 284–306.

[84] E. A. Kuznetsov, Solitons in a parametrically unstable plasma, DoSSR 236 (1977) 575–577.

[85] Y.-C. Ma, The perturbed plane-wave solutions of the cubic Schrödinger equation, Studies in Applied Mathematics 60 (1) (1979) 43–58.

[86] B. Kibler, J. Fatome, C. Finot, G. Millot, G. Genty, B. Wetzel, N. Akhmediev, F. Dias, J. M. Dudley, Observation of Kuznetsov-Ma soliton dynamics in optical fibre, Scientific reports 2 (2012) 463.

[87] T. I. Lakoba, Long-time simulations of nonlinear Schrödinger-type equations using step size exceeding threshold of numerical instability, J. Sci. Comput. 72 (2017) 14–48.

[88] V. E. Zakharov, Kinetic equation for solitons, Sov. Phys. JETP 33 (3) (1971) 538–541.

[89] D. S. Agafontsev, V. E. Zakharov, Intermittency in generalized NLS equation with focusing six–wave interactions, Physics Letters A 379 (40) (2015) 2586–2590.

[90] S. K. Turitsyn, J. D. Ania-Castañón, S. A. Babin, V. Karalekas, P. Harper, D. Churkin, S. I. Kablukov, A. E. El-Taher, E. V. Podivilov, V. K. Mezentsev, 270-km Ultralong Raman Fiber Laser, Phys. Rev. Lett. 103 (2009) 133901.

[91] S. K. Turitsyn, S. A. Babin, A. E. El-Taher, P. Harper, D. V. Churkin, S. I. Kablukov, J. D. Ania-Castañón, V. Karalekas, E. V. Podivilov, Random distributed feedback fibre laser, Nature Photonics 4 (4) (2010) 231–235.

[92] A. O. Korotkevich, P. M. Lushnikov, Proof-of-concept implementation of the massively parallel algorithm for simulation of dispersion-managed WDM optical fiber systems, Optics letters 36 (10) (2011) 1851–1853.

[93] G. Falkovich, N. Vladimirova, Cascades in nonlocal turbulence, Phys. Rev. E 91 (2015) 041201.

[94] Y. Chung, P. M. Lushnikov, Strong collapse turbulence in a quintic nonlinear Schrödinger equation, Phys. Rev. E 84 (2011) 036602.